MINIATURISED MAGNETIC BEAD ACTUATOR-BASED ATOMIC FORCE MICROSCOPE FOR SINGLE-MOLECULE MEASUREMENTS

ABSTRACT

Single molecular techniques have been providing researchers powerful tools to reveal the mechanisms of bioprocesses by investigating the behaviours and properties of individual molecules. It's also an essential way to study the functional differences and accesses the parameters of individual molecules.

Atomic force microscopy (AFM) is one of the most popular technologies to probe into individual molecules and has provided insights into structure, kinetics and dynamics of many molecules. However, the conventional AFM use cantilever-based sensors and piezo-based actuators which are relatively large in dimension and prone to drift and noise.

This thesis focuses on the development of a customised AFM for single molecule force spectroscopy experiments which is capable of both magnetic and piezo actuation. The magnetic actuation method unitises miniaturise magnetic beads as actuators reduces the actuator size significantly and performs experiment in non-contact way, thus reduces the impact of noise and drift. The resolution of the setup is verified experimentally and comparable to commercial AFM in single molecule force spectroscopy applications.

Single molecule force spectroscopy experiments using both varying loading rates and force clamp methods have been performed using biotin-streptavidin and heparin-FGF2 molecule pairs. The energy landscapes of their bonds have been studied.

LIST OF CONTENTS

ABSTRACT i
LIST OF FIGURES v
LIST OF TABLES ix
LIST OF ACRONYMS AND ABBREVIATIONS x
LIST OF PUBLICATIONS xi
ACKNOWLEDGEMENTS xii
DECLARATION xiii
1. INTRODUCTION 1
1.1 The Importance of Single Molecule Experiments 1
1.2 Commonly Used Tools for Single Molecule Observation 3
1.2.1 Micropipette 3
1.2.2 Single molecule fluorescence microscopy 4
1.3 Commonly Used Tools for Single Molecule Force Spectroscopy 7
1.3.1 The importance of force 7
1.3.2 Pulling vs. force clamp 10
1.3.3 Optical tweezer 12
1.3.4 Magnetic tweezer 15
1.3.5 Atomic force microscopy 16
1.4 Objectives 18
2. THE AFM SYSTEM 20
2.1 Principles of AFM 20
2.1.1 Conventional AFM systems 20
2.1.2 Optical readout principle 21
2.1.3 Force detection 24
2.1.4 Piezoelectric actuator 25
2.2 Design and Manufacturing of the AFM System 26

2.2.1 Design 26
2.2.2 Manufacturing 28
2.3 Characterisation of the AFM Head 30
2.3.1 Laser alignment 30
2.3.2 Deflection sensitivity calibration 33
2.3.3 Spring constant calibration 35
2.3.4 Noise analysis 37
3. MAGNETIC ACTUATOR 38
3.1 Magnetic Tweezer Actuators Options 38
3.1.1 Using permanent magnets 38
3.1.2 Using electromagnets 40
3.2 Force on the Beads in Magnetic Tweezer 43
3.2.1 Magnetic dipole model 43
3.2.2 Force estimation and calibration in magnetic tweezer systems 44
3.3 The Electromagnetic Actuator in This Work 46
3.3.1 The beads 46
3.3.2 The electromagnetic system 47
4. MODELLING OF THE AFM AND THE SOFTWARE CONTROLLER 53
4.1 Modeling 53
4.1.1 Force sensing system 53
4.1.2 The bead and the molecules 56
4.1.3 Electromagnetic actuator 58
4.1.4 The AFM system 63
4.2 Data Acquisition 67
4.3 The VI for Pulling Experiment 68
4.4 Force Clamp Experiments 69
4.4.1 Software structure 69
4.4.2 Force clamp pulling 70
5. BIOMOLECULAR EXPERIMENTS 73
5.1 Molecular Pulling Experiments Using Biotin-Streptavidin Pairs 73

5.1.1 Sample preparation 74
5.1.2 Results 75
5.2 Biotin-Streptavidin Force Clamp Experiment 79
5.2.1 Sample preparation 79
5.2.2 Results 80
5.2.3 Discussion 87
5.3 Heparin-FGF2 Pulling Experiments 88
5.3.1 Sample preparation 90
5.3.2 Results 90
5.4 Heparin-FGF2 Force Clamp Experiments 94
5.4.1 Sample preparation 94
5.4.2 Results 94
6. CONCLUSIONS 101
6.1 The Main Achievements in This Study 101
6.2 Main Features of the Developed System 104
6.3 Limitations and Possible Further Developments 105
REFERENCE 107

LIST OF FIGURES

Figure 1.1. Schematic of voltage patch clamp set up from Neher and Sackman [24] 4
Figure 1.2. Absorption and emission profile for Alexa Fluor 555 [30] 5
Figure 1.3. The schematic of molecule bond energy landscapes tilted by external force. (a) A single barrier, (b) two barriers while the inner one is dominant [45] 9
Figure 2.1. Schematics of conventional AFM system. (a) Cantilever actuated, (b) sample stage actuated. 20
Figure 2.2. Schematic of beam deflection method. 22
Figure 2.3 Block diagram of a quadratic photodetector [83] 23
Figure 2.4. Relationship between force on cantilever and photodetector readout. 24
Figure 2.5. CAD drawing for the AFM head case. 27
Figure 2.6. (a) The liquid cell adapter. (b) The commercial fluid cell [91] 28
Figure 2.7. The manufactured AFM head. 29
Figure 2.8. CAD top view of the AFM head, the kinematic rotation mount is shown in yellow [92] 30
Figure 2.9. Locations and interference patterns of the laser spot. Location of the laser spot (a) at the edge of the chip, (b) on the leg of the cantilever, (c) at the tip of the cantilever. The interference pattern when laser is (d) not on the cantilever, (e) on the leg of the triangular cantilever, (f) on the tip of the cantilever..... 32
Figure 2.10. T12XY/M translation stage [93] 33
Figure 2.11. Deflection signal and piezo input when the cantilever is in contact with a stiff surface. 34
Figure 2.12. PSD curve from a MESP cantilever, blue line is the measurement data, read line is the fitted curve. 36
Figure 2.13. Force noise density of the deflection signal acquired using a SNL-10 cantilever in air (black line) and in liquid (red line) [96] 37
Figure 3.1. Schematic of magnetic tweezer based on permanent magnets [97] 40
Figure 3.2. Schematic of magnetic tweezer implemented by electromagnet [98] 41

Figure 3.3. Schematic of Biot-Savart law. 42
Figure 3.4. Schematic of force estimation by inverted pendulum model in magnetic tweezer [103] 44
Figure 3.5. Characterisation of Dynabeads M-280 at room temperature in other literatures. (a) Hysteresis loops (magnetic field versus magnetisation) of M-280 [106] , (b) magnetisation curve (magnetic field versus magnetic moment) of M-280 Streptavidin [107] 47
Figure 3.6 Cross section of the magnetic actuator. 48
Figure 3.7. (a) Experimental set up to measure the magnetic field density at different distance from the tip. (2) Double exponential curve fittings for different current densities on the coil, dash point curves are the simulation results and solid curves are the fitted experimental results [96] 49
Figure 3.8. Force characterisation of the electromagnetic actuator. (a) Time response of force when the coil is actuated with 10 Hz (left) and 1 kHz (right) square wave current, (b) frequency response [96] 51
Figure 3.9. The thermal analysis of the electromagnetic actuator [96] 52
Figure 4.1. The schematic of the customised AFM [109] 53
Figure 4.2. Lumped-element model of the cantilever. 54
Figure 4.3. Lump-element model of a cantilever using Simulink. (a) Simulink model, (b) step response..... 55
Figure 4.4. Force on the biomolecule coated magnetic bead. 56
Figure 4.5. Simulink model of force on the magnetic bead. 58
Figure 4.6. Electrical characterisation of the electromagnetic actuator. (a) Impedance change corresponding to frequency and the fitted lumped-element model, (b) phase shift of the voltage across the coil..... 59
Figure 4.7. Simulink model of magnetic field gradient from electromagnetic actuator. 60
Figure 4.8. The magnetic field gradient generated by the electromagnetic actuator with respect of distance from the core tip. (a) Simulink simulation result and (b) calculation from experimental measurement with current density of 3 A/mm^2 and 4 A/mm^2 show in red and blue curves respectively, y-axis is the magnetic field

gradient (mT/μm). 61
Figure 4.9. Magnetic force applied on the bead. (a) Simulink model, (b) magnetic force. 63
Figure 4.10. Simulink model of the AFM system. 64
Figure 4.11. Time response of the AFM system. (a) Step input voltage to the coil drive amplifier, (b) corresponding force on the cantilever, (c) deflection of the cantilever. 65
Figure 4.12. Magnetic bead distance sweeps the full actuation range of the piezo actuator where the initial distance is 200 μm. (a) Distance from the initial, (b) force change on the bead according to distance, (c) deflection signal on the photodetector. 66
Figure 4.13. Block diagram of the AFM system. 67
Figure 4.14. User interface of pulling experiment VI. 68
Figure 4.15. Block diagram of the controller software [49] 70
Figure 4.16. Block diagram of the feedback controller and AFM system. 71
Figure 5.1. Schematics of experiments using biotin-streptavidin pairs. (a) Pulling experiment using piezo actuation, (b) pulling experiment using magnetic bead attached cantilever, (c) force clamp experiment using streptavidin functionalised magnetic beads. 73
Figure 5.2. Sample force curves using piezo pulling method. (a) A specific biotin-streptavidin event with about 200 pN unbinding force, (b) no rupture event. 76
Figure 5.3. Histogram of probability of unbinding force versus loading rates using biotin-streptavidin piezo pulling [96] 76
Figure 5.4. Force curves using magnetic bead attached cantilever and magnetic actuation (a) with specific unbinding force of 285 pN, (b) without event [96] 77
Figure 5.5. Loading rate versus most probable rupture force [96] 78
Figure 5.6. A sample force curve using feedback ON method. 80
Figure 5.7. A sample force curve showing multiple events using feedback ON method. 81
Figure 5.8. Histogram of lifetimes under clamping force from 45 pN to 60 pN using

feedback ON method [49] 82
Figure 5.9. The off-rate versus clamping force using controller ON method [49] 83
Figure 5.10. A sample force curve from experiments using feedback OFF method [49] 84
Figure 5.11. A sample force curve with two rupture events from experiments using feedback OFF method. 85
Figure 5.12. Histogram of lifetimes with clamping force from 40 pN to 55 pN using feedback OFF method [49] 85
Figure 5.13. The variation of off-rate as a function of clamping force when the feedback controller is turned off [49] 86
Figure 5.14. The comparison of off-rates using feedback ON and feedback OFF methods. (a) The statistical results and fittings, (b) the scatter plot [49] 88
Figure 5.15. Probability of ruptures in experiment group and control groups [152] 91
Figure 5.16. Sample force curve from heparin-FGF2 experiments using magnetic actuation [152] 92
Figure 5.17. Most probable rupture force as a function of loading rate [152] 93
Figure 5.18. A typical force curve from heparin-FGF2 force clamp experiment using feedback ON method..... 95
Figure 5.19. Histogram of lifetime with clamping force from 40 pN to 55 pN using feedback ON method from heparin-FGF2 force clamp experiment. 96
Figure 5.20. Sample force trace captured using feedback OFF method in heparin-FGF2 force clamp experiment. 97
Figure 5.21. Histogram of lifetimes under clamping force ranging from 55 pN to 65 pN using feedback OFF method in heparin-FGF2 force clamp experiment..... 98
Figure 5.22. Estimated off-rates as a function of clamping force from heparin-FGF2 experiments. 99
Figure 5.23. Nature logarithmic of off-rate versus clamping force from heparin-FGF2 experiments, data from feedback ON method is in red, from feedback OFF is in blue. 100

LIST OF TABLES

Table 3.1. Parameters using double exponential fitting. 50

Table 5.1 Bell's parameters of biotin-streptavidin interaction derived from experiments using customised AFM and commercial AFM 79

Table 5.2. Zero force off-rates K^0 and barrier widths x_β estimated from data using feedback ON method [49] 83

Table 5.3. Zero force off-rates K^0 and barrier widths x_β derived from feedback OFF method [49] 86

Table 5.4. Bell's parameters of heparin-FGF2 interaction at different loading rate regimes [152] 93

Table 5.5. Bell's parameters estimated from Heparin-FGF2 experiments using force clamp method. 99

Table 6.1 Specifications of the customised AFM 103

LIST OF ACRONYMS AND ABBREVIATIONS

AFM	Atomic Force Microscope
APD	Avalanche Photodiodes
BSA	Bovine Serum Albumin
CAD	Computer-Aided Design
CCD	Charge Coupled Device
CLK	Clock signal
DAQ	Data Acquisition
DI	Deionized
DS	Deflection Sensitivity
ESI	Electrospray Ionization
FGF	Fibroblast Growth Factor
FLIM	Fluorescence Lifetime Imaging
FRET	Fluorescence Resonance Energy
GAG	Glycosaminoglycan
GFP	Green Fluorescent Protein
HSPG	Heparan Sulfate Proteoglycans
MS	Mass Spectroscopy
NMR	Nuclear Magnetic Resonance
PBS	Phosphate Buffered Saline
PID	Proportional Integral and Deferential
PSD	Power Spectral Density
STM	Scanning Tunneling Microscope
TCE	Thermoelectric Cooler
TIRF	Total Internal Reflection Fluorescence
XRC	X-Ray Lithography

LIST OF PUBLICATIONS

Some of the results in this PhD thesis have been published in the following journals:

Sevim S, Ozer S, Feng L, et al. Dually actuated atomic force microscope with miniaturized magnetic bead-actuators for single-molecule force measurements[J]. Nanoscale Horizons, 2016, 1(6): 488-495.

Sevim S, Shamsudhin N, Ozer S, et al. An atomic force microscope with dual actuation capability for biomolecular experiments[J]. Scientific reports, 2016, 6: 27567.

Sevim S, Ozer S, Jones G, et al. Nanomechanics on FGF-2 and heparin reveal slip bond characteristics with pH dependency[J]. ACS Biomaterials Science & Engineering, 2017, 3(6): 1000-1007.

Feng L, Torun H. Miniaturized magnetic bead-actuators for force-clamp spectroscopy-based single-molecule measurements[J]. Ultramicroscopy, 2020, 209: 112888.

ACKNOWLEDGEMENTS

First of all, I would like to express my sincere gratitude to my supervisor Dr. Hamdi Torun. With his richness in knowledge, experience and dedication, he has guided me into the field of atomic force microscope and led me in the direction to complete this work; he is always prepared to help, listen to my questions and open to discussions.

I would like to thank MANAQA project (FP7-ICT-2011-C296679) for providing me the chance to be involved in this research. I would like to express my very great appreciation to our project partners from ETH-Zurich, University of Würzburg and Universitat Autònoma de Barcelona for their contribution and material supports.

I also feel lucky that I met so many friends here, especially my colleagues. They have helped me so much in both work and daily life and made me feel at home in a foreign country.

On a personal note, I cannot say enough to thank my parents for their unconditional support.

DECLARATION

I declare that the work contained in this thesis has not been submitted for any other award and that it is all my own work. I also confirm that this work fully acknowledges opinions, ideas and contributions from the work of others.

Any ethical clearance for the research presented in this thesis has been approved. Approval has been sought and granted by the Faculty Ethics Committee of Engineering and Environment on 28 February 2019.

Name: Luying Feng

Signature:

Date: 13.06.2020

1. INTRODUCTION

1.1 The Importance of Single Molecule Experiments

Researchers have for a long time been interested in understanding the fundamental mechanisms in bioprocesses and have been trying different ways to reveal their mechanisms. The traditional optical diffraction, biochemistry and biophysical methods are used to investigate the behaviour of ensembles of bio-molecules, the measured parameters are the average of the ensemble.

Utilising the laser scattering of the photon vibrations from wave number over $500 - 1800\ cm^{-1}$, Raman spectroscopy is used to measure the discrete vibrational energy, scattering probability and polarisation of ensemble species, the inter- and intra- molecular bond energy and structural information [1] . It has been used to characterise protein-DNA interaction recognitions [2] , to monitor protein bindings [3] , to reveal the conformation and kinetics of protein-peptide bonds [4] and to map the architecture of viruses [5] [6] successfully. High wave number $(2400 - 3800\ cm^{-1})$ Raman spectroscopy also has been used to investigate the internal changes of cells in vivo and vitro [7] .

The fundamental principle of X-ray crystallography (XRC) technique is to measure the periodic lattice distance by x-ray elastic scattering, it can reconstruct the 3D structure of the crystals by large numbers of diffraction patterns. And thanks to the invention of femtosecond X-ray laser which can provide high spatial resolution in low radiation does, small angle X-ray crystallography has been developed to study comparatively large proteins in hydrate stream [8] . It's also a powerful tool to investigate the internal structure and locate the binding sites and channels, etc. of proteins [9] [10] .

Mass spectroscopy (MS) can provide quantitative information on the mass-to-charge ratio of ions through a tube under vacuum. The measured sample requires special pre-treatment

such as enzyme digestion and mixing, then MS results are identified by database searching rapidly and inexpensively [11] . It has been widely used for protein sequencing [12] and virus identification [13] [14] . Electrospray ionization (ESI) mass spectroscopy is employed to monitor the charge state distribution of the intact and highly charged protein spray in vacuum [15] , offering a method to study protein conformational changes by analysing their weights change in different states [16] .

Isothermal titration calorimetry (ITC) provides a direct way to characterise thermodynamic properties of non-covalent interactions of two types of molecules in equilibrium. The measured thermodynamic parameters are reaction stoichiometry, association rate, free energy, enthalpy, entropy and heat capacity of binding [17] . It has been used to investigate the interactions of ion-protein [18] , protein-lipid [19] , ligand-receptor [20] , enzyme catalyst [21] and protein unfolding [22] , etc.

Although there are no chemical differences among the seemingly homogenous bio-molecular ensembles, the behaviour of individual molecules can't be distinguished. One should not ignore that molecules are intrinsically heterogeneous, the intermolecular variations do exist. Furthermore, it is also almost impossible to use the traditional bulk measurement methods to observe the behaviour of a certain molecule over a period of time as they require the synchronisation of the whole molecular population. Furthermore, bulk measurements are often affected by the presence of many different intermediates and of multiple species in a solution, so to distinguish the contribution of each species to the parameters is also challenging.

Alternatively, single-molecular methods focus on investigation of the behaviours and properties of individual molecule by allowing the study of their functional differences and providing the access to their parameters. Current single-molecule techniques are capable of microsecond temporal resolution, and therefore they can be used to assess the dynamics of the specific targets.

The methodologies of single-molecule approaches can be categorised into two general types: those that observe electrical or fluorescence signals of single molecules under thermodynamic equilibrium or nonequilibrium conditions and those that manipulate single molecules by applying force [23] .

.

1.2 Commonly Used Tools for Single Molecule Observation

1.2.1 Micropipette

The first single-molecule experiment was patch-clamp experiment performed by Neher and Sackman in 1976 during which single-channel currents from plasma membranes of frog skeleton muscle were recorded [24] , leading to the Nobel Prize in Physiology or Medicine in 1991 “for their discoveries concerning the function of single ion channels in cells” . Patch clamp techniques use a micropipette, which is usually a hollow glass pipette filled with electrolyte solution, to probe individual isolated living cell membranes. The enclosed or “patch” area only covers one or a few ion channel molecules. The voltage inside the pipette to the ground is kept constant during the experiment while the current through the pipette is measured as shown in the schematic of voltage clamp in Figure 1.1. Alternatively, the current is kept constant while the voltage across the membrane is measured. The techniques are especially useful to study excitable cells such as neurons [25] , cardiomyocytes [26] , stomach smooth muscle cells [27] and pancreas cells [28] . These techniques can also be applied to study bacteria [29] .

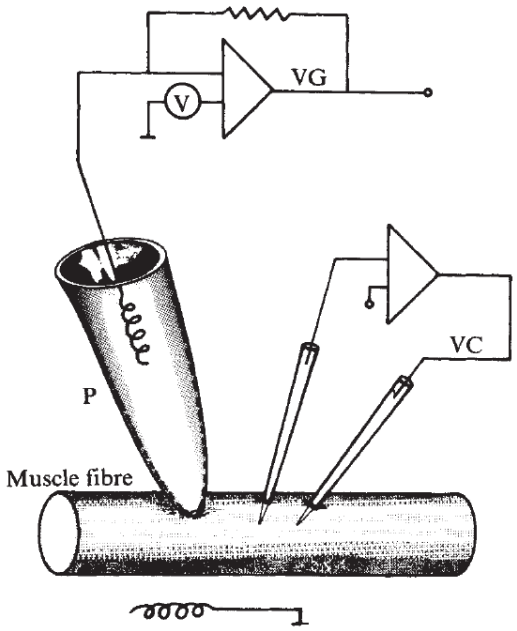

Figure 1.1. Schematic of voltage patch clamp set up from Neher and Sackman [24] .

1.2.2 Single molecule fluorescence microscopy

Fluorescence microscopy utilises fluorescence process that photon emission exhibits less than microsecond delay after the absorption of excitation light, the emission light intensity peak is usually lower in wavelength and intensity than the excitation light as shown in Figure 1.2, this process can be used to study organic and inorganic samples [30] . Thanks to the development of semiconductor technology that allows very small photon emission signal to be detected in very high time resolution and the development of fluorescence tags that can be conveniently integrated into the molecules, single molecule fluorescence microscopy techniques become a handy tool for single molecular studies.

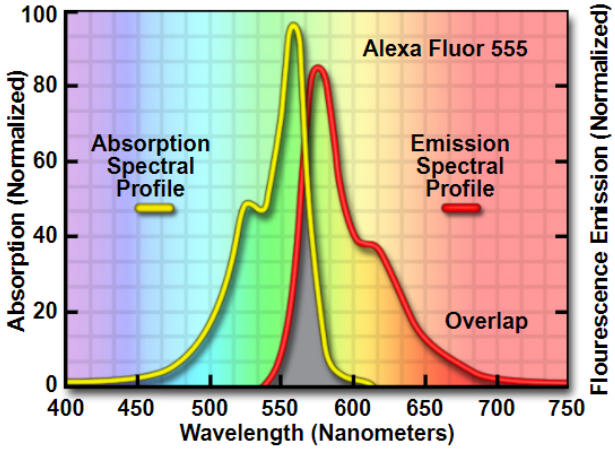

Figure 1.2. Absorption and emission profile for Alexa Fluor 555 [30] .

Detection technology

In far field region, the spatial resolution is limited by the optical diffraction. The Rayleigh criterion of the resolution limit is that two point-like objects observed through a circular aperture are separated by an angle larger than $\theta = 1.22\frac{\lambda}{D}$, where λ is the wavelength of the light, D is the diameter of the aperture.

Imaging in the near-field regime to avoid significant optical diffraction effect can push the resolution limit beyond the Rayleigh criterion and achieves super-resolution. Several super resolution techniques have been developed. The 2014 Nobel Prize in Chemistry was awarded to Eric Betzig, Stefan W. Hell and William E. Moerner "for the development of super-resolved fluorescence microscopy" [31] . Furthermore, mathematical fitting is also used to estimate fluorescence emission location to push beyond the optical limit further [32] .

Total internal reflection fluorescence (TIRF) microscopy has been applied on protein [33] and cells [34] for over a few decades. It's a technology that can be applied only to observe a thin region of specimen, using evanescent wave to selectively illuminate and excite fluorophores that are close to the coverslip. Thus, it's especially useful for investigation

of the labelled molecules. In 1995, single molecule experiment using this technique combining with microneedle and optical tweezer was already implemented to acquire in vitro experiment image of single fluorescent molecules and to monitor individual ATP turnovers by single myosin molecules, the experiment elucidates how myosin generates movement [35] . Nowadays, TIRF technique is often used in biophysicists and biochemists [36] .

Also, thanks to the development of electron multiplying charge coupled device (CCD) and avalanche photodiodes (APD) technology, single fluorescence microscopes with great sensitivity and time resolution are developed, recording single photon emission events which generate very weak signals and detecting single photons became possible [30] .

Fluorescence tag

The green fluorescent protein (GFP) was isolated from jellyfish Aequorea victoria in 1962 by Osamu Shimomura et al. [37] . Since 1988, Martin Chalfie et al. introduced the method to insert GFP into C.elegans and E.coli for colouring and tracking cells [38] . During 1990s, Roger Y. Tsien elucidated how GFP emitting its internal fluorescence light and succeeded in varying the colour of the light so that different proteins and multiple simultaneous biological processes could be tracked [39] . These three researchers were awarded the Nobel Prize in Chemistry in 2008 “for the discovery and development of the green fluorescent protein, GFP”.

Nowadays, numerous mutations of GFP aiming to improve its biophysical characteristics have been developed, different colour mutations have been added as well [40] . However, standard fluorescent proteins suffer from photobleaching problem after characteristic time and this irreversible phenomenon is due to the decomposition of the dye molecules [30] , therefore, long time scale experiment using this technique is challenging. Although some

new engineered fluorescent proteins have been developed to be more robust and tracking lifetimes are lengthened, the intrinsic photostability problem remains. A recent research also points out that the fluorescence labels can alter the natural interactions of protein and DNA which might cause the misestimation of the molecule interactions [41] .

1.3 Commonly Used Tools for Single Molecule Force Spectroscopy

1.3.1 The importance of force

Force plays an important role in kinetics and dynamics of molecules like other variables such as temperature and pressure. Many properties of the intermolecular and intramolecular reactions can be rationalized by the strength and direction of the force. In macroscopic manifestations, these phenomena can be shown as the change of elasticities and melting points of solids, the viscosities and the boiling points of liquids, and the compressibility of gases [42] .

Svante Arrhenius extended these ideas to microscopic manifestations and try to explain the kinetics and affinities between chemical species. His concept of activation energy argues that reactants must first acquire minimum kinetic energy E_a above the average energy of the whole ensemble to participate in reactions and transform into products. This concept is empirical, but explains the exponential nature of the relationship is present in all kinds of processes and reactions, exponential relationship can be used to model kinetics in these processes and reactions [43] .

The Arrhenius equation is:

$$k = Ae^{\frac{-E_a}{k_B T}} \tag{1.1}$$

where A is the temperature independent pre-exponential constant factor for the reaction,

E_a is the activation energy for the reaction in energy per molecule, k_B is the Boltzmann constant, T is the absolute temperature.

The transition state theory proposed in 1935 assumes a special equilibrium between reactants and activated transition state complexes. It illustrates qualitatively how chemical reactions occur. The activated complexes can be converted into products and the rate of this conversion can be calculated using kinetic theory. The rate constant k can be express as below:

$$k = \frac{k_B T}{h} e^{-\frac{\Delta G^{\ddagger}}{RT}} \tag{1.2}$$

where k_B is the Boltzmann constant, T is the absolute temperature, h is the Plank constant, $\Delta G^{\ddagger}$ is the standard Gibbs energy, R is the universal gas constant [44] .

Bell-Evan's theory explains that the dissociation time of molecule weak bond is dependent on applied force. Without force, molecule events happen due to thermal crossing of the potential energy barrier, sometimes it can take very long and make it very challenging to be measured. By applying force, the energy landscape can be tilted by force, the conceptual diagram is shown in Figure 1.3 [45] , for a sharp barrier, the change of shape and location of the transition state due to force can be ignored, by varying loading rates, applying dynamic force [46] or applying constant force over a long enough period of time [47] , the barrier is lowered, therefore, the energy landscapes of the bonds can be explored.

$$x_\beta = x_{ts} cos\theta \tag{1.3}$$

$$E_b(f) = E_b(0) - f x_\beta \tag{1.4}$$

$$k_{\rightarrow} = \frac{1}{t_D} \exp\left(\frac{-E_b(f)}{k_B T}\right) \quad (1.5)$$

Where x_{ts} is the location of transition state on x coordinate, E_b is the potential energy, f is the applied force, x_β is the energy barrier width along the direction of force, $k_{\rightarrow}$ is the escape rate, t_D is the relaxation time, k_B is the Boltzmann constant, T is the absolute temperature.

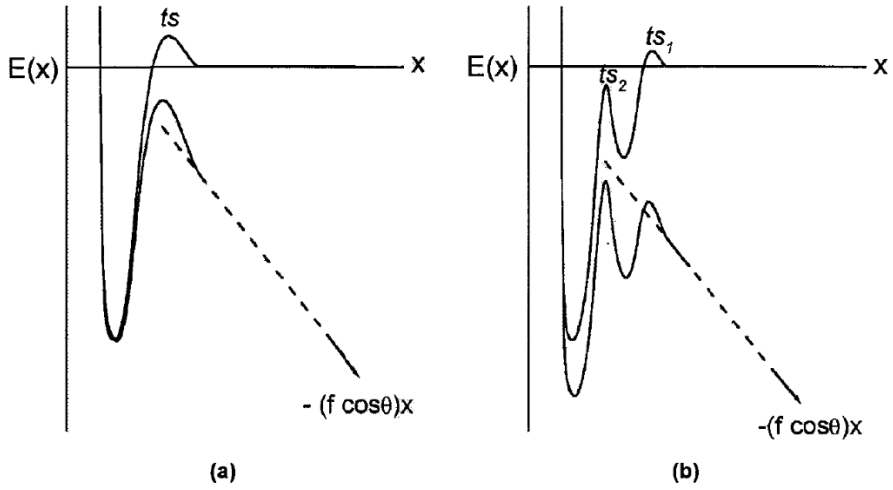

Figure 1.3. The schematic of molecule bond energy landscapes tilted by external force. (a) A single barrier, (b) two barriers while the inner one is dominant [45] .

The ergodic hypothesis in thermodynamics proposes that the process parameter of a single molecule averaged over time is equal to the average over the ensemble molecules at one time. Therefore, the measuring time on single molecule experiments must be long enough to cover its conformational space, and each experiment must be repeated enough times to obtain good statistics [48] .

These conceptual advances suggest that it is feasible to measure those force related parameters, but only until the development of single molecule manipulation techniques can the researchers gain powerful tools to access directly the force generated in chemical reactions, or even to apply external force to change the extent and rate of these reactions.

Similarly, mechanics and dynamics of inter- and intra-molecular interactions regulated by mechanical stimuli such as force also play a central role in biology. Spatial and temporal information on mechanical interaction force at single molecular level elucidates various biomolecular processes such as cell tethering, antigen binding to antibody, and protein folding/unfolding. In addition, mechanical measurements at single-molecular level on proteins and cells allow extraction of molecular kinetics and affinities, which are important for understanding the fundamental interaction between molecules, and in practical research, it's also important for drug developments [49] .

Besides, single molecule force spectroscopy also makes it possible to resolve the rare or transient phenomena that would otherwise be blurred by the averaging over large populations. For example, multi-states or multi-species distributions can be directly measured. Kinetic rates can also be directly measured by the time recording of single events or by statistically analysing the distribution of event times [23] .

Usually the kinetic and affinity parameters to estimate in single molecular experiments are off-rate k_{off}, the dissociation rate at zero force K^0, the width of energy barrier of the molecular bond x_β and $\Delta G^\ddagger$ the height of the energy barrier.

1.3.2 Pulling vs. force clamp

Conventional force spectroscopy using pulling, or force extension method is usually performed by fixing one end of the bonded molecular pair and pull the other in a constant speed, also called loading rate r_f. Driven far from the equilibrium, the association rate can be ignored, the relationship of likelihood of being in the bound state S_1 and loading rate r_f can be expressed as:

$$\frac{dS_1}{df} \approx -(\frac{t_{off}k_{\rightarrow}}{r_f})S_1 \quad (1.6)$$

where t_{off} is the forward passage time, f is the force between the bond, $k_{\rightarrow}$ is the escape rate.

The experiments are repeated multiple times under loading rate r_f, the statistics between probability of rupture $p(f)$ and force can be described by:

$$p(f) \approx \frac{k_{\rightarrow}(f)}{r_f(f)} S_1(f) \quad (1.7)$$

The maximum:

$$\frac{\partial p(f)}{\partial f} = 0 \quad (1.8)$$

The most probably rupture force f^* is statistically estimated under each loading rate r_f, and they follow the relationship [45] :

$$F \propto log\ (r_f) \quad (1.9)$$

With the most probable rupture force f^* under loading rate r_f, the kinetic parameters zero force off-rate K^0 and barrier width x_β can be measured with the equations below

$$k_{off}(f) = K^0 \exp\ (\frac{f}{k_B T / x_\beta}) \quad (1.10)$$

$$f^* = \frac{k_B T}{x_\beta} \ln\ (\frac{r_f x_\beta}{k_B T K^0}) \quad (1.11)$$

However, in this way the applying force is increasing over time, the calculated result

actually is a function of extension other than force, it represents a convolution of kinetics, force, length and time, which make it hard to resolve the force dependent parameters such as lifetime [47] . This method pulls the molecular bonds in a constant force until rupture events are observe, with the measured lifetime which is the reciprocal of off-rate k_{off} and the applied force f the energy landscape of the bond can be explored.

$$k_{off}(f) = K^0 \exp\left(\frac{f x_\beta}{K_b T}\right) \tag{1.12}$$

$$\ln\left(k_{off}\right) = \ln(K^0) + f \cdot \left(\frac{x_\beta}{K_b T}\right) \tag{1.13}$$

Force clamp method is a direct way to measure the force dependent parameters. Besides, force between biomolecules or within biomolecules are usually not changed drastically, using force clamp method can mimic the actual physiological conditions.

1.3.3 Optical tweezer

Optical tweezer was Introduced by Arthur Ashkin, Steven Chu and their co-workers at AT&T Bell Laboratories in 1986, it's a single beam optical trap that is capable of trapping dielectric particles with the size range from 10 μm down to ~25 nm [50] . The principles of the optical tweezer are very straightforward. For an object that is much smaller than the wavelength of the light, an electric dipole moment regarding to the light's electric field is drawn up intensity gradients toward the focus. For an object that is much larger than the wavelength of the light, it acts as a refractive lens and redirecting the momentum of the photons of the light rays, resulting in the force from the photons draws the object toward the focus where there are higher flux of photons [51] .

In the Rayleigh regime where the particle is much smaller than the wavelength, the particle can be viewed as an induced electric dipole moment in an electromagnetic field. For a spherical particle with radius r and refractive index n_b in a Gaussian beam, the scattering force F_{scat} due to the radiation pressure of the incident light is

$$F_{scat} = \frac{P_{scat}}{c} n_b = \frac{I_0}{c} \frac{128\pi^5 r^6}{3\lambda^4} \left(\frac{m^2-1}{m^2+2}\right) n_b \tag{1.14}$$

where P_{scat} is the power scattered, c is the speed of light, I_0 is the intensity of the light, λ is the wavelength of the light, m is the relative refractive index between the particle and the medium.

The gradient force F_{grad} acting on the particle is due to the electromagnetic field induced Lorenz force

$$F_{grad} = -\frac{n_b}{2} \alpha \nabla E^2 = -\frac{n_b^3 r^3}{2} \left(\frac{m^2-1}{m^2+2}\right) \nabla E^2 \tag{1.15}$$

where α is the polarizability of the particle, E is the electric field of the light.

Stable trapping can be achieved when the R parameter, which is the ratio of backward gradient force to forward-scattering force, is large enough. This requires the beam diverges from the focal point rapidly enough such that the axial gradient force dominates [50] . For a Gaussian beam with spot size ω_0 and wavelength λ, the maximum intensity in z axial occurs at

$$z = \pi\omega_0^2/\sqrt{3}\lambda \tag{1.16}$$

$$R = \frac{F_{grad}}{F_{scat}} = \frac{\sqrt[3]{3}}{64\pi^5} \frac{n_b^2}{\left(\frac{m^2-1}{m^2+2}\right)} \frac{\lambda^5}{r^5 \omega_0^2} \geq 1 \tag{1.17}$$

For small displacements which is usually smaller than about 150 nm from the equilibrium

position of the trapped object, the optical trap can be well approximated as a linear spring that obeys Hook's law where the force is linearly proportional to the displacement. The spring constant, or stiffness, is depending on the properties of the optical trap and the trapped object, for example, the steepness of the optical gradient which is depending on the power and focusing of the laser, and the polarizability, size and shape of the trapped object [52] .

The conventional gradient force optical tweezers can't trap too small particles, because the polarizability α of the particle scales as the third power of the particle size from Rayleigh scattering [50] . To overcome this problem, nanoaperture optical tweezer is developed. In this technique, the particle itself plays an important role in trapping by modifying the transmission through the aperture, as a result the range of optical tweezer to dielectric particles extends below 50 nm in size in "dirty" solution, trapping proteins becomes possible [53] .

Since optical tweezer is a non-invasive, label-free, tether-free approach to manipulate objects in liquid, it is very suitable for single bio-molecule experiments. The biological particles that are probed using this technique include proteins, DNA, viruses, antibody and small molecules. As its name indicates, it also can be a handy tool to assemble, reconfigure and dismantle cell-sized vesicles networks [54] , to manipulate single human virus and study of viral-cell interactions [55] . It provides a non-contact way to select and translocate single cells [56] . It has also been used to study the unzipping of individual DNA-hairpin pairs and quantify the delay of the unzipping cause by tumour suppressor p53 protein [57] . It is also a tool to characterise the mechanical property of molecules, for example, determining the elastic modulus of white blood cells [58] .

The development of dynamic holographic optical tweezers realised by spatial light modulator can sculpt the wave fronts of each trap individually and move them in three dimensions [59] , and thus 3D displacement and real time measurement of the trapped particles become possible, which means parallel experiments become possible and the

throughput of optical tweezers is enhanced.

Since laser is the direct manipulation tool of optical tweezer, some problems have to be considered. The laser beam may interact with photosensitive biological samples, it may also cause damage to the samples due to heating. Furthermore, high performance lasers are very expensive.

1.3.4 Magnetic tweezer

Using magnetic particles as manipulators has a long history. In 1949, Francis Crick and Arthur Hughes from Cambridge University already used external magnetic field to move the tiny magnetic beads engulfed by the plasma membrane of the cells grown in culture medium through the cells and observed the cells with high power microscopy, the physical properties of the cells were measured [60] . But the magnetic tweezer appeared relatively late in 1990s.

The implementation of magnetic tweezer is relatively simpler than optical tweezer, that is to apply pulling or torsional force to manipulate magnetic particles by changing the magnetic field on them, generally speaking the magnetic field does not affect the samples. Magnetic tweezer can implement almost infinite bandwidth and large displacements force, which means it can perform force clamp experiments passively [61] . The innovation of chemically linking an individual molecule between a magnetic bead and a glass slide also expands the application scenarios of magnetic tweezer. These properties together make magnetic tweezer especially popular for DNA studies. For example, it have been used by researchers to probe into the structural and mechanical properties [62] [63] and quantitatively study the dynamics of DNA [64] . It is also commonly used to study molecular interactions, such as bond lifetime-force behaviours [65] .

However, magnetic tweezer generally has comparatively low trap stiffness, therefore the force range that can be applied is also comparatively low, normally it's in the piconewton level. The spatial and temporal resolution are also limited by the video-camera based data acquisition method, although the performance can be improved to reach Angstrom level by using high speed camera and super-luminescent diode [66] .

1.3.5 Atomic force microscopy

Atomic force microscopy (AFM) is a type of scanning probe microscopy (SPM) with Angstrom vertical resolution and nanometre lateral resolution. The AFM was invented by IBM scientists Gerd Binning and Heinrich Rohrer in 1982, the first experimental implementation was made in 1986. It was developed based on the principles of the scanning tunnelling microscope (STM) and the stylus profilometer [67] . The AFM was first commercialized in 1989, and thanks to the development of MEMS technology, various choices of cantilevers with different probe shapes and stiffness values specialised for different functions such as high speed, ultra-high resolution, conductive and magnetic measurements are also commercially available now.

The AFM's precursor STM helped its inventors to win the Nobel Prize in Physics in 1986. It is based on the concept of quantum tunnelling. During STM measurement, a conducting tip is brought very close to the sample surface, then a biased voltage is applied between the tip and sample allowing electrons tunnel through them. The tunnelling current is a function of tip position, applied voltage and local density of states of the sample, thus information of the sample can be acquired by investigating the tunnelling current [68] . The lateral resolution of this technique can reach $0.1\ nm$ and depth resolution can reach $0.01\ nm$. However, because it usually requires extremely clean and stable surface, very sharp tips, good environment vibration control and sophisticated electronics, the application scenarios are limited.

AFM is also a scanning technique, but AFM measures the force applied on the samples rather than measures the tunnelling current. During AFM measurement, a sharp cantilever tip is brought into contact with the sample surface, the force between the tip and the surface results in bending of the cantilever which obeys Hooke's law. This bending is amplified and measured using the laser deflected from the back side of the cantilever. The force that can be measured using AFM includes both strong (ionic and covalent) and weak interaction forces (Van der Waals force, capillary force, electrostatic force, etc.). Additional information can be simultaneously measured by using special cantilever tips. The working environment of AFM is relatively relaxed as it does not require vacuum environment. The measurement can be performed in liquid environment easily, relatively dirty, sticky and rough samples can also be probed.

The lateral resolution of AFM is limited by the tip end radius size, for example, the commonly used pyramid shape tip radius is 15-40 nm, providing a resolution of about 30 nm due to the convolution of tip and surface profiles, but with ultra-sharp probe, the resolution can be down to 2 nm. But it has vertical displacement resolution down to Angstrom level and the force resolution down to piconewton level [69] .

Due to the wide range of choices of commercially available tips that are suitable for various environments, decent lateral resolution and very high vertical resolution, AFM has become a versatile tool and has been applied to a wide range of nature science study at the nanoscale including molecular engineering, characterisation of polymers, liquid, cells and molecules, inter- and intra-molecular analysis.

AFM has been widely used to image stiff [70] and soft [71] sample surface topographies. Because it can be applied in liquid environment, it's also used to image bio-samples in vivo [72] . High speed AFM can even be used to produce videos of samples in vitro and first visualised the myosin V molecules walking along actin tracks in 2010 at the frame rate of $146.7\ ms$ [73] . AFM is even getting faster and can reach 30-60 frames per second

[74] .

Besides for surface topography study, AFM is also a powerful tool to characterise samples, for example, measuring sample viscosity [76] , elastic property [75] [77] and adhesion [78] [79] . More importantly, due to its high force sensitivity, it's also commonly used to study particle-cell interactions [80] , molecular bonds [81] , force induced domain ruptures happen between different protein sequences and tertiary structures in polyproteins [82] , etc..

AFM has its own limitations as well. The measurement is based on cantilever deflection technique, which is sensitive to environment noise, therefore, noise isolation chamber and careful designed active feedback controller for noise cancelation is critical for AFM experiments. The AFM cantilever undergoes Brownian motion due to thermal noise which is inversely proportional to spring constant of the cantilever, as shown in equation (2.12), the root mean square amplitude of the Brownian motion of a commercially available AFM cantilever typically ranges from 0.01 nm to 1 nm in room temperature, therefore, it's difficult to apply very small force precisely to the sample with a cantilever, especially for force clamp experiments.

1.4 Objectives

The aim of this study is to develop a new AFM system with micro/nano-level actuators for improved single-molecular measurements. The specific objectives to meet the aim are as follows:

1. Design and implementation of a setup combining the fundamentals of AFM and magnetic tweezer utilising the advantages of high vertical resolution and

straightforward detection of AFM cantilever deflection technique together with the non-contact and low stiffness actuation of magnetic tweezers;

2. Realising a new system capable of both conventional pulling experiments and both active and passive force-clamp experiments;
3. Verifying the new system and investigating single-molecular interactions between biotin and streptavidin
4. Investigating single-molecular interactions between heparin and Fibroblast Growth Factors 2 (FGF-2) and revealing the bond property using the new system.

Our AFM was designed focusing on increasing hardware and software modularity for biomolecular applications. The modular design consists of the AFM head with piezo actuation, the sample stage with electromagnetic actuation and the software controller. The design was realised using 3D printing techniques and a software-based controller. Each of these parts will be explained in detail in the coming chapters.

2. THE AFM SYSTEM

This chapter first introduces the basic working principles of AFM systems, then describes the design and characterisation of the AFM system developed in this research.

2.1 Principles of AFM

2.1.1 Conventional AFM systems

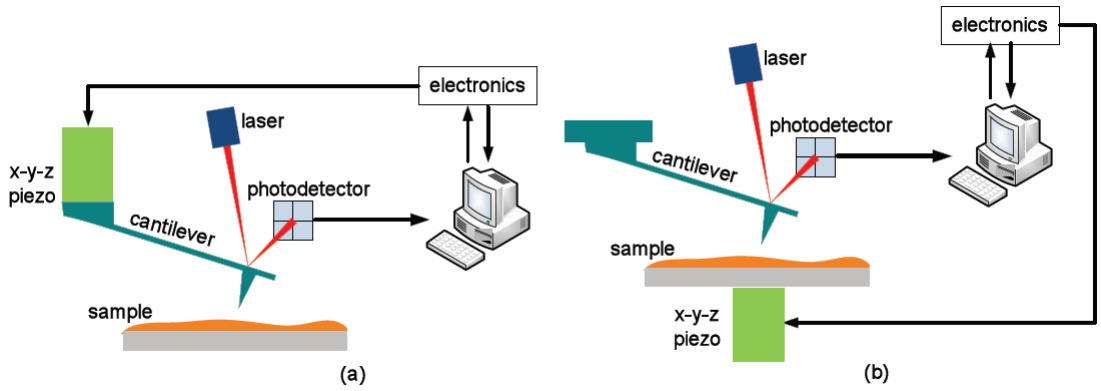

Figure 2.1. Schematics of conventional AFM system. (a) Cantilever actuated, (b) sample stage actuated.

The conventional AFM systems can be classified into two types: the cantilever actuated configuration, as shown in Figure 2.1 (a), and the sample stage actuated configuration, as shown in Figure 2.1 (b). The main principles are very similar, in both cases, a spring-like cantilever is anchored at a certain angle with the surface. A focused laser is shone on the back side of the highly reflective cantilever tip then is deflected back to a photodetector. The deflected laser signal which indicates the movement of the cantilever is captured by the photodetector and converted to electric signals. The signals are sent to the controller which generates actuation signals to the piezo actuator accordingly to adjust the position of the cantilever. In a cantilever actuated system, the cantilever is actively actuated all the

time even if there's no interaction between the cantilever and sample surface. The readout optics has to be adaptive to the cantilever fluctuations, therefore, the system is relatively more complicated than the stage actuated system. However, the cantilever actuated configuration allows the entire active detection system fits into the top hemisphere and left the stage passive, it can reserve the bottom hemisphere for additional functionalities and further customisations.

2.1.2 Optical readout principle

Optical beam deflection method sometimes also called "optical lever" method, is used in most of the commercial AFM due to the simplicity of experimental set up, a schematic is shown in Figure 2.2. Assume that the laser is perfect, then scattering is ignored, the laser beam follows the geometrical optics. When the cantilever with length d moves by a small displacement, the change on the cantilever tip is Δd, the angular change of the cantilever is θ . When θ is small, $tan\theta \approx \theta$. The total length of the optical path is L, the displacement change of the laser spot on the photodetector is ΔL, then the relationships can be approximated as follow:

$$\theta = \frac{\Delta d}{d} \tag{2.1}$$

$$\theta = \frac{\Delta L}{L} \tag{2.2}$$

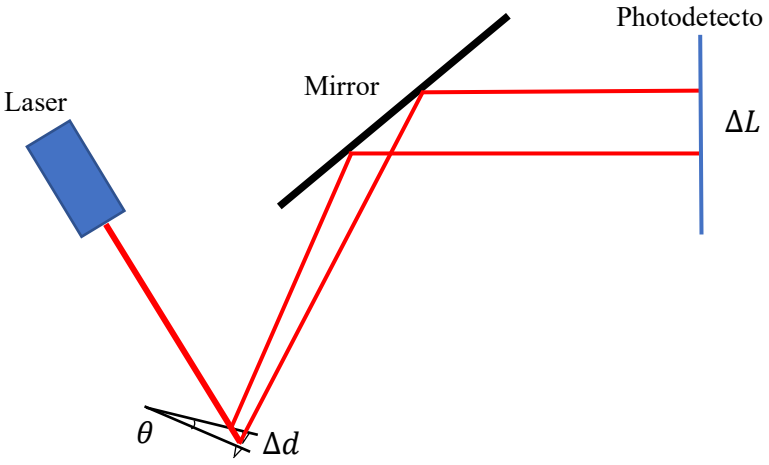

Figure 2.2. Schematic of beam deflection method.

The displacement change of the cantilever is magnified by the optical path and measured as deflected spot location change on the photodetector. The photodetector produces differential top-bottom and left-right signals and a sum signals that are related to the laser spot location and intensity. Thus, the displacement of the cantilever is measured.

$$V_{t-b} = [(I_3 + I_4) - (I_1 + I_2)] \times A \tag{2.3}$$

$$V_{l-r} = [(I_2 + I_3) - (I_1 + I_4)] \times A \tag{2.4}$$

$$V_{sum} = (I_1 + I_2 + I_3 + I_4) \times A \tag{2.5}$$

A block diagram of a quadratic photodetector is shown in Figure 2.3. As shown in the figure, the currents I_1, I_2, I_3 and I_4 are caused by the laser excitation of electrons in the corresponding photodiodes, these currents are proportional to the laser intensity before saturation. Then the current signals are amplified by a constant transimpedance gain A, in this example it is in the order of 10^4. The top-bottom signal V_{t-b} and left-right signal V_{l-r} are proportional to the location related to the centre of the quadratic photodetector due to the resistive elements in the photodiodes, the sum signal V_{sum} is

related to laser power, these voltage signals are calculated by a sum and difference amplifier following equation (2.3) to (2.5).

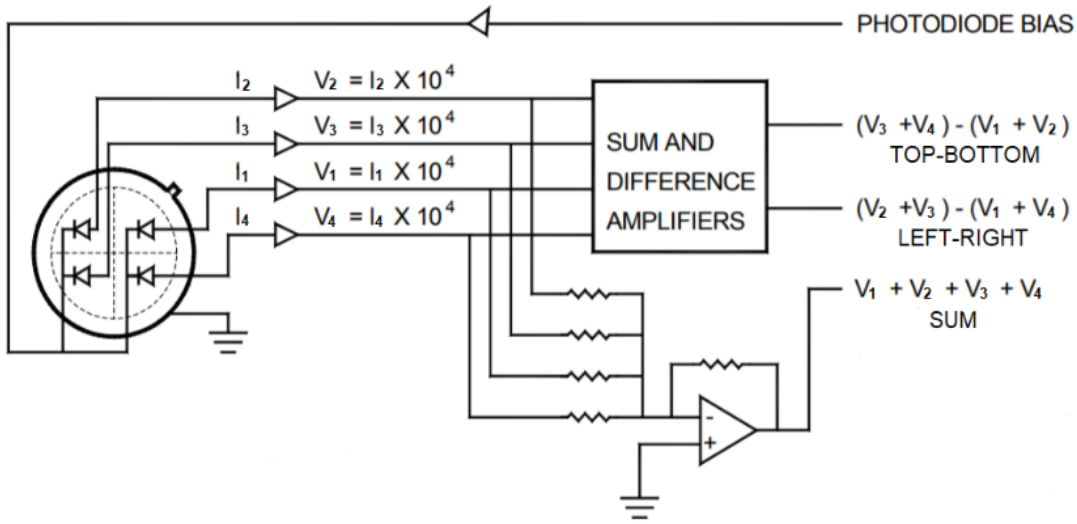

Figure 2.3 Block diagram of a quadratic photodetector [83] .

However, in reality it doesn't mean that a longer optical path always enhances the measurement. As the optical path gets longer, the laser spot deflected on the photodetector also becomes more diverging due to optical diffraction, some amount of optical power is moved to the nearby ones and measurement precision is reduced. Likewise, if the laser source is too far away from the cantilever, the laser spot at the cantilever can be larger than the cantilever width, some part of it will fall off the cantilever and can't be reflected to the photodetector, introducing power loss. Some advanced techniques have been developed by other researchers to overcome these problems [84] .

Therefore, when using relatively simple beam-deflection method, the optical path should be carefully designed to achieve high sensitivity.

2.1.3 Force detection

The deflection sensitivity DS can be defined as relative displacement of the cantilever divided by the relative photodetector signal from the same linear region. When the cantilever is pressed on a hard surface by distance Δd and the corresponding relative photodetector readout is ΔV, then:

$$DS = \frac{\Delta d}{\Delta V} \tag{2.6}$$

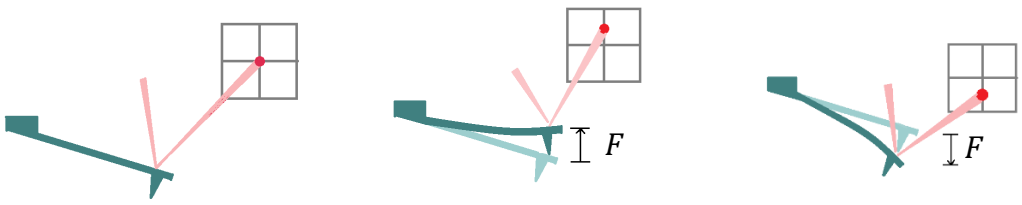

(a) **(b)** **(c)**

Figure 2.4. Relationship between force on cantilever and photodetector readout.

Calculation of the force applied on the cantilever is very straightforward. Figure 2.4 shows the schematic of the relationship between the force and the laser spot location on the photodetector. The cantilever experiences force F in vertical direction obeys Hook's law within its linear deflection range:

$$F = k \cdot \Delta d \tag{2.7}$$

where k is the spring constant of the cantilever which can be obtained from the

manufacturers and can be calibrated.

Pressing force will result in the cantilever bending upwards while the dragging force will result in the cantilever bending downwards as shown in the schematics. When the deflection sensitivity DS is measured, the force can be readily calculated from the relative photodetector readout ΔV:

$$F = k \cdot DS \cdot \Delta V \tag{2.8}$$

However, it's necessary to calibrate the spring constant and deflection sensitivity of the cantilever to obtain more accurate measurements. The popular spring constant calibration methods include thermal tune or thermal noise method [85] [86] and reference cantilever method [87] . The thermal tune calibration method is integrated in most of the commercial AFM software.

2.1.4 Piezoelectric actuator

Most of the scanners in AFM systems utilise piezoelectric effect for actuation. The "piezoelectric effect" and "inverse piezoelectric effect" was discovered by Jacques and Pierre Curie in 1880 [88] . The piezoelectric effect describes the induced electric charge due to mechanical stress, converts mechanical energy into electrical energy. Vice versa, the inverse piezoelectric effect explains the induced mechanical strain when electrical voltage is applied, converts electrical energy into mechanical energy. Nowadays, piezoelectric and inverse piezoelectric effects have been used in many scientific instruments and everyday products such as lighters, loudspeakers and signal transducers.

The relationships between the electrical and elastic properties for small electrical and mechanical signals can be described by linearised relations:

$$S = s^E T + dE \tag{2.9}$$

$$D = dT + \varepsilon^T E \tag{2.10}$$

Where S is the mechanical strain tensor, s^E is the elasticity coefficient matrix under constant electric field, E is the electric field, d is the piezoelectric material coefficient matrix, D is the Electric flux density, T is the mechanical stress tensor, ε^T is the permittivity under constant stress [89] .

Although the above simplified relations can't describe the non-linear behaviours such as creeps and hysteresis of piezo actuators [90] , it's adequate for most of the applications.

2.2 Design and Manufacturing of the AFM System

2.2.1 Design

The AFM system was designed based on a cantilever-actuated setup, the top hemisphere, which is also called as AFM head in this thesis, is reserved for piezoelectric actuator and optical readout. The bottom hemisphere is reserved for electromagnetic actuation and all the other subsystems. Two main functional parts of the AFM head were designed separately: the AFM head case and the liquid cell adapter.

A CAD drawing of the AFM head case designed with SolidWorks (Dassault Systemes S.A.) is shown in Figure 2.5. The compact design houses a laser source, a cylindrical

piezo actuator and related mechanical components fits in a space of $66.6 \times 117 \times 40\ mm$.

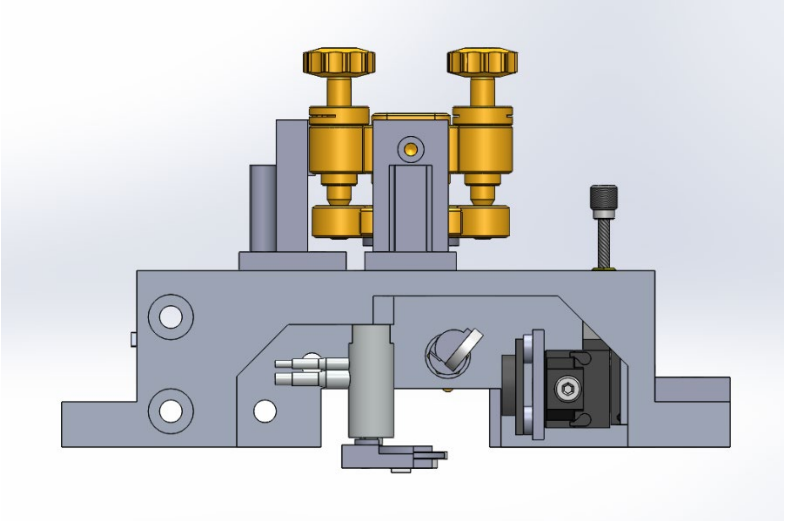

Figure 2.5. CAD drawing for the AFM head case.

The laser source is mounted on top of the head with a metal kinematic rotation mount which is fixed to the head case by custom designed posts via M3 screws. Since the aim in this work is to measure molecular bonds along a single axis, a piezo actuator with a single translational axis for vertical motion was employed. The piezo actuator (P-840.1, Physik Instrumente, Karlsruhe, Germany) is mounted to the head case via a M5 screw. The free end of the piezo actuator holds a commercial fluid cell (Bruker Probes, CA, USA) via a customised designed adapter. A quadratic photodetector (QP50-6-18u-SD2, Pacific Sensor, CA, USA) with $250\ k\mathrm{Hz}$ cut off frequency is mounted on the right inner wall of the case and the position of it can be adjusted by a two-dimensional translation stage with $12.7\ mm$ travel distance in each axis (T12XY miniature, Thorlabs, NJ, USA) for laser alignment. The incoming laser is deflected off the cantilever then steered to the photodetector by a $12 \times 12\ mm$ mirror which is attached to the inner back wall of the case by an adjustment rotational knob. The distance from the laser source to the cantilever is $60\ mm$, from the cantilever and to the mirror is $45\ mm$.

A CAD drawing of the fluid cell adapter and the commercial cantilever holder for fluid experiments are shown in Figure 2.6 (a). A narrow slide on that adapter that just fits the fluid cell in is designed so that no screws are needed to mount the liquid cell. The adapter dimension is $22.95 \times 25.75 \times 6\ mm$.

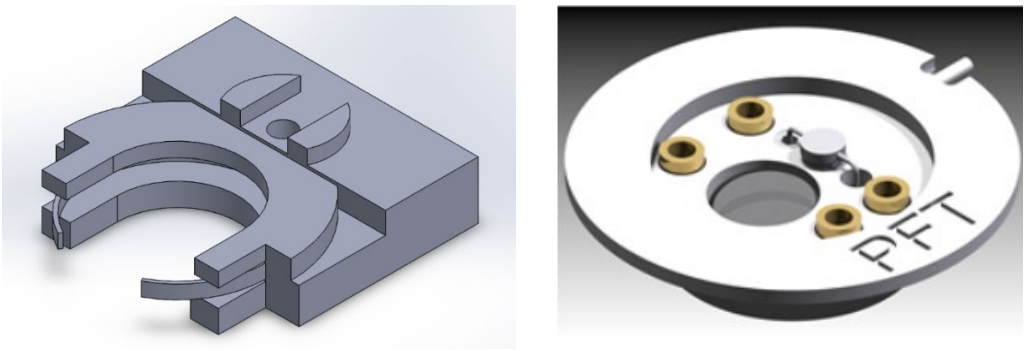

(a) (b)

Figure 2.6. (a) The liquid cell adapter. (b) The commercial fluid cell [91] .

2.2.2 Manufacturing

The AFM head case was fabricated with general-purpose rigid resin (Objet VeroWhitePlus, RGD835) using stereolithography 3D printing (Stratasys Objet Eden260V, MN, USA). The components of the head were assembled as shown in Figure 2.7. It's low cost, portable, light weight and easy to fabricate and assemble while still rigid enough for precise measurements.

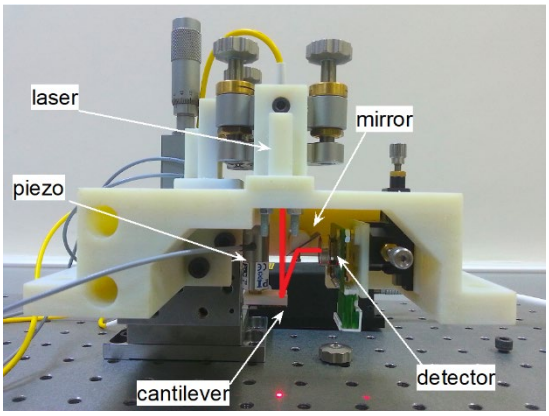

Figure 2.7. The manufactured AFM head.

The cylindrical piezo used to actuate the cantilever is relatively short ($32\ mm$ in length, $12\ mm$ in diameter) but covers $15\ \mu m$ travel distance which is adequate for biomolecular force spectroscopy experiments. The piezo actuator is also used for the fine positioning of the cantilever. An adapter, as shown in Figure 2.6 (a) connects the commercially available fluid cantilever holder, as shown in Figure 2.6 (b), to the free end of the actuator.

In actual experiments, a sample stage integrated with electromagnetic actuator is placed below the cantilever which is fixed on the fluid cell at an angle of 12° by a special designed spring. The working distance when using electromagnetic actuation, which is defined as the distance between cantilever tip and the magnetic core tip under the sample stage surface, is $500\ \mu m$. The distance between the cantilever tip and sample stage surface is controlled precisely by a manual Vernier micrometre (SM25, Newport, CA, USA).

A red laser source (LPF-03, OzOptics, Ontario, Canada) with $633\ nm$ wavelength is used to realise the optical lever method mentioned earlier. The laser is fibre-coupled to an aspheric focusing lens with a focal length of $13.9\ mm$. The diameter of the laser spot at a distance of $60\ mm$ is approximately $20\ \mu m$, which is smaller than the widths of most

of the commercially available cantilevers. The distance between the laser source and the cantilever together with the laser spot location on the cantilever can be adjusted with the kinematic rotation mount (SN100-F3K, Newport, CA, USA). The angular range of the rotation mount is $\pm 7°$. The focused laser spot shines on the cantilever and the reflected light is steered to the quadrant photodetector by the mirror placed at an angle of $33°$, the optical path is shown as the read lines in Figure 2.7.

2.3 Characterisation of the AFM Head

2.3.1 Laser alignment

Laser alignment on the cantilever is achieved by adjusting the three knobs of the kinematic rotation mount, Figure 2.8 shows the top view of the AFM head where the kinematic rotation mount is shown clearly (yellow colour). Figure 2.9 illustrates the procedure in further details. Laser spot can be aligned on the tip of a triangle shape cantilever following the experiential steps described below.

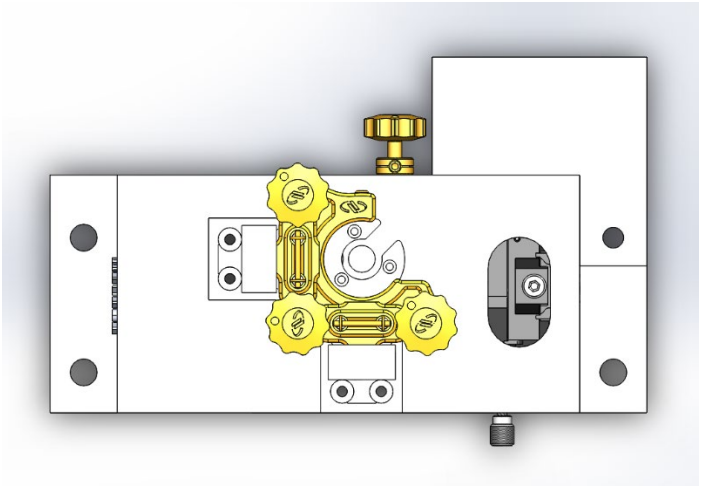

Figure 2.8. CAD top view of the AFM head, the kinematic rotation mount is shown in yellow [92] .

First, the laser spot location is adjusted to the edge of the cantilever chip by adjusting the bottom right knot, thus moving the laser spot parallel to the cantilever direction. The location can be verified visually from the laser pattern on the sample stage surface. If the laser is not on the cantilever, the pattern will be similar to Figure 2.9 (d), if the laser is at the edge of the chip, as the schematic in Figure 2.9 (a), a portion of that pattern will be cropped, if the laser is completely on the chip of the cantilever, no laser spot will appear on the sample stage surface.

Then the laser spot is adjusted to the desired cantilever by adjusting the top knot, thus moving the laser spot along the edge of the cantilever chip, while counting the number of cantilever legs. Diffraction pattern which is perpendicular to the cantilever can be observed on the sample stage surface, if the laser spot is on a cantilever, the pattern is similar to Figure 2.9 (e).

Afterwards, the laser spot can be adjusted to the tip of the desired cantilever readily, as shown in Figure 2.9 (c), by fine tuning the top and bottom right knots, thus moves the laser along the cantilever leg in a zig-zag way, as shown in Figure 2.9 (b), until the spot reach the tip. If the spot is at the tip, a concentric ring diffraction pattern which looks like Figure 2.9 (f) can be observed on the sample stage surface. The final step is to maximize the sum signal by very small adjustments around the tip region.

The laser alignment for a rectangular shape cantilever can also follow the above method except that the concentric ring diffraction pattern cannot be observed when the spot is at the tip, therefore, to locate the laser spot on the tip, the laser spot can be moved long the cantilever until out of it then moved backward slightly.

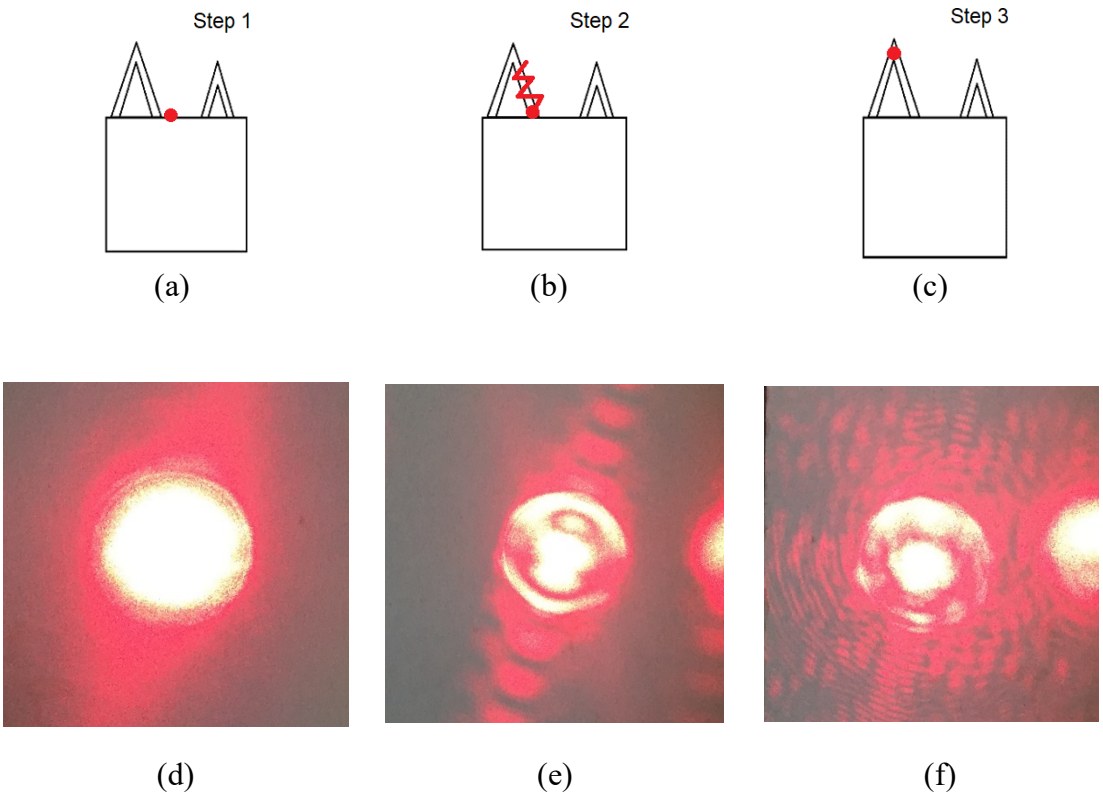

Figure 2.9. Locations and interference patterns of the laser spot. Location of the laser spot (a) at the edge of the chip, (b) on the leg of the cantilever, (c) at the tip of the cantilever. The interference pattern when laser is (d) not on the cantilever, (e) on the leg of the triangular cantilever, (f) on the tip of the cantilever.

Laser spot size on the cantilever can also be adjusted by turning the three knobs with the same amount of angle when the laser is aligned on the tip of a triangular shape cantilever to achieve larger sum signal. Generally speaking, the laser spot should be smaller than the cantilever width, further adjustment can be achieved by observing the diffraction pattern as shown in Figure 2.9 (f). A rule of thumb is that the 0^{th}-order pattern in the concentric ring diffraction pattern centre should be as bright as possible so that most of the laser can be deflected by the cantilever.

To align laser spot at the centre of the quadratic photodetector, one method is to adjust the location of the photodetector by the top-bottom and left-right knots of the translation

stage which is shown in Figure 2.10, the other is to fine adjust the optical path by adjusting the angle of the mirror around the $33°$ designed angle.

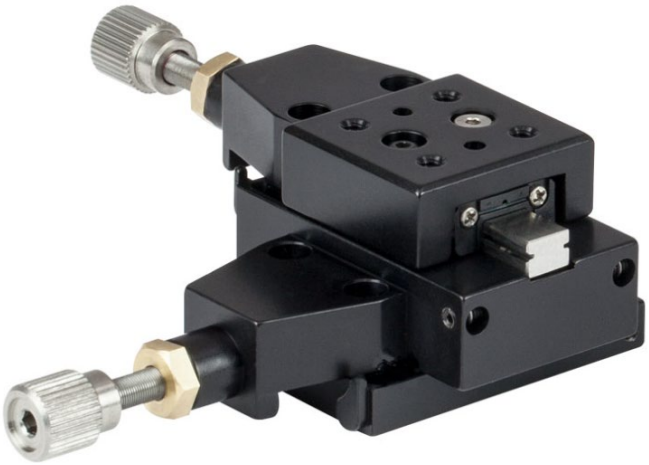

Figure 2.10. T12XY/M translation stage [93] .

2.3.2 Deflection sensitivity calibration

The cantilever can be brought in contact with the sample surface by adjusting the Vernier micrometre on the AFM head and the height of the sample stage manually or by adjusting the DC voltage on the piezo actuator. A triangle wave voltage signal is applied to the piezo actuator which extends by a transduction ratio of $k_{piezo} = 1.5\,\mu m/V$ whereas the deflection signal from the photodetector which indicates the vertical position of the cantilever can be observed. If the cantilever is in contact with a stiff surface, deflection signal similar to Figure 2.11 can be observed. The deflection signal in Figure 2.11 is a typical deflection sensitivity calibration curve obtained in liquid environment, the triangle portion of the deflection signal indicates that the cantilever is in contact with the surface, the step shape signal is due to the hydrodynamic drag force when the cantilever changes direction suddenly, the relatively flat portion means the cantilever is moving in the liquid

in one direction with constant speed.

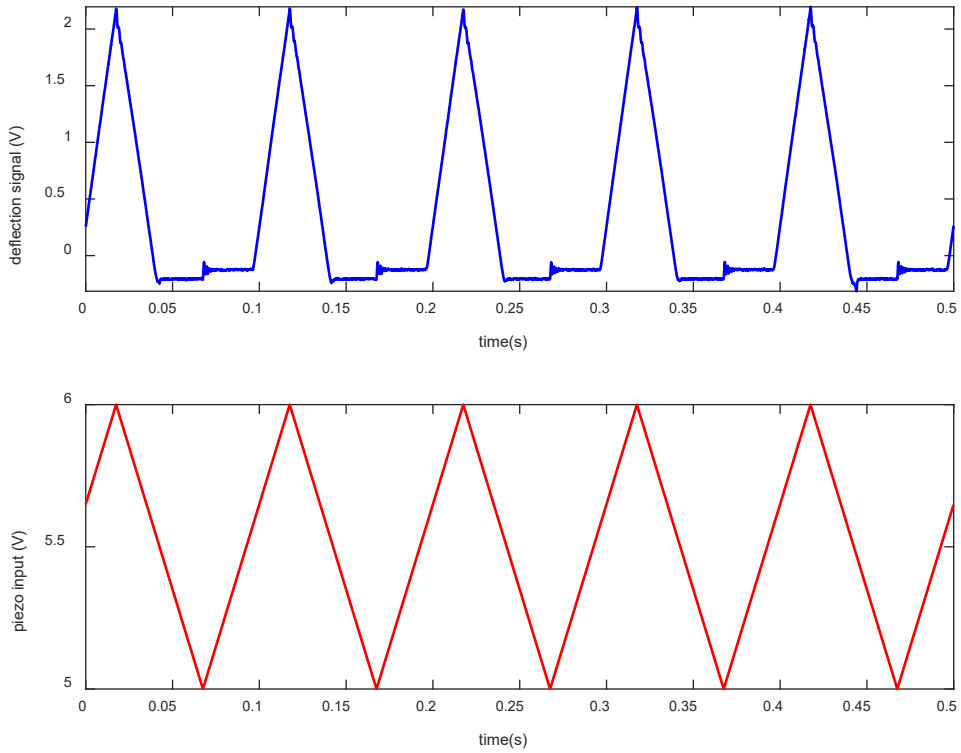

Figure 2.11. Deflection signal and piezo input when the cantilever is in contact with a stiff surface.

The deflection signal corresponds to increasing piezo input is called approach curve and that to decreasing piezo input is called retract curve. Deflection sensitivity can be calculated using the linear part of the approach curve with equation (2.6), knowing that the piezo actuator extension is proportional to the piezo input, the coefficient is $k_{piezo} = 1.5\ \mu m/V$ in our system,

$$DS = \frac{\Delta d}{\Delta V} = \frac{2Afk_{piezo}\Delta t}{\Delta V} \tag{2.11}$$

where A and f are the amplitude and frequency of the voltage applied to the piezo

actuator respectively, ΔV is the relative deflection signal during Δt. The deflection sensitivity in Figure 2.11 is calculated to be $0.28\ \mu m/V$.

2.3.3 Spring constant calibration

The spring constant of the cantilever can be calibrated with thermal tune method. This method is based on the equipartition theorem and makes quantitative prediction of kinetic and potential energy of the cantilever as a single spring based on its Brownian motion. The equation below tells that the average kinetic energy of the vertical axis motion is equal to the thermal energy of that degree of freedom.

$$\langle \frac{1}{2} k z^2 \rangle = \frac{1}{2} k_B T \tag{2.12}$$

where k is the spring constant of the cantilever, z is the cantilever motion in vertical direction, k_B is the Boltzmann constant and T is the absolute temperature.

The fastest and simplest method is to directly measure the mean square displacement $\langle z^2 \rangle$, however, due to the external noise the spring constant is usually underestimated [94] .

Another commonly used method is the thermal tune method which is based on the power spectral density (PSD) measurement of the cantilever. According to Lorenz PSD model [95] :

$$p(f) = L(f) = \frac{a_0}{(f-a_1)^2+a_2} + a_3 \tag{2.13}$$

where $p(f)$ is the fitting of PSD, f is the frequency, a_3 is the background white noise,

a_1 is the resonance frequency.

Q factor of the cantilever:

$$Q = a_1/(2\sqrt{a_2}) \tag{2.14}$$

Spring constant:

$$k = (k_B T)/(\frac{\pi a_0}{\sqrt{a_2}}) \tag{2.15}$$

Figure 2.12 is a PSD curve recorded from a MESP cantilever (Bruker), the nominal length is $225\ \mu m\ (200 - 250\ \mu m)$, width is $28\ \mu m\ (23 - 33\ \mu m)$, thickness is $2.75\ \mu m$, spring constant is $2.8\ N/m\ (1 - 5\ N/m)$, resonance frequency is $75\ k\text{Hz}\ (60 - 100\ k\text{Hz})$. The calculated Q factor is 108 and spring constant is $1.2\ N/m$ using Lorenz PSD model.

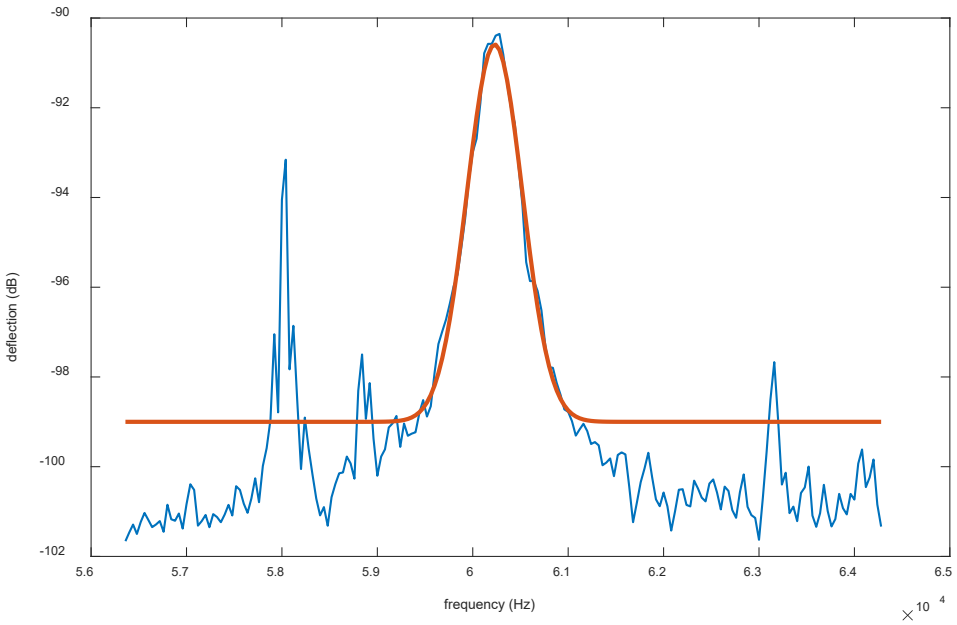

Figure 2.12. PSD curve from a MESP cantilever, blue line is the measurement data, read line is the fitted curve.

2.3.4 Noise analysis

Noise analysis of the AFM was performed using a commonly used SNL10-D cantilever (Bruker). The nominal length of the cantilever is $205\ \mu m$ $(200-210\ \mu m)$, width is $25\ \mu m$ $(20-30\ \mu m)$, thickness is $0.6\ \mu m$, resonance frequency is $18\ k\text{Hz}$ $(12-24\ k\text{Hz})$, nominal spring constant is $0.06\ N/m$ $(0.03-0.12\ N/m)$. Figure 2.13 is the force noise spectrum of the vertical deflection signal obtained until 100 kHz. The sensitivity and spring constant were calibrated before the measurement. The original measured result was in voltage, then is converted into force here. The resonance peak in air is about $18\ kHz$ as expected, it broadened and shifted to about $4\ kHz$ in DI water due to damping effect. However, our interest is only focus on frequency below $1\ kHz$ in bio-experiments, the bandwidth here is adequate. When only consider the actuation bandwidth below $1\ kHz$, the integrated noise is $1.82\ pN$ in air and $2.98\ pN$ in liquid, which can also be considered as force resolution of the system [96] .

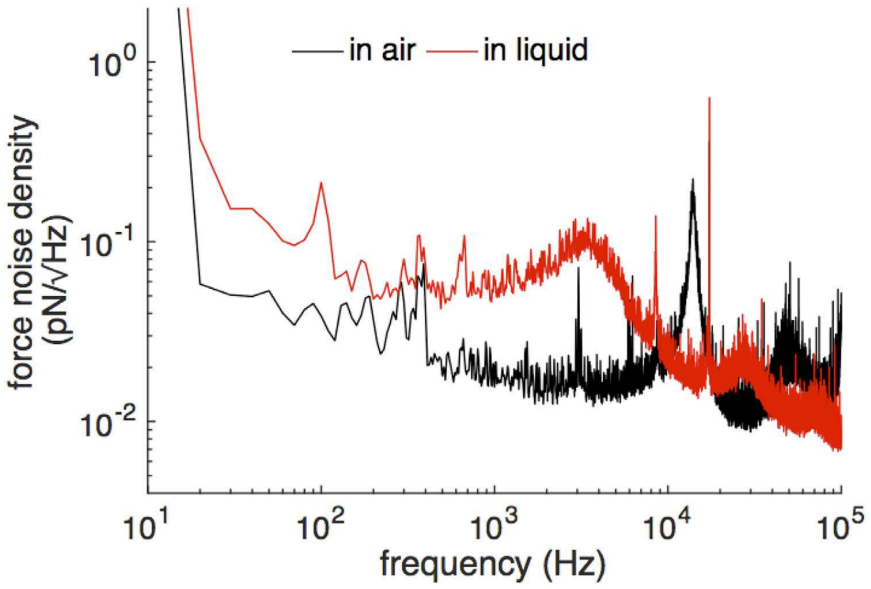

Figure 2.13. Force noise density of the deflection signal acquired using a SNL-10 cantilever in air (black line) and in liquid (red line) [96] .

3. MAGNETIC ACTUATOR

This chapter focuses on the design and characterisation of the magnetic actuator integrated with the AFM head within the customised setup. Firstly, the basic principles and applications of magnetic tweezers are described. Then, the magnetic actuator developed in this study based on the concepts of magnetic tweezers is described.

3.1 Magnetic Tweezer Actuators Options

3.1.1 Using permanent magnets

In a permanent magnet there's always a pair of opposite poles, north pole and south pole. Even if the magnet is cut into very tiny pieces the pair of poles still exist due to the fact that the domains in the magnet are lined up in the same direction. Magnetic monopole is a hypothetical concept that has not been observed. Inside of a magnet, according to Poisson's model, a magnetic field H, measured in A/m, is produced by magnetic poles, and magnetisation vector M is due to small pairs of north and south magnetic poles and defined as the magnetic dipole moment per unit volume of that region. Outside of the magnet, the magnetic flux density B, measured in tesla (T), is proportional to H field. In Maxwell's equation the relationship between B-field and H-field is:

$$B = \mu_0(M + H) \tag{3.1}$$

where μ_0 is the vacuum permeability, $\mu_0 = 4\pi \times 10^{-7} H/m$.

The permanent magnets actuated magnetic tweezer can be simplified as a pair of magnets

with north pole of one magnet facing the south pole of another is placed on top of the sample fluid cell sample stage that is located on top of an inverted microscope. The magnets are usually made of rare-earth materials, neodymium iron boron ($Nd_2Fe_{14}B$) magnets are among the strongest permanent magnets commonly available. To reduce the stray field effect caused by the H field generated by the magnetisation in a magnet, usually an iron ring is placed around the magnets and provides a return path for the magnetic flux. The actuator can be integrated with an inverted microscope in one setup as demonstrated where a collimated light through the gap of the magnets illuminates the sample [97] .

The experiment is prepared by attaching one end of the molecule to the sample surface and another end to a magnetic bead. Pulling force along a single threshold axis can be achieved without local minimum by moving the pair of magnets along the vertical axis; rotational force can be achieved by attaching the pair of magnets to a rotary motor and rotate them. A schematic of magnetic tweezer based on permanent magnets is shown in Figure 3.1.

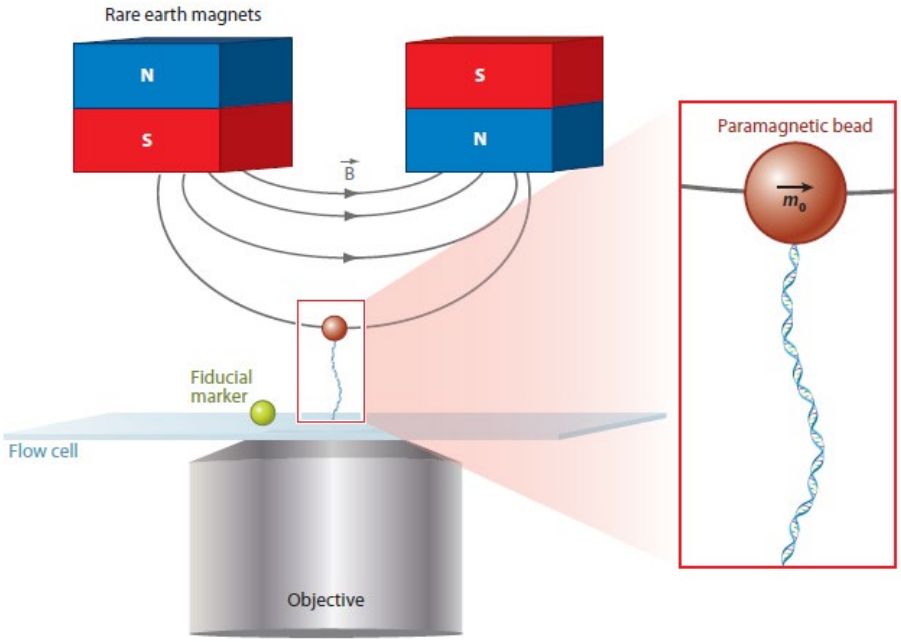

Figure 3.1. Schematic of magnetic tweezer based on permanent magnets [97] .

3.1.2 Using electromagnets

Magnetic actuators can also be implemented by electromagnets which consists of several sets of pointed tip magnetic cores made of soft magnets winding with current conducting coils. A schematic is shown in Figure 3.2.

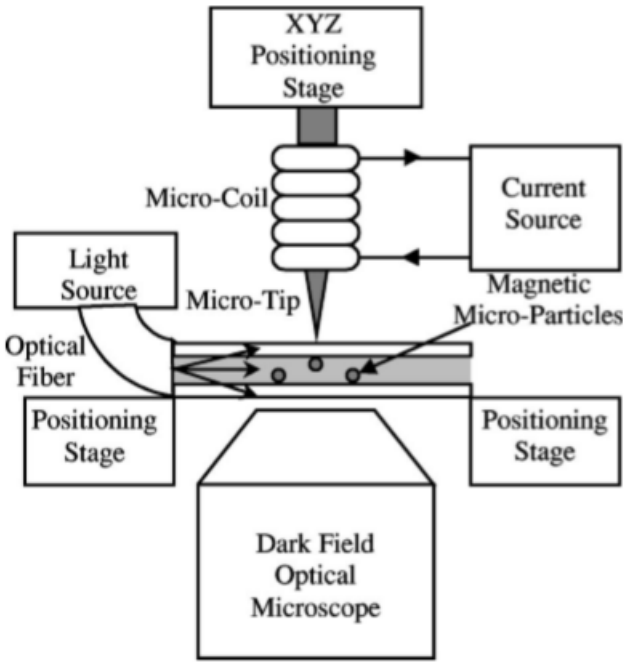

Figure 3.2. Schematic of magnetic tweezer implemented by electromagnet [98] .

According to Biot-Savart law, in 3D space, the magnetic field at any point P generated by a constant current I in a wire can be described by:

$$B = \frac{\mu_0}{4\pi}\int_{wire}\frac{Idl\times\hat{r}}{|r|^2} \tag{3.2}$$

Where μ_0 is the vacuum permeability, dl is a vector segment along the wire, r is the distance from dl to P, $\hat{r}$ is a unit vector of r. A schematic of it is shown in Figure 3.3.

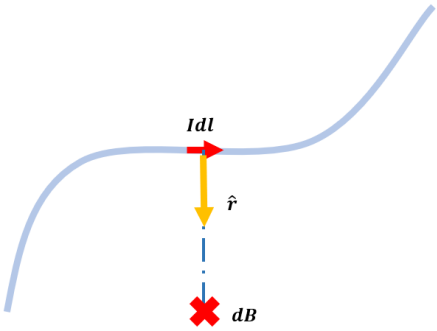

Figure 3.3. Schematic of Biot-Savart law.

The domains in the core are in random directions without current, the magnetic field from these domains cancel out each other, therefore the core almost doesn't show any magnetic field. When the current is on, the domains are aligned in the same direction as the magnetic field generates from the winding, those fields add to the wire's field and create a large magnetic field. The number of domains lining up increases with current along the coil until all the domains line up and reach saturation. The calculation of the electromagnetic field is usually done by finite element simulation due to the complexity [99] .

Some of the advantages of using electromagnet as actuator are the capability of swiftly changing the magnetic field strength and direction, thus the actuation force, by changing the amplitude and phase of the current in the winding coils rather than moving the magnets with motors, which allow easier control over the force. However, hysteresis, which is dependent on the core material in the magnetic field, as a function of current is also introduced. However, the actuation force usually is lower than using permanent magnets in similar configuration. Moreover, the current in the coil also generates heat, a cooling system may be needed [100] .

3.2 Force on the Beads in Magnetic Tweezer

3.2.1 Magnetic dipole model

The magnetic beads are magnetised in the magnetic field, the induced magnetic dipole moment of the magnetic bead m in a weak external magnetic field before saturation can be estimated as:

$$m = \frac{V_b \chi}{\mu_0} B \tag{3.3}$$

Where V_b is the volume and χ is the magnetic susceptibility [101] .

The force of the magnetic dipole described by classical electric current loop model is given by [102] :

$$F = \nabla(m \cdot B) \tag{3.4}$$

Therefore, in a week magnetic field, the magnetic force on the magnetic bead can be estimated as:

$$F = \frac{V_b \chi}{\mu_0} \nabla |B|^2 \tag{3.5}$$

In a strong magnetic field where the magnetic moment is saturated, the magnetic force can be estimated as:

$$F = \nabla(m_{sat} B) \tag{3.6}$$

where m_{sat} is the magnetic moment in saturation.

The magnetisation value may differ from device to device due to manufacturing, the calculation and measurement of B field in the exact position is also very challenging, the estimation of the force in this work therefore is using experimental approach.

3.2.2 Force estimation and calibration in magnetic tweezer systems

The force estimation in most of the magnetic tweezers relies on camera-based position tracking method. The molecule tethered magnetic bead can be described by an inverted pendulum model as shown schematically in Figure 3.4, where the molecule experiences force F, the magnetic bead fluctuates around its mean position due to Brownian motion. The fluctuation of the magnetic bead position $\langle \delta x^2 \rangle$ can be linked to force by:

$$\langle \delta x^2 \rangle = \frac{k_B T L_{ext}}{F} \tag{3.7}$$

where k_B is the Boltzmann constant, T is the thermodynamic temperature, L_{ext} is the extension of the tether at force F. The force is inverse proportional to the variance of the bead position [103] .

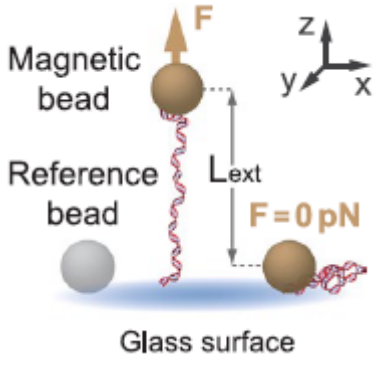

Figure 3.4. Schematic of force estimation by inverted pendulum model in magnetic tweezer [103] .

A camera is used to capture the images of the bead, the measured position x_m at time t over the integration time W is estimated as:

$$x_m(t) = \frac{1}{W}\int_{t-W}^{t} x(t')dt' \tag{3.8}$$

The variance of the true trajectory of the particle obeys the equipartition theorem:

$$Var\langle x\rangle \equiv \langle x^2\rangle - \langle x\rangle^2 = \frac{k_b T}{k} \tag{3.9}$$

where k is the trap stiffness of the potential trap.

However, due to the finite camera shutter time, the variance of measured position x_m is smaller or equal to the variance of the true position x:

$$Var\langle x_m\rangle \leq Var\langle x\rangle \tag{3.10}$$

The reduced variance of measured position causes overestimation of the force, thus, calibration of the force is essential before biological experiments when using magnetic tweezers [104] .

An alternative way to calibrate the magnetic tweezers is by using the viscous drag in a known liquid. According to Stokes' law, the frictional force for the spherical particle in the liquid can be described by:

$$F_{drag} = 6\pi\eta R_b v \tag{3.11}$$

where v is the velocity, η is the medium viscosity, R_b is the particle radius.
The stiffness of the trap can be calibrated in Fourier space as:

$$k = \frac{k_B T}{\int_0^\infty df |x(f)|^2} \tag{3.12}$$

where $|x(f)|^2$ is the power spectrum of the particle fluctuation in x direction [105] .

3.3 The Electromagnetic Actuator in This Work

3.3.1 The beads

Commercial superparamagnetic Dynabeads M-280 Streptavidin from TermoFisher were used in this study. They are uniform beads with a diameter of $2.8\,\mu m$ with streptavidin monolayer covalently bonded to the surface. The magnetic characterisation of the beads has been done by other researchers, as shown in Figure 3.5.

The magnetisation M in high field where the magnetic moment is saturated can be expressed as:

$$M = M_0\left(1 - \frac{k_B T}{M_S \langle V \rangle B}\right) \tag{3.13}$$

$$m = MV \tag{3.14}$$

where M_0 is the saturation magnetisation, M_s is the intrinsic spontaneous magnetisation and $\langle V \rangle$ is the mean volume of the particles, m is the magnetic moment. $M_0 = 10.8\,Am^2/kg$ and $M_s = 336\,kA/m$ for Dynabeads M-280 were measured in literature [106] .

The measurement in another literature also indicates that Dynabeads M-280 streptavidin are easily to be magnetised to magnetic moment large enough for saturation [107] .

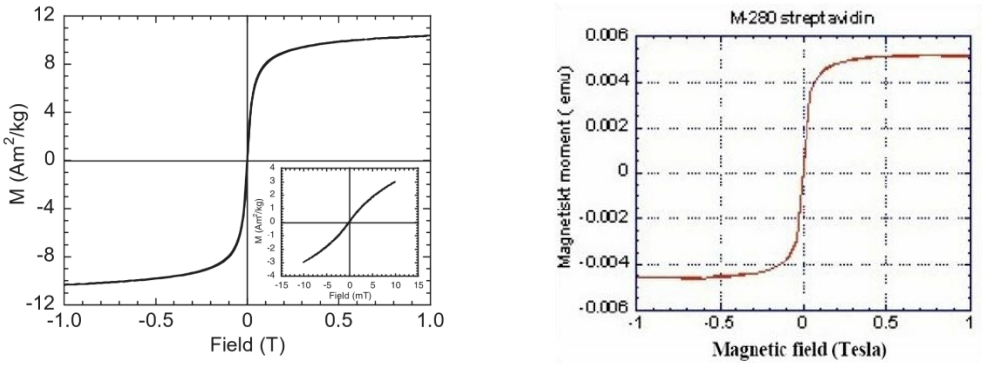

(a) (b)

Figure 3.5. Characterisation of Dynabeads M-280 at room temperature in other literatures. (a) Hysteresis loops (magnetic field versus magnetisation) of M-280 [106] , (b) magnetisation curve (magnetic field versus magnetic moment) of M-280 Streptavidin [107] .

3.3.2 The electromagnetic system

The electromagnetic actuator consists of a cylindrical cobalt-iron core and copper coil. The magnetic field distribution depends highly on the material and geometry of the core. Within practical design constrain, tip length does not affect the field distribution drastically [108] , based on empirical results, $4.0\ mm$ was selected in this work. Tip end radius alters the field drastically in vicinity of the tip end. The sharper the tip the grater the magnetic gradience can be achieved. However, due to the consideration of repeated machining with tight geometry tolerance constrain, $0.5\ mm$ was chosen. The final design of the core is $3\ mm$ in radius and $30\ mm$ in length. A cross section of the magnetic tweezer is shown in Figure 3.6.

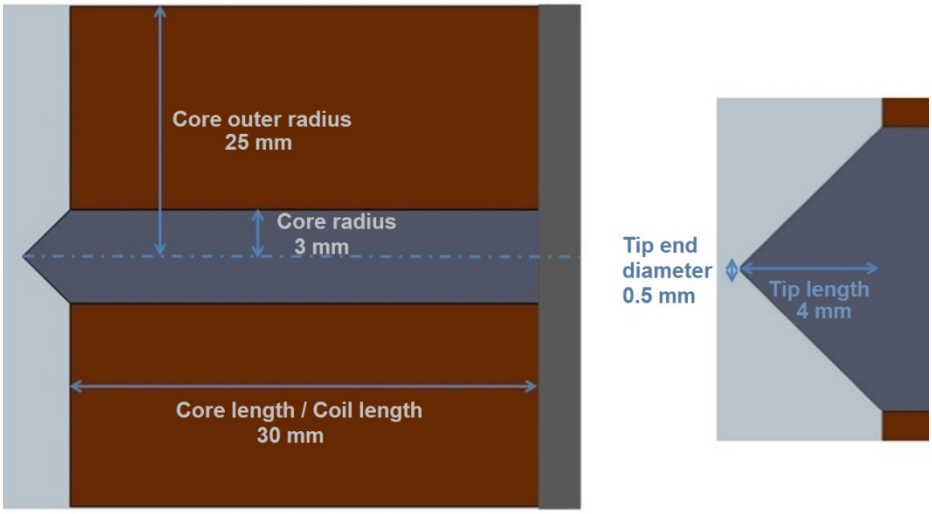

Figure 3.6 Cross section of the magnetic actuator.

The frequency response was a major consideration when designing the coil. Skin effect at high frequency causes the current density to increase close to the surface of the coil and exponentially decrease towards the middle, the effective cross-sectional area of the wires will reduce and the resistance of the wire will increase. The penetration skin depth δ can be approximated with equation:

$$\delta = \sqrt{\frac{\rho_c}{\pi f \mu_r \mu_0}} \tag{3.15}$$

where ρ_c is the resistivity of the wire in $\Omega \cdot m$, f is the frequency, μ_r is the relative magnetic permeability and μ_0 is the vacuum permeability. The diameter of the coil was chosen to be $0.71\ mm$, the skin depth is $225\ \mu m$ at $33767\ Hz$.

The magnetic field generated from the coil with DC current was characterised experimentally. The magnetic field density was measured by a micro-hall sensor (Nanomagnetics Ltd, Ankara, Turkey) with of $1\ \mu m^2$ sensing area, the distance between the coil and the sensor was controlled by a precision stage. The experimental set up and measurement results are shown in Figure 3.7 [96] .

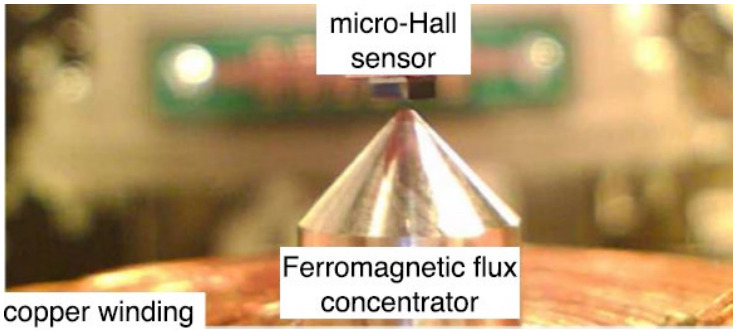

(a)

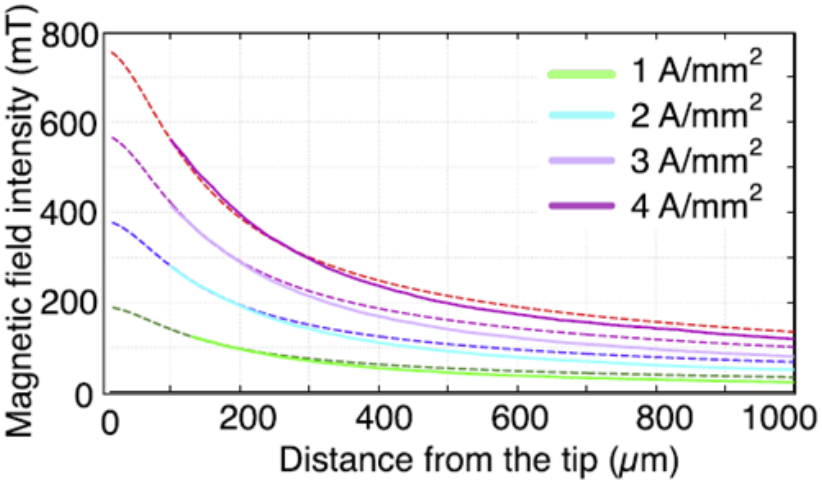

(b)

Figure 3.7. (a) Experimental set up to measure the magnetic field density at different distance from the tip. (2) Double exponential curve fittings for different current densities on the coil, dash point curves are the simulation results and solid curves are the fitted experimental results [96] .

The magnetic field intensities B as a function of distance from the tip for applied current densities were fitted with double exponential curves using equation (3.16), the fitted parameters for current densities of $3\ A/mm^2$ and $4\ A/mm^2$ are shown in Table 3.1. Magnetic field density of $0.55\ T$ can be achieved at $100\ \mu m$ working distance with $4\ A/mm^2$ current density.

$$B = a \cdot e^{bx} + c \cdot e^{dx} \tag{3.16}$$

Table 3.1. Parameters using double exponential fitting.

Current Density	a (mT)	b (mm^{-1})	c (mT)	d (mm^{-1})
3 A/mm^2	468.1	-0.0061	177.8	-0.00082
4 A/mm^2	605.7	-0.0057	228.4	-0.00068

A commercial CoCr coated cantilevers (MESP, Bruker) with calibrated spring constant of $1.12\ N/m$ was used for the force characterisation, the measurement setup was the same as Figure 3.7 (a). The measurements were performed in air, a transconductance amplifier was used to drive the magnetic coil with $0.3\ A$ square waves from $10\ Hz$ to $10\ kHz$ while the actuation force on the cantilever was measured. Figure 3.8 shows the time response and frequency response of the force on the cantilever. Both the time response and frequency response indicate that the magnetic actuator is capable of the $1\ kHz$ actuation bandwidth target in this study. Since during electromagnetic actuation, the piezo actuator where anchors the cantilever is switched off , the setup is able to resolve force below $5\ pN$ when using a cantilever with spring constant of 0.06 N/m, which is about twice the integral PSD over measurement bandwidth [96] .

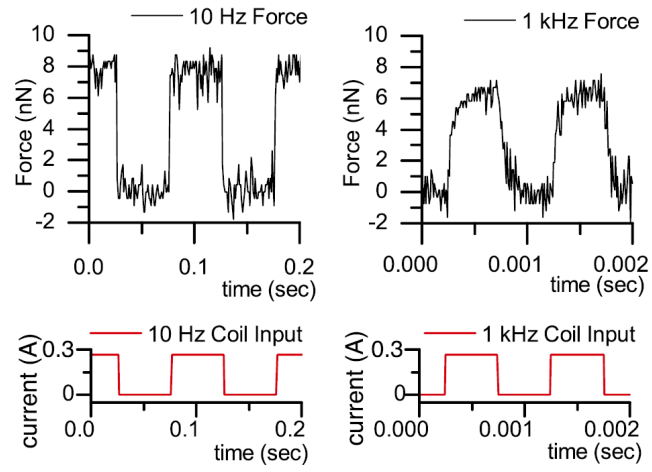

(a)

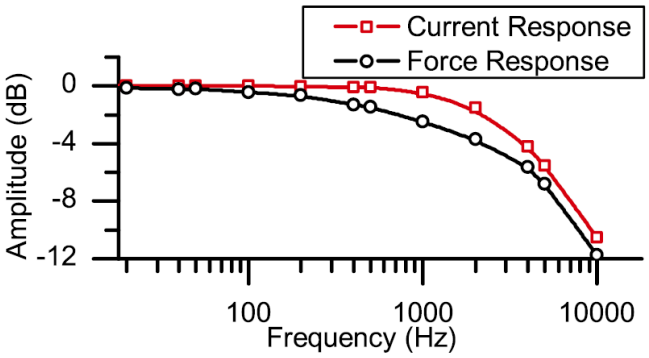

(b)

Figure 3.8. Force characterisation of the electromagnetic actuator. (a) Time response of force when the coil is actuated with 10 Hz (left) and 1 kHz (right) square wave current, (b) frequency response [96] .

Thermal analysis of the electromagnetic actuator was performed experimentally by placing a sub-mm size thermistor in the liquid meniscus and using a thermoelectric cooler (TCE) that controlled by a PID controller as sample surface. The distance between the core tip and the thermistor was kept similar to that from the cantilever tip in actual experiments. Figure 3.9 shows the measured temperature in meniscus when the coil was driven with $1.8\ A$ square wave current at $0.2\ Hz$. The initial temperature is 25.9 ℃, the current was turned on at $5\ min$ and turned off at $100\ min$, the PID controller was turned on at $53\ min$ and the final temperature was 32.5 ℃ [96] .

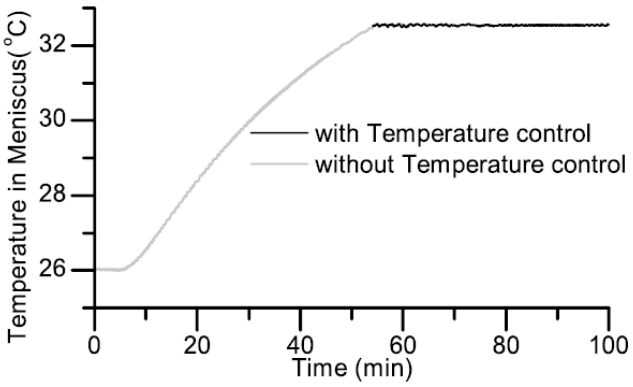

Figure 3.9. The thermal analysis of the electromagnetic actuator [96] .

4. MODELLING OF THE AFM AND THE SOFTWARE CONTROLLER

4.1 Modeling

The schematic of the customised AFM system is shown in Figure 4.1 [109] . It can be decomposed into four subsystems during simulation: the AFM head force sensing system which includes piezo, cantilever and photodetector; the molecules and bead; the electromagnetic actuator and the software controller.

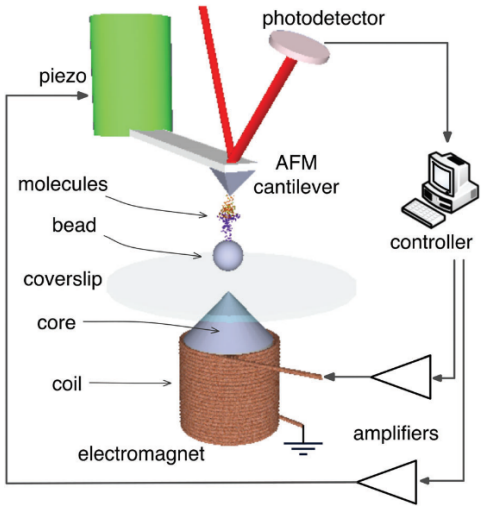

Figure 4.1. The schematic of the customised AFM [109] .

4.1.1 Force sensing system

Piezo

When nonlinear effects are ignored the piezo can be modelled as follow:

$$\Delta Z = k_{piezo} \Delta V \tag{4.1}$$

where ΔV is the change of the voltage applied on the piezo, k_{piezo} is the piezo coefficient, as mentioned in chapter 2 it's 1.5 $\mu m/V$. During force clamp experiments using electromagnetic actuation the piezo is kept stationary, thus $\Delta V = 0,\ \Delta Z = 0$.

Cantilever

The AFM cantilever was modelled as a lumped-element model consisting of effective mass m_e connected by a massless spring with spring constant k and a massless damper with coefficient b [110] as schematically shown in Figure 4.2.

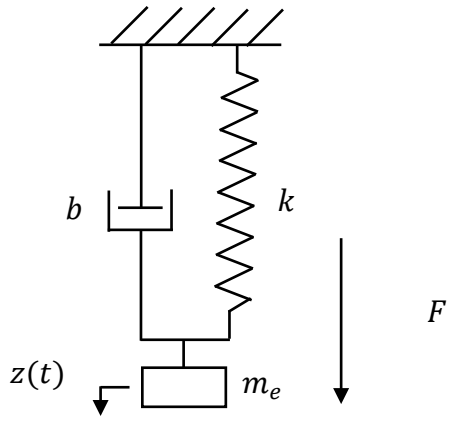

Figure 4.2. Lumped-element model of the cantilever.

When the force acting on the cantilever tip in vertical direction is F, the displacement in corresponding direction z and the force can be written as:

$$m_e \frac{d^2z}{dt^2} + b\frac{dz}{dt} + kz = F \tag{4.2}$$

The MATLAB Simulink simulation and result are shown in Figure 4.3, assuming that the effective mass which was obtained from the manufacturer is $5.17 \times 10^{-12}\ kg$, damping coefficient is $3.6 \times 10^{-7}\ kg/s$, which was obtained by fitting the resonance frequency

and Q factor to the second order system model, spring constant is $0.01\ N/m$, which is the nominal value of the MLCT-C (Bruker) cantilever, $100\ pN$ step force starts at $1\ ms$.

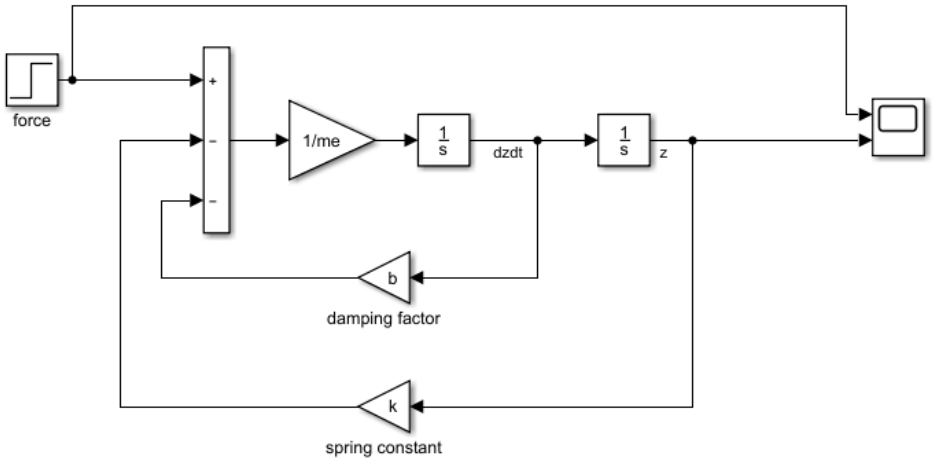

(a)

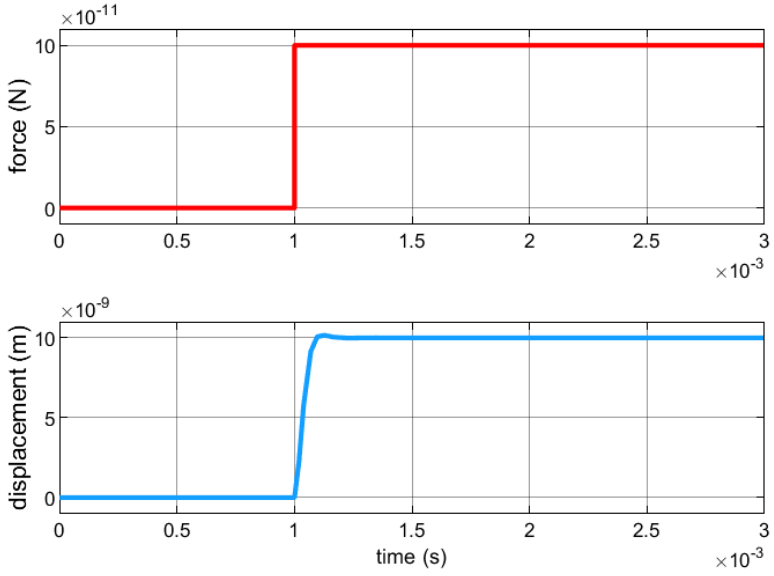

(b)

Figure 4.3. Lump-element model of a cantilever using Simulink. (a) Simulink model, (b) step response.

Optical path

As mentioned in chapter 2, the displacement change of the cantilever tip position z can

be calculated as the voltage change ΔV of deflection signal on the photodetector multiply by deflection sensitivity DS:

$$z = DS \cdot \Delta V \tag{4.3}$$

4.1.2 The bead and the molecules

The Bead

The forces on a biomolecule coated magnetic bead consists of electromagnetic pulling force F_{mag}, gravitational force F_{grav}, molecule pulling force $F_{molecule}$ and hydrodynamic drag force F_{drag} as shown in Figure 4.4.

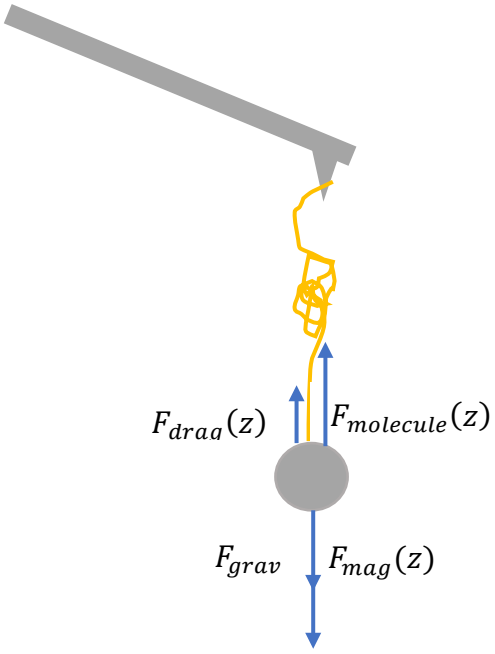

Figure 4.4. Force on the biomolecule coated magnetic bead.

When only consider the forces involved in z axis, in equilibrium [111] :

$$F_{molecule} = F_{mag}(z) + F_{grav} - F_{drag}(z) \tag{4.4}$$

According to Stokes' formula for viscous drag:

$$F_{drag}(z) = 6\pi\eta R_b \frac{dz}{dt} \tag{4.5}$$

where η is the viscosity of the liquid, the PBS used in experiment was water-based salt solution and the experiments were conducted in room temperature, a value of 1cP ($10^{-3} kg \cdot m^{-1}s^{-1}$) was taken throughout the analysis. R_b is the radius of the magnetic bead which is $1.4\ \mu m$.

Since the magnetic bead diameter is comparable to its distance from the coverslip surface z which was generally $5\ \mu m$ during actual experiments, thus extra correction terms for the enhancement of the hydrodynamic drag due to the presence of the surface [112] :

$$F_{drag}(z) = 6\pi\eta R_b \left(1 + \frac{R_b}{Z} + \frac{R_b}{2R_b+6Z}\right)\frac{dz}{dt} \tag{4.6}$$

The gravitational force can be calculated as:

$$F_{grav} = \frac{4}{3}\pi {R_b}^3 \rho g \tag{4.7}$$

where density of the magnetic bead $\rho = 1.4 g/cm^3$ was characterised by other researchers, g is the gravitational constant [106] .

Figure 4.5 shows the Simulink model of the force on the bead, rest of the input and output ports will be discussed later on.

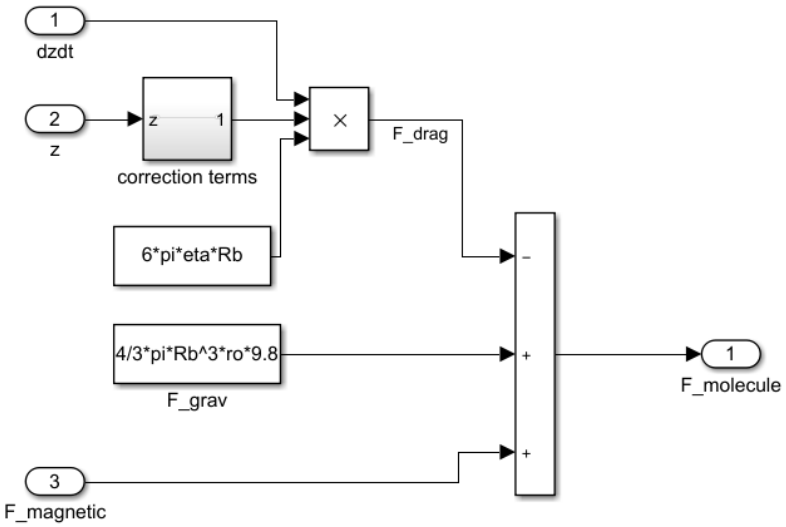

Figure 4.5. Simulink model of force on the magnetic bead.

The Molecules

The mechanism of biomolecular bonds elongate under mechanical stimulation remains unclear and yet to be explored [113] . Furthermore, the average size of protein is about a few nanometres in diameter, the distance between donor and accepter protein measured by fluorescence resonance energy (FRET) and fluorescence lifetime imaging (FLIM) is also in the order of a few nanometres [114] , both are very small compare to the size of the magnetic bead. Therefore, during simulation, the molecule size was ignored, the molecular bond was assumed to be rigid, therefore the pulling force applied on the molecule from the magnetic bead was the same as the force the molecule exerted on the cantilever tip.

4.1.3 Electromagnetic actuator

Electrical characteristics of the coil

The lumped-element model of the electromagnetic manipulator was characterised experimentally by applying $1\,A$ sinusoidal current to the coil and measured the coil

impedance and voltage phase shift. The experimental result and fitted lump-element model is shown in Figure 4.6, the parallel 4.4 $k\Omega$ resistor is the equivalent output impedance of the coil drive amplifier.

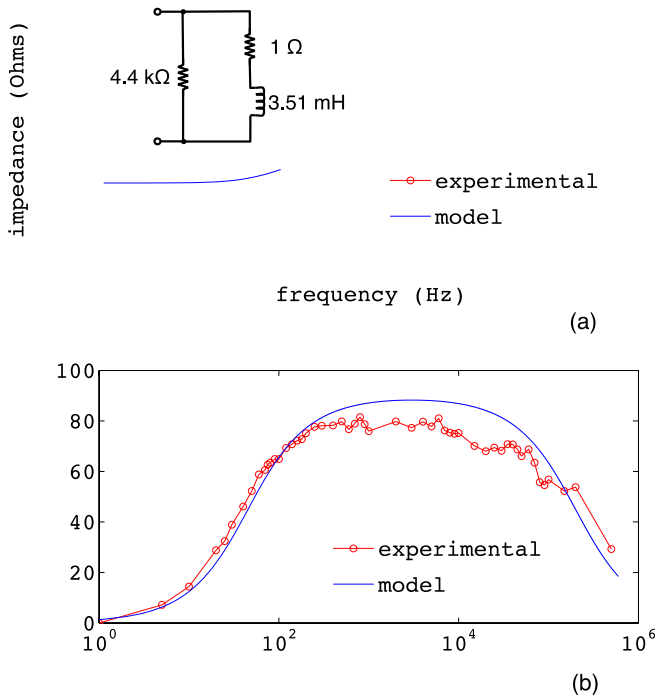

Figure 4.6. Electrical characterisation of the electromagnetic actuator. (a) Impedance change corresponding to frequency and the fitted lumped-element model, (b) phase shift of the voltage across the coil.

Magnetic field and magnetic force

The magnetic field gradient generated by the electromagnetic actuator was simulated based on the double exponential fitting derived from the measurements of magnetic field B discussed in chapter 3:

$$B(z_c) = a \cdot e^{bz_c} + c \cdot e^{dz_c} \tag{4.8}$$

where B is the measured magnetic field intensity, z_c is the distance from the core tip,

other parameters are shown in Table 3.1.

The magnetic gradient can be approximated as:

$$\nabla B = \frac{B(z_c) - B(z_c - \Delta z_c)}{\Delta z_c} \tag{4.9}$$

where z_c is the distance from the core tip to the magnetic bead in vertical direction, the magnetic bead was idealised as a point particle during simulation.

The Simulink model of magnetic field gradient generated by the electromagnetic actuator is shown in Figure 4.7, the simulated magnetic field gradient at distance from 0 to $500\ \mu m$ is shown in Figure 4.8 (a) which have good agreement with Figure 4.8 (b) the derivative of experimental measurement of the magnetic field B with respect to distance from the tip.

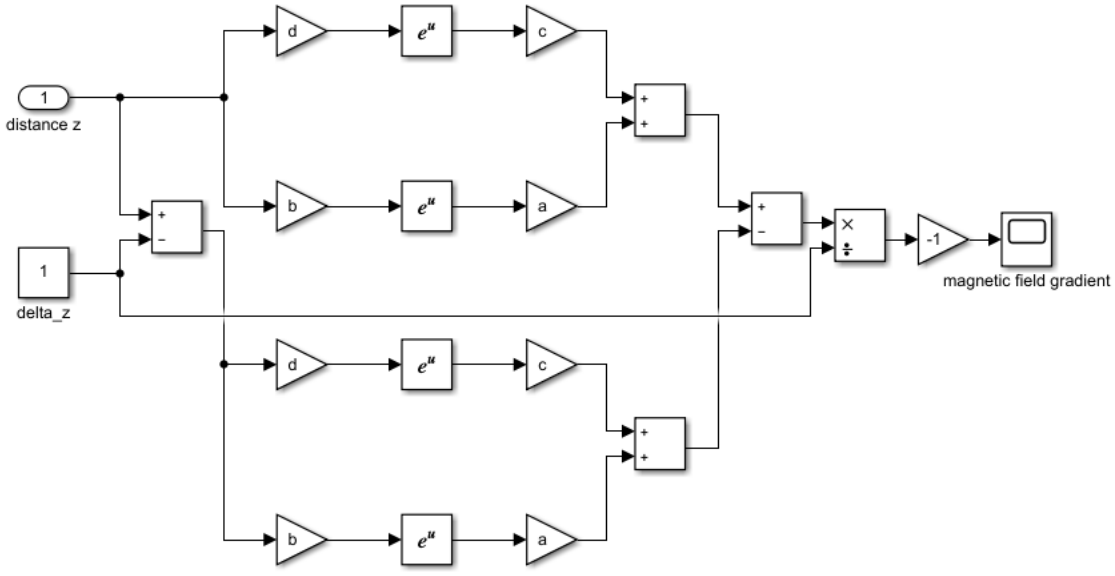

Figure 4.7. Simulink model of magnetic field gradient from electromagnetic actuator.

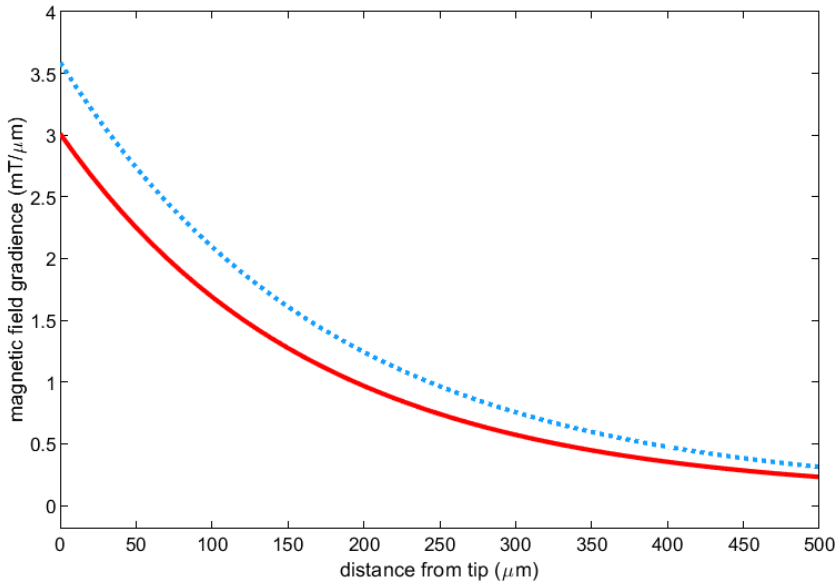

(a)

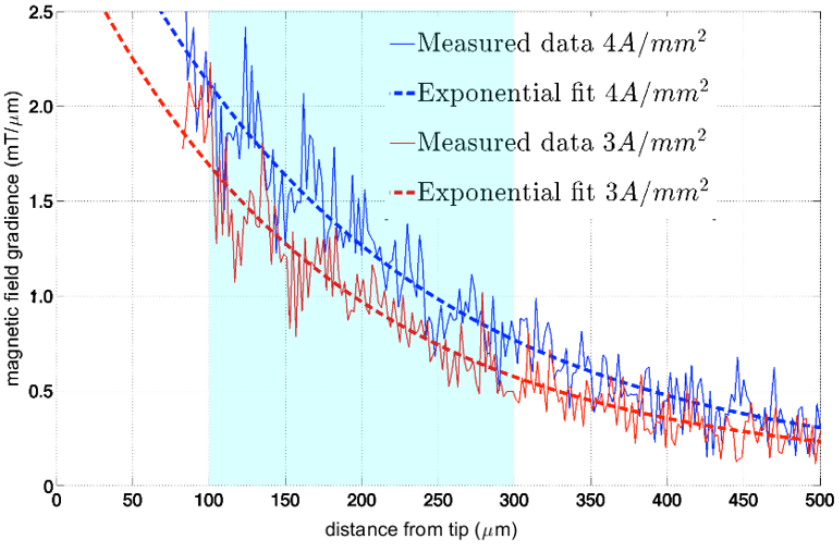

(b)

Figure 4.8. The magnetic field gradient generated by the electromagnetic actuator with respect of distance from the core tip. (a) Simulink simulation result and (b) calculation from experimental measurement with current density of 3 A/mm^2 and 4 A/mm^2 show in red and blue curves respectively, y-axis is the magnetic field gradient (mT/μm).

Transconductance Amplifier

A commercial power amplifier (AE Techron 7224, IN, USA) with adjustable gain was

used to drive the coil for magnetic actuation during experiments. For simplicity the amplifier was modelled ideally by ignoring non-linear effect and simplified as an adjustable gain k_A.

Magnetic force applied on magnetic bead

The magnetic force applied on the magnetic bead depends on the magnetic field gradient, which already discussed in chapter 3. However, the magnetic field, thus the gradient, generated by the electromagnetic actuator is also function of the current I applied on the coil which was not measured in detail in this study, therefore during simulation it's approximated by assuming the magnetic field gradient $\nabla B(z_c, I)$ at the same distance z_c is proportional to the current. The magnetic bead was also assumed to be saturated, therefore:

$$F_{mag} = \nabla(m_{sat}B) = m_{sat}\nabla B(z_c, I) \tag{4.10}$$

Then the magnetic force was modelled as Figure 4.9 (a). During simulation, the double exponential fitted parameters for current density of $3A/mm^2$, which corresponds to 1.2 A current on the coil in this study, were used as reference to calculated the B field generated by other current. In simulation, the magnetisation was $m_{sat} = 10.8\ Am^2/kg$ [106] . The simulated magnetic force on the bead in Figure 4.9 (b) is $380\ pN$ at $100\ \mu m$ and $130\ pN$ at $300\ \mu m$, the effective stiffness of the magnetic actuation is low enough, which indicates that the electromagnetic actuation can afford passive force clamp.

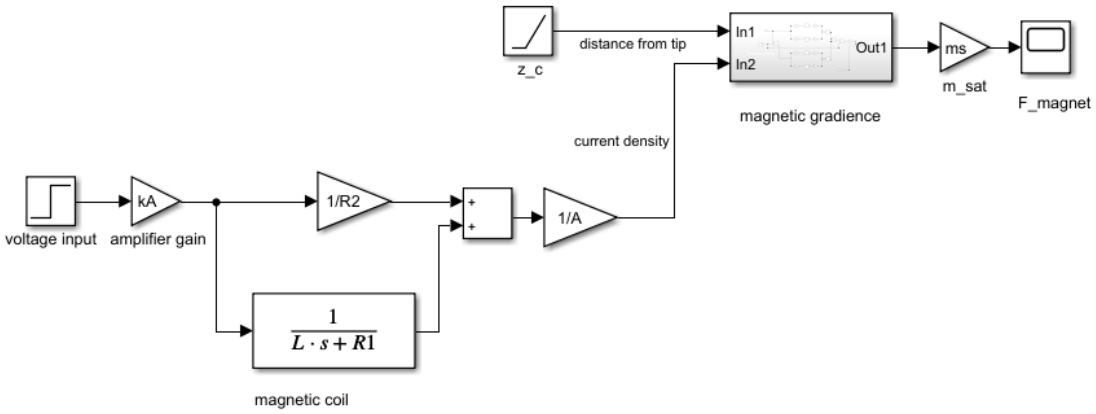

(a)

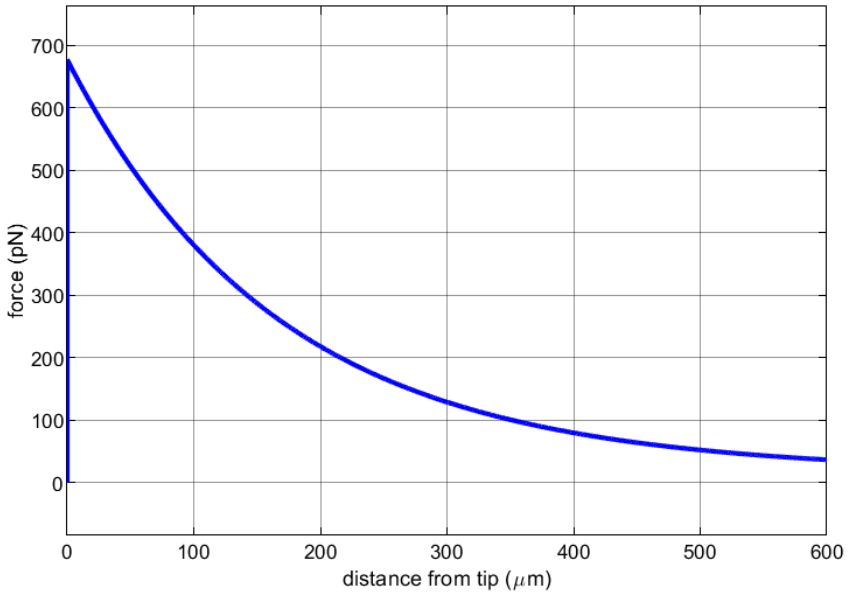

(b)

Figure 4.9. Magnetic force applied on the bead. (a) Simulink model, (b) magnetic force.

4.1.4 The AFM system

Since the molecule was assumed to be rigid, the total force on the magnetic bead was the same as the force on the cantilever tip, the relative distance z and the speed $\frac{dz}{dt}$ of the cantilever were also the same as those of the bead. Based on this assumption, the whole

system, shown in Figure 4.10, was modelled by connecting the subsystems discussed above.

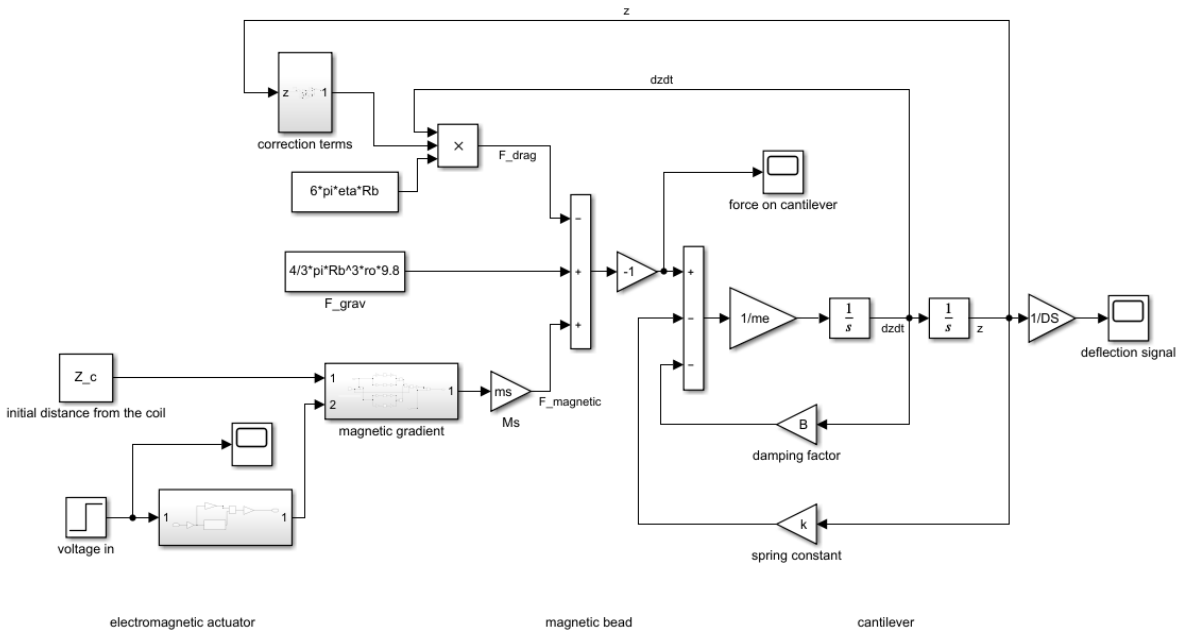

Figure 4.10. Simulink model of the AFM system.

The initial distance between the cantilever and the core tip was $200\,\mu m$, the initial distance between the magnetic bead and the coverslip was $5\mu m$. $1\,V$ step input voltage started at $0.1\,s$ was applied to the coil drive amplifier, the current density on the coil was about $4\,A/mm^2$, the sensitivity of the cantilever was $0.5\,\mu m/V$, which was within the practical range. The simulated time response of the force on the cantilever tip and the deflection is shown in Figure 4.11, according to the result in Figure 4.11 (b), it takes about $10\,ms$ for the force and deflection to reach maximum, the 14 mV deflection signal in Figure 4.11 (c) on the photodetector is also very easy to be observed in practice. The analysis and simulation provided basic understanding of the AFM system which facilitated the design of the AFM software controller.

Then the initial distance between the cantilever and the core tip was kept $200\,\mu m$, the voltage applied to the coil drive amplifier was set to constant $1\,V$, the distance was swept from 0 to $15\,\mu m$ in a speed of 1 $\mu m/s$, as shown in Figure 4.12 (a), which covered the

full range of the piezo actuator. In practice, the range that used the most will be $5\ um$ to $10\ um$. The simulated force on the magnetic bead is shown in Figure 4.12 (b), the force at $5\ um$ is $69\ pN$, at $10\ um$ is $67\ pN$. Accordingly, the deflection signal shown in Figure 4.12 (c) at $5\ um$ is $13.72\ mV$, at $10\ um$ is $13.35\ mV$.

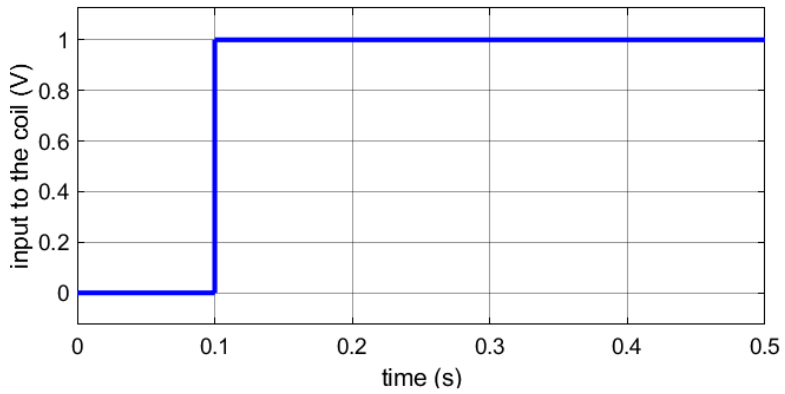

(a)

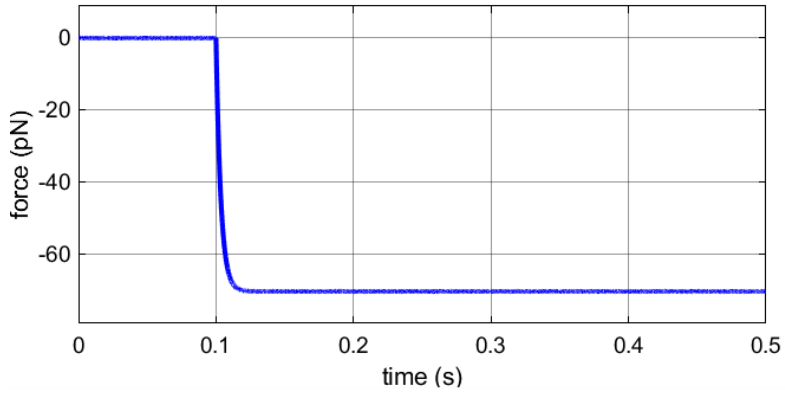

(b)

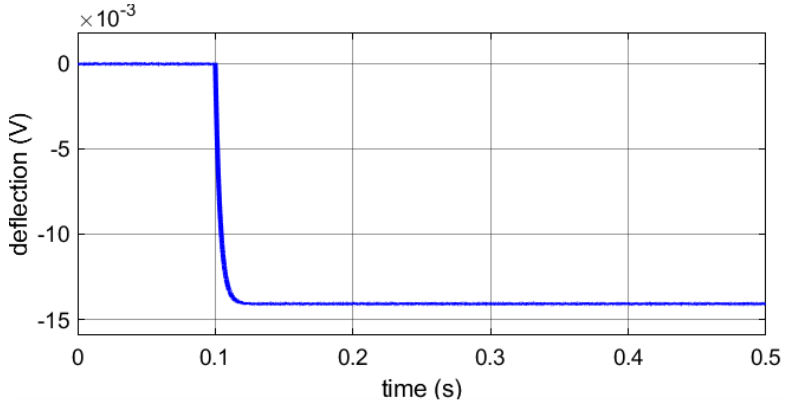

(c)

Figure 4.11. Time response of the AFM system. (a) Step input voltage to the coil drive amplifier, (b) corresponding force on the cantilever, (c) deflection of the cantilever.

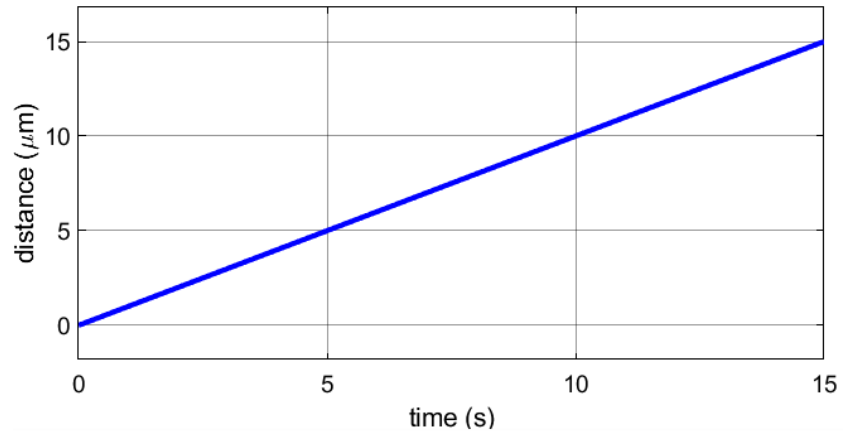

(a)

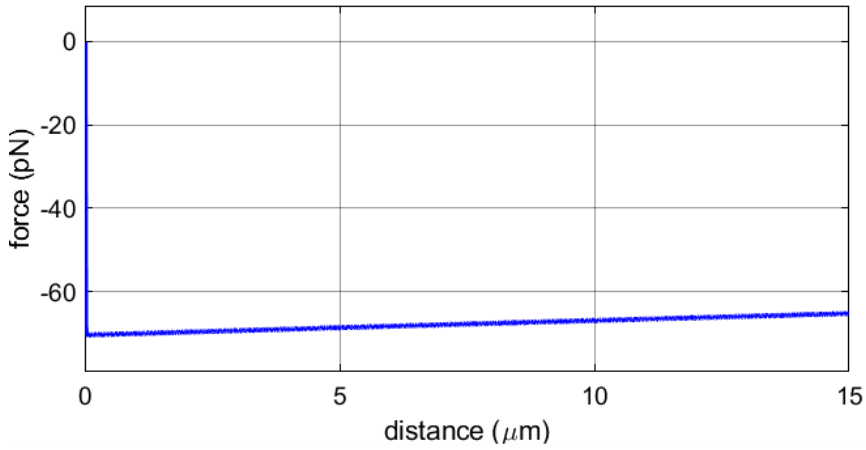

(b)

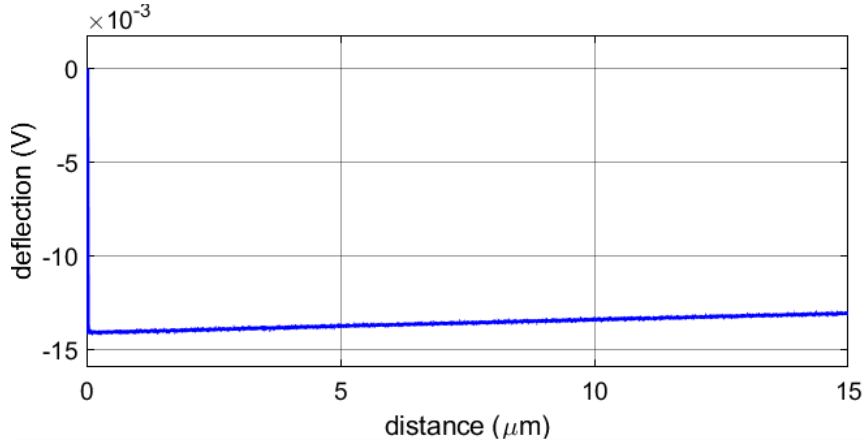

(c)

Figure 4.12. Magnetic bead distance sweeps the full actuation range of the piezo actuator where the initial distance is 200 µm. (a) Distance from the initial, (b) force change on the bead according to distance, (c) deflection signal on the photodetector.

4.2 Data Acquisition

Figure 4.13 shows the block diagram of the electronics of the AFM system. The data acquisition was realised by a DAQ card (NI-PXIe 6365, National Instruments, TX, USA) controlled by a PXI (PCI extensions for Instrumentation) embedded controller (NI PXI-8102, National Instruments, TX, USA). Four analog input channels are reserved for Top-Bottom, Left-Right and SUM signals of the photodetector and the current on the coil. Two analog output channels are utilised for sending signals to the power amplifier and the piezo amplifier that is responsible to piezo actuator.

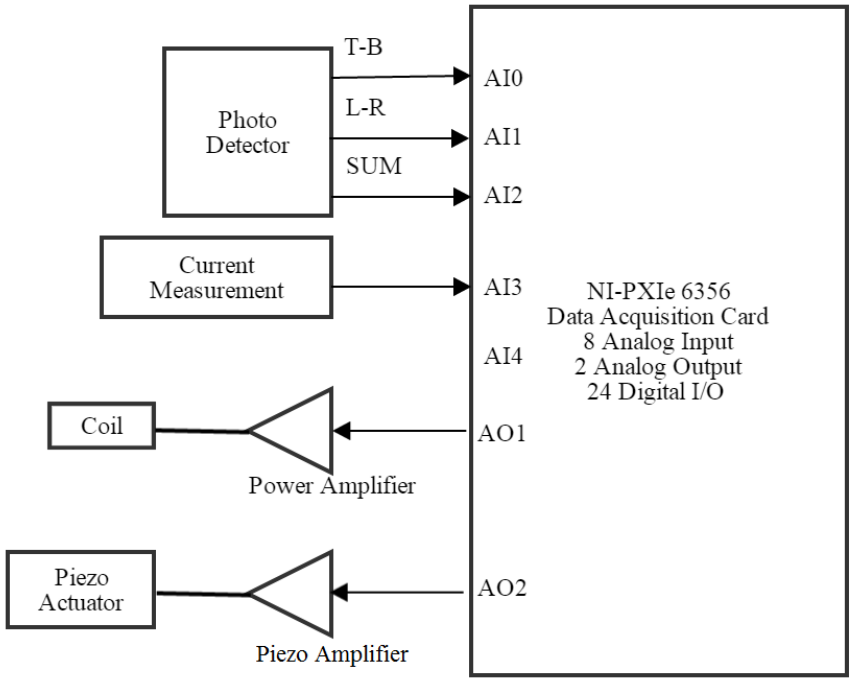

Figure 4.13. Block diagram of the AFM system.

All software controllers were programmed on LabView. The VIs for different functions were programmed in modules and readily to be packed into one VI.

4.3 The VI for Pulling Experiment

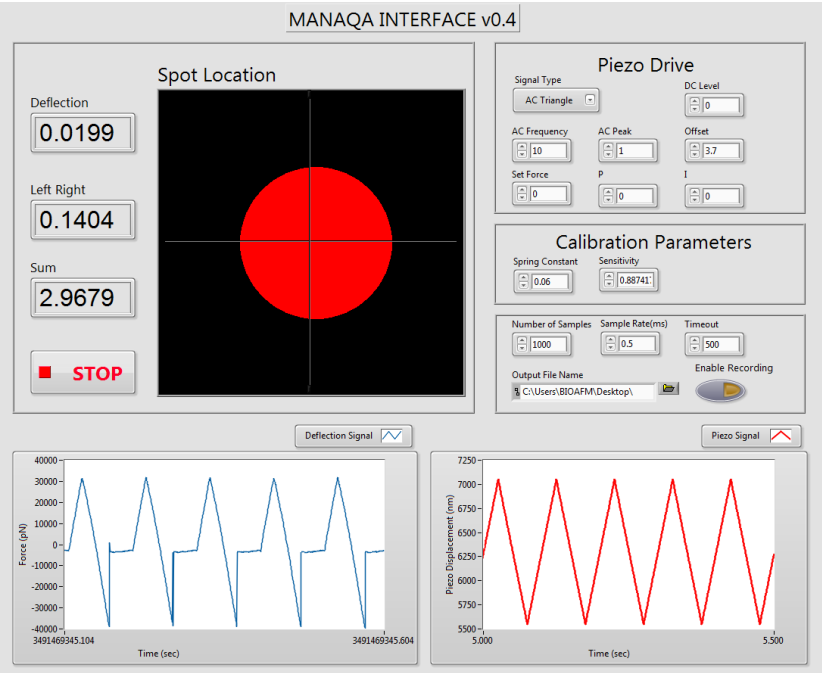

Figure 4.14. User interface of pulling experiment VI.

The interface for pulling experiment is shown in Figure 4.14. This VI is used for laser alignment and sensitivity calibration. It can also be used for conventional pulling experiments. The location of the laser spot on the photodetector is shown graphically and numerically. The output piezo signal can be adjusted from the Signal Type menu, the options are DC, AC-sine, AC triangle and Custom that can be defined by the user. The deflection signal and piezo displacement signal are displaced at the bottom.

When the laser is aligned the deflection sensitivity of the cantilever can be measured in a few steps. First set the Piezo Drive signal to AC Triangle wave with DC offset, generally 5V, which is half of the maximum voltage output of the DAQ card, thus can provide the freedom to move the cantilever upwards and downwards by adjusting voltage. Then the cantilever is brought into contact with the surface manually as discussed in chapter 2, meanwhile the deflection signal can be observed on the waveform chart until a waveform

similar to the Deflection Signal in Figure 4.14 appears. The large adhesion in the sample here is due to the capillary force between the cantilever and the coverslip.

This VI can also be used to perform conventional pulling experiments using piezo actuation. The pulling speed of the piezo can be adjusted by changing the frequency or the amplitude of the triangle signal from Piezo Drive block.

4.4 Force Clamp Experiments

4.4.1 Software structure

The block diagram of the VI for force clamp experiments using electromagnetic actuator is shown in Figure 4.15. The VI includes 5 major functioning blocks, namely pickup beads, force-clamp pulling, adjust zero-force offset, buffer and data storage. The first three are connected in a loop that following the experiment routine, a state machine is used to switch among the three functions sequentially. These three blocks require precision timing and prompt response, therefore they are placed in timed loops that are executed in a higher priority with different timing. Data recording is in lower priority which doesn't require timing. The measured data are first streamed into the buffer then waited in queue to be written on hard drive. This structure that decouples different function blocks in different loop rates is called producer-consumer structure. 5 samples are taken in each loop, the average of the 5 samples are used for the error calculation for feedback control, the original sampled data are recorded.

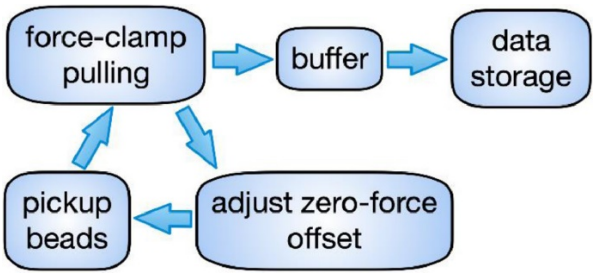

Figure 4.15. Block diagram of the controller software [49] .

4.4.2 Force clamp pulling

The force clamp pulling block was programmed into two modes, the feedback ON mode with closed-loop active feedback control that keeps the force constant on the cantilever and feedback OFF mode which keeps the applied current constant on the magnetic coil with open loop output.

In feedback ON mode, a PID controller was programmed to drive the coil amplifier of the AFM system, the block diagram is shown in Figure 4.16. The error between the setpoint force and the observed deflection signals are compensated by the required actuation determined with PID algorithm. PID controller has historically been considered to be one of the most powerful controllers even when detailed knowledge of the system is absent [115] [116] . A velocity PID algorithm was chosen for the closed-loop controller in this research because it can avoid large sudden changed of output and windup.

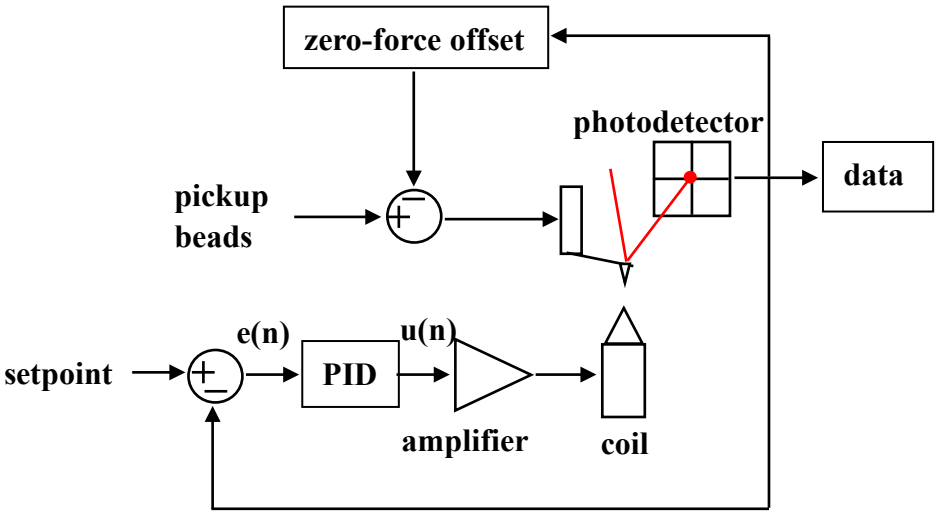

Figure 4.16. Block diagram of the feedback controller and AFM system.

The output of the PID controller $u(t)$ is the voltage sent to the power amplifier during magnetic actuation. For a continuous time system $u(t)$ can be modelled as follow:

$$u(t) = K_p \left\{ e(t) + \frac{1}{T_i} \int_0^t e(t)dt + T_d \frac{de(t)}{dt} \right\} \tag{4.11}$$

where K_p is the proportional gain, T_i is the integral time, T_d is the differential time.

It can be discretised for a discrete-time system as:

$$u(n) = K_p \left\{ e(n) + \frac{T}{T_i} \sum_{j=0}^{n} e(j) + \frac{T_d}{T} [e(n) - e(n-1)] \right\} \tag{4.12}$$

where T is the sampling time of the discrete-time system.

The incremental output to piezo $\Delta u(n)$ then can be expressed in terms of error $e(n)$ and constants as below:

$$\Delta u(n) = u(n) - u(n-1) \tag{4.13}$$

and

$$T_i = K_p/K_i \tag{4.14}$$

$$T_d = K_d/K_p \tag{4.15}$$

where K_i , K_d are integral and derivative gain respectively.

Therefore, the incremental actuation signal is:

$$\Delta u(n) = \left(K_p + K_i T + \frac{K_d}{T}\right) e(n) - \left(K_p + \frac{2K_d}{T}\right) e(n-1) + \frac{K_d}{T} e(n-2) \tag{4.16}$$

All signals are converted into voltage in the implementation, the clamping force F_c is converted into voltage V_c:

$$V_c = \frac{10^{-6} F_c}{k \cdot DS} + V_0 \tag{4.18}$$

where k is the spring constant of the cantilever, V_0 is the deflection offset when cantilever is out of contact with the surface, DS is the deflection sensitivity.

The error $e(n-1)$ and $e(n-2)$ are realised by feedback node with different delay. The derivative term can predict error and decrease overshoot theoretically, in practice, it is very sensitive to noise, therefore K_d is usually set to be very small or zero.

In feedback OFF mode, the PID feedback algorithm is replaced by a constant DC voltage.

5. BIOMOLECULAR EXPERIMENTS

Biomolecular experiments using two different pairs of molecules were performed in this research. The first pair, biotin-streptavidin, has been widely studied and was used to validate the system. The second pair, heparin-FGF2, was selected to gather new data to understanding how the molecules interact with each other. Both pulling and force clamp methods were used to investigate these two molecular pairs. Schematics of three types of experiments using biotin-streptavidin pair are shown in Figure 5.1. The schematics of heparin-FGF2 pulling experiments using piezo actuation are similar to that shown in Figure 5. 1 (a), the schematics of heparin-FGF2 pulling experiments using magnetic actuation and force clamp experiments are similar to that shown in Figure 5.1 (c). In this chapter, the biomolecules are briefly introduced, materials, methods and experimental results are also discussed.

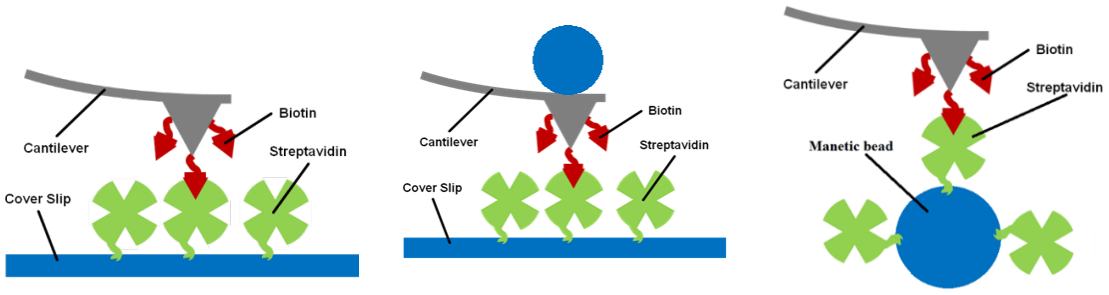

(a) (b) (c)

Figure 5.1. Schematics of experiments using biotin-streptavidin pairs. (a) Pulling experiment using piezo actuation, (b) pulling experiment using magnetic bead attached cantilever, (c) force clamp experiment using streptavidin functionalised magnetic beads.

5.1 Molecular Pulling Experiments Using Biotin-Streptavidin Pairs

Biotin-streptavidin molecular force spectroscopy experiments based on pulling methods were performed using the customised AFM system. Both piezo actuation and electromagnetic actuation methods were used during the experiments.

The mechanics and the dynamics of the biotin-streptavidin complex have been characterised in detail [117] . Streptavidin is a tetrameric protein that has very high affinity to biotin molecules, the binding of the pair exhibits one of the strongest non-covalent bonds in nature [118] . These make the pair especially suitable for initial experiments using our customised AFM setup.

5.1.1 Sample preparation

For biotin-streptavidin pulling experiments using piezo actuation, biotin coated cantilevers (CT.BIO, Novascan, Ames, IA USA) on which biotin is covalently bonded and substrate uniformly coated with immobilised streptavidin (VXP0010, Xenoprobe) were used.

Molecular pulling experiments where cantilevers were actuated magnetically were also performed. For this purpose, a ferromagnetic bead with diameter of $30\ \mu m$ was glued on the back side of tip of a cantilever (MLCT-C, Bruker Probes) and the cantilever was functionalised with biotin using physical absorption method [119] . The nominal spring constant of this cantilevers is $0.01\ N/m$ and was calibrated before the experiments using thermal tune calibration method. $20\ \mu L$ of streptavidin solution with initial concentration of $10\ mg/100\ \mu L$ was diluted with $50\ \mu L$ of Phosphate-buffered saline (PBS, Sigma-Aldrich) buffer solution for three times. $20\ \mu L$ droplet of diluted streptavidin solution was placed in the centre of the coverslip for 15 minutes at room temperature and removed afterwards with pipet to covalently bond a layer of streptavidin on the coverslip surface.

Laser was aligned with the method discussed in chapter 2, in experiments using magnetic actuation, the cantilever tip was also aligned with the electromagnetic core tip.

Then in both methods, the cantilever and coverslip surface were treated with $50\ \mu L$ of

bovine serum albumin (BSA, Sigma-Aldrich) with concentration of $40\ \mu g/mL$ for $15\ min$ to reduce non-specific adhesion, afterwards the BSA was removed with a pipette and $100\ \mu L$ droplet of PBS was placed on the coverslip. The cantilever was lower down towards the surface manually by adjusting the Vernier micrometre to form a meniscus for the experiment. All experiments were performed at room temperature.

5.1.2 Results

The concentration of molecules was adjusted so that the probability of specific unbinding events was ~30% during our experiments. This level allows us to resolve the interactions at single molecular level. If the molecular concentrations were higher, the interactions would include many pairs of molecules. If they were lower, the events would become highly rare. Control experiments were performed by saturating biotin on the cantilever with excess streptavidin, the probability of the specific unbinding events reduced to 1%. The significant reduction in specific events indicated the validity of the experiment protocol for this molecular pair [109] .

Figure 5.2 (a) shows a force curve with specific unbinding event, the unbinding force is about $200\ pN$, Figure 5.2 (b) shows a force curve where no unbinding event happens. During the approach cycle (black line), the biotin functionalised cantilever tip was lowered down onto the streptavidin coated sample surface, positive deflection signal was detected after contact. After the contact of the cantilever and the surface which allowed molecular bond formation, the cantilever was retracted back (red line). The loading rates of the molecular bond were measured using the slope of the portion below the relatively flat noncontact portion on the retract curve. The sudden jump on the retract curve indicated a single molecular bond rupture, the magnitude of the jump was measured as the unbinding force. About 100 force curves were recorded under each piezo speed, thus different loading rates. In this research, the loading rates were varied from $6 \times 10^2\ pN/s$ to $6 \times 10^6\ pN/s$, Figure 5.3 shows the histogram of unbinding force versus loading rates.

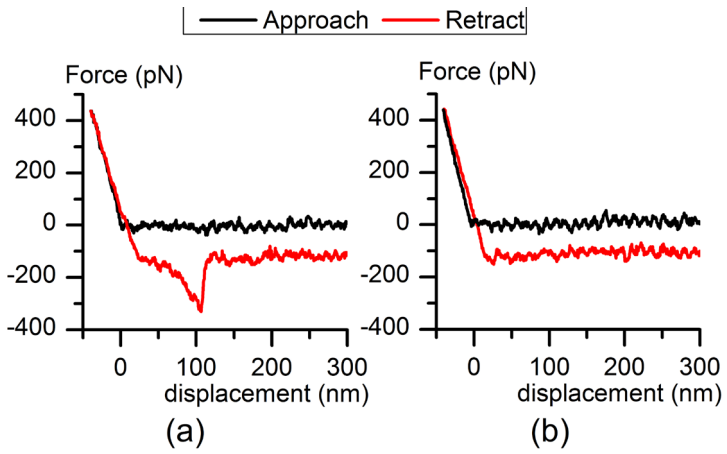

Figure 5.2. Sample force curves using piezo pulling method. (a) A specific biotin-streptavidin event with about 200 pN unbinding force, (b) no rupture event.

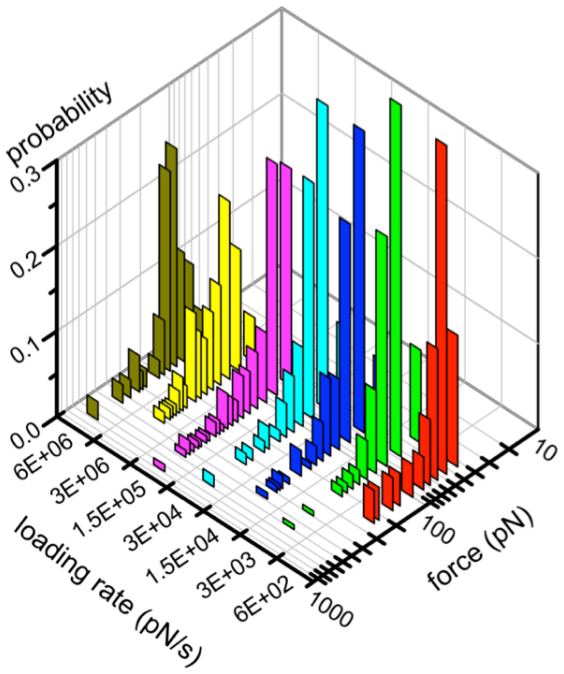

Figure 5.3. Histogram of probability of unbinding force versus loading rates using biotin-streptavidin piezo pulling [96] .

Figure 5.4 shows the sample force curves from experiment using magnetic bead attached cantilever and magnetic actuation. The states of the cantilever during the experiment are schematically shown. During the experiment, the cantilever was brought within the

vicinity of the sample surface by piezo actuation, then the bead attached cantilever was actuated by the electromagnet actuator. First, the cantilever was brought into contact with the sample surface by the magnetic force to allow the molecular bond formation, the displacement of the cantilever did not change during contact. Then the cantilever was released from the surface by decreasing the magnetic attraction force. Figure 5.4 (a) shows an example of specific event with unbinding force measured to be $285\,pN$, the loading rate was measure from the slop of unbinding force portion. Loading rates were varied between 10^3 to $10^5\,pN/s$ using magnetic actuation [96] .

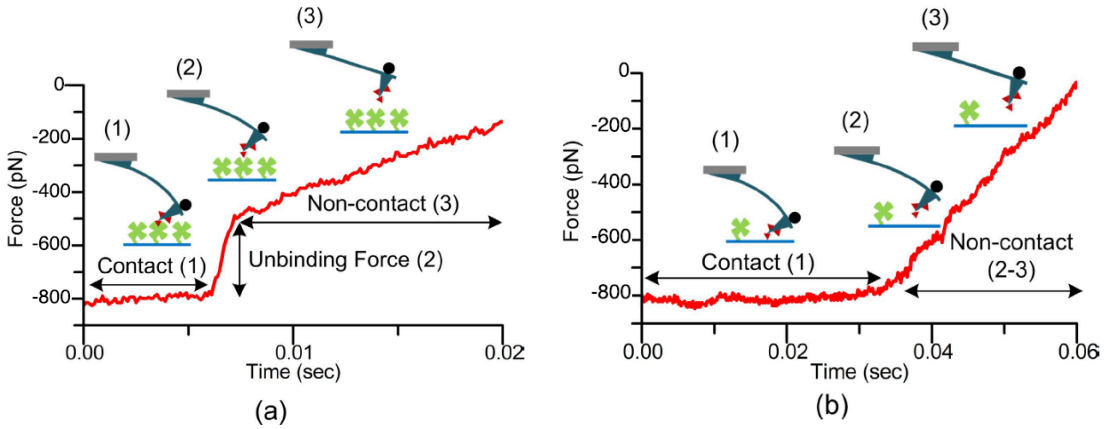

Figure 5.4. Force curves using magnetic bead attached cantilever and magnetic actuation (a) with specific unbinding force of 285 pN, (b) without event [96] .

For comparison, biotin-streptavidin pulling experiments were also performed on a commercial AFM system. The same type of cantilevers and samples were used, the preparation procedures were the same as that mentioned in the piezo pulling method. Figure 5.5 shows the loading rate versus most probable rupture force using piezo and magnetic actuation from the customised AFM and a commercial AFM, verifying that the customised AFM is capable of single molecular experiments [96] .

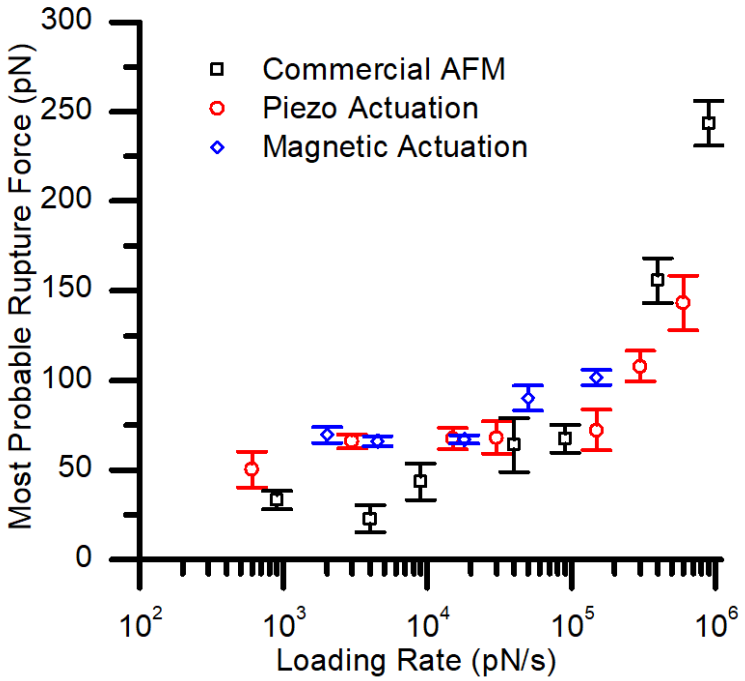

Figure 5.5. Loading rate versus most probable rupture force [96] .

The kinetics and energy landscape of the molecular bond were derived by fitting the measured distribution of force under each loading rate with equations (1.10) and (1.11) [120] [121] , the results are summarised in Table 5.1. In loading rate region until $10^5\,pN/s$, the calculated zero force dissociation rate K^0 and barrier width x_β are $6.41 \times 10^{-4}\,s^{-1}$ and $0.85\,nm$ respectively, in loading rate region between $10^5\,pN/s$ to $10^6\,pN/s$, the calculated K^0 and x_β are $7.14 \times 10^2\,s^{-1}$ and $0.07\,nm$ using piezo actuation in the customised AFM system, the calculated parameters from both loading rate regions show good agreement with the results from commercial AFM [49] .

Table 5.1 Bell's parameters of biotin-streptavidin interaction derived from experiments using customised AFM and commercial AFM

	Loading rate (pN/s)	K^0 (s^{-1})	x_β (nm)
Piezo actuation	1×10^2 to 1×10^5	6.41×10^{-4}	0.85
	1×10^5 to 1×10^6	7.14×10^2	0.07
Magnetic actuation	1×10^2 to 2×10^5	1.08	0.28
Commercial AFM	1×10^2 to 1×10^5	6.04×10^{-4}	0.48
	1×10^5 to 1×10^6	5.25×10^2	0.05

5.2 Biotin-Streptavidin Force Clamp Experiment

5.2.1 Sample preparation

Commercial biotin coated cantilevers (Novascan) and commercial magnetic beads (Dynabeads, M-280 Streptavidin, ThermoFisher) were used in force clamp experiments using magnetic actuation.

The magnetic beads were diluted before use. $1\ mL$ of PBS PH 7.4 washing buffer was added into a centrifuge tube, $5\ \mu L$ of resuspend Dynabeads was transfer into the tube and mixed with the buffer. The tube was placed on top of a magnet for $1\ min$, the supernatant was discarded. Then $1\ mL$ of PBS was added into the tube.

The cantilever and the core tip of the electromagnetic actuator were aligned. Then both the cantilever and coverslip were treated with $50\ \mu L$ of BSA for $15\ min$ to reduce non-specific adhesion. $100\ \mu L$ PBS was placed onto the cover slip, then $0.1\ \mu L$ of resuspend diluted beads were injected into the PBS on top of the magnetic coil tip. Then the cantilever was brought into the PBS to form meniscus. All the experiments were performed at room temperature.

5.2.2 Results

Force clamp experiments were performed using both controller ON and controller OFF methods discussed in chapter 4. Figure 5.6 is a typical force and current curve using controller ON method. In this example, the force, which corresponding to the total force applied on all the picked up magnetic beads on the cantilever, is $260\ pN$. A magnetic bead detaches from the cantilever at $1.42\ s$ due to a molecular bond rupture, the total number of beads, thus the force applied on the cantilever decreases. The current applied to the electromagnet is increased by about $0.2\ A$ to compensate the decreased force and to keep the total force constant, the details of the controller are discussed in chapter 4 [49] .

The force of the molecular bond was measured by the magnitude of the spike like rupture, the lifetime of the bond was measured as the timespan between the force reached setpoint and the rupture. In the force curve shown in Figure 5.6, the force and lifetime are $120\ pN$ and $1296\ ms$ respectively [49] .

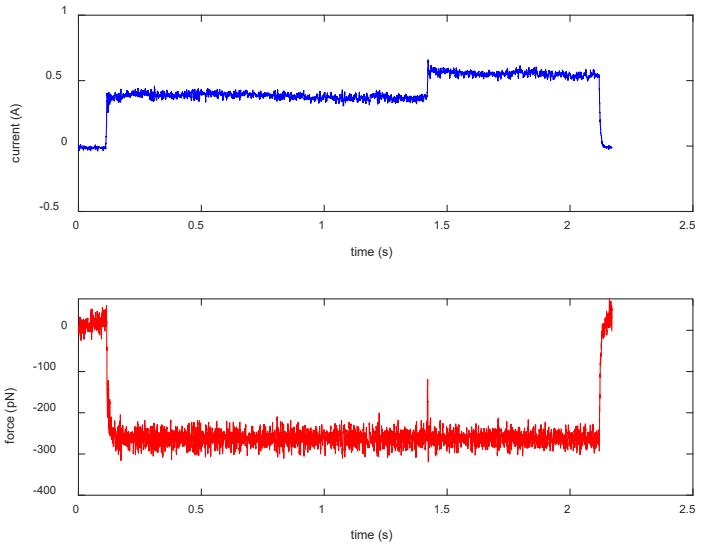

Figure 5.6. A sample force curve using feedback ON method.

Multiple ruptures were also observed in one force curve, an example is shown in Figure 5.7 where three rupture events can be observed clearly at about $700\ ms$ and two ruptures at about $900\ ms$ and $1600\ ms$ can be observed from the jump of the current. In this scenario the total force applied on the beads attached on cantilever is kept constant by the controller. The total force reduces when one of the beads detached from the cantilever, to keep the total force constant the current will immediately increase due the feedback compensation, the force on the remaining beads also increases. Therefore, the beads except for the first one, experience stepwise increasing force each time one of the beads falls down, the rupture force is overestimated. If the number of residual beads on the cantilever is large enough, the percentage error of the force can be ignored. However, the number of beads attached on the cantilever was unknown and was changing during the experiment, only the first unbinding event in each force curve was included in the subsequence statistical analysis in this research.

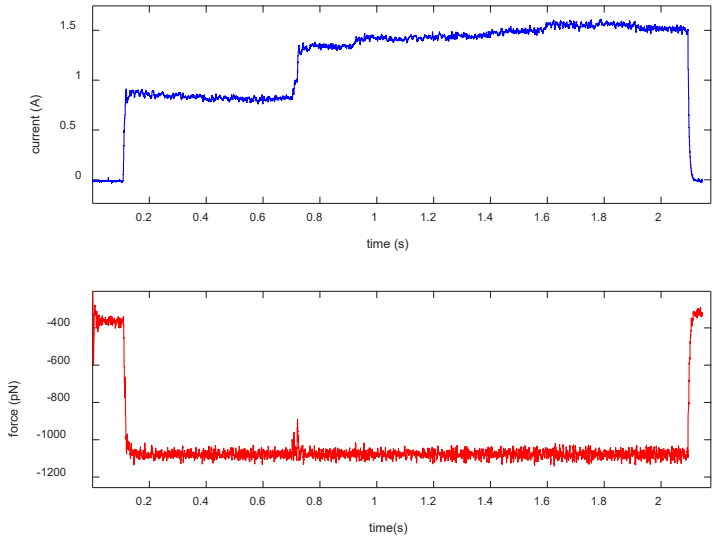

Figure 5.7. A sample force curve showing multiple events using feedback ON method.

Experiments at various clamping forces were performed. A total of 533 first unbinding events were obtained with force ranging from $35\ pN$ to $450\ pN$ [49]. These events were grouped by the magnitude of unbinding force to generate histograms of lifetime, these histograms were fitted by exponential probability density functions to estimate the lifetime under force [122]. An example of histograms of lifetime with force between

$45\ pN$ and $60\ pN$ is shown in Figure 5.8, the mean value of the force is $53\ pN$, the expected lifetime is 0.261 s with 95% confidential interval (0.211 s, 0.329 s) [49] .

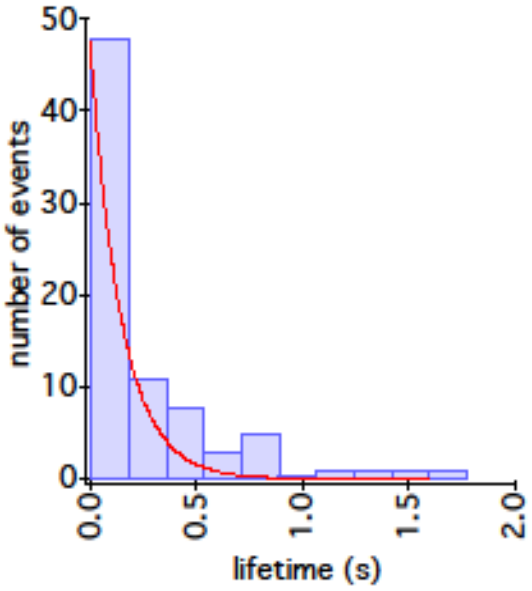

Figure 5.8. Histogram of lifetimes under clamping force from 45 pN to 60 pN using feedback ON method [49] .

The force histograms from eight force groups were analysed to map the off-rate which is the reciprocal of lifetime as a function of clamping force. Figure 5.9 is the natural logarithm of off-rate as a function of force when using feedback ON method. The data was fitted with Bell-Evans' model using equations (1.12) and (1.13) [123] [124] . Two slopes on the figure indicate two energy barriers are present in this molecule pair, which have been consistently observed for biotin-streptavidin bonds [117] . Zero force off-rates in two regions K^0 were derived from the y-intercept of the extended fitted lines, barrier widths x_β were derived from the slops of the fitted line. Table 5.2 shows these parameters with one standard deviation.

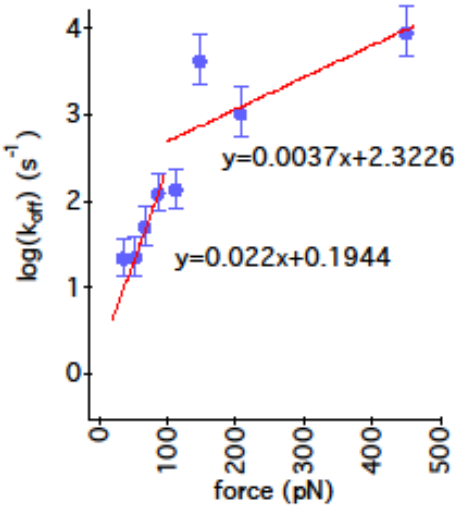

Figure 5.9. The off-rate versus clamping force using controller ON method [49] .

Table 5.2. Zero force off-rates K^0 and barrier widths x_β estimated from data using feedback ON method [49] .

	Force range (pN)	K^0 $(1/s)$	x_β (nm)
Region 1	0-100	1.215 ± 0.128	0.091 ± 0.006
Region 2	100-450	10.202 ± 7.010	0.015 ± 0.011

As discussed in chapter 4, the magnetic field strength and gradient on the magnetic beads at a fixed location depends on the current applied on the electromagnetic actuator, the variance of magnetic force within the vicinity of that location is small. Therefore, when applying constant current, the force on the magnetic beads attached cantilever tip can be considered constant in magnetic actuation system.

Thus force-clamp experiments were also performed with feedback OFF method by applying constant current to the coil. The rupture forces were measured from the sudden decrease of the total force on the cantilever, the lifetimes were measured from the timespan between the moment the total force reached maximum and the rupture.

Figure 5.10 is a sample force curve using feedback OFF method, the molecular bond breaks at $307\ ms$, the rupture force is $102\ pN$, lifetime is $219\ ms$. The constant current applied on the coil is $1.28\ A$ and is on for $2.5\ s$ [49].

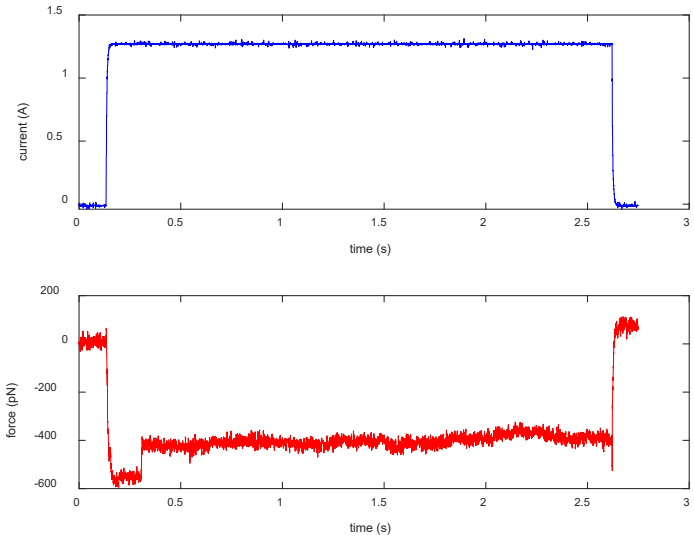

Figure 5.10. A sample force curve from experiments using feedback OFF method [49].

Multiple events in a single force curve were also observed, an example curve with two rupture events at $172\ ms$ and $458\ ms$ is shown in Figure 5.11. The total force on the cantilever reduces whenever a magnetic bead falls off from the cantilever. Since the actuation current remains constant, the remaining beads exert less force on the cantilever, thus the cantilever becomes less bended and moves further away from the actuator. Consequently, the force on each bead also stepwise decreases whenever one of the beads falls down, which means the force of the beads, except for the first one, is underestimated. However, this estimation error depends on the distance between the cantilever tip and the magnetic actuator core tip, which is hard to measure, only the first ruptures were included in the analysis in this research.

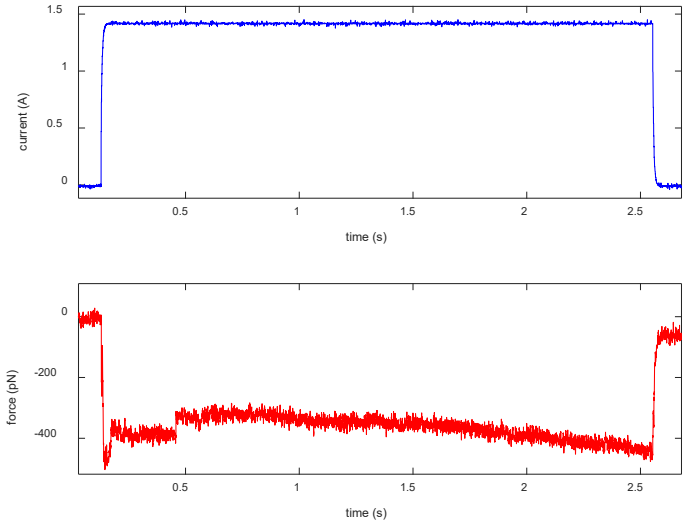

Figure 5.11. A sample force curve with two rupture events from experiments using feedback OFF method.

A total of 481 first rupture events with unbinding forces from $32\,pN$ to $304\,pN$ were recorded. The events were grouped by force levels in the way similar to feedback ON case. Histogram of the lifetime was generated in each group and fitted with exponential probability density function. Figure 5.12 is an example of histogram of lifetime with force from $40\,pN$ to $55\,pN$, the estimated mean value of force is $47\,pN$, the expected lifetime is $0.394\,s$ with 95% confidential interval ($0.316\,s$ $0.507\,s$).

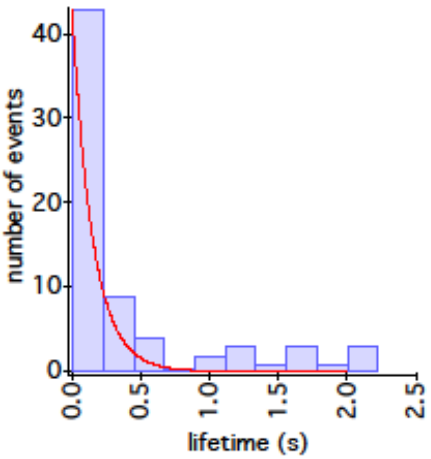

Figure 5.12. Histogram of lifetimes with clamping force from 40 pN to 55 pN using feedback OFF method [49] .

The off-rates and the clamping force were estimated from seven histograms, the natural logarithmic of off-rate versus rupture force is shown in Figure 5.13. Two energy barrier regions were observed similar to the previous case.

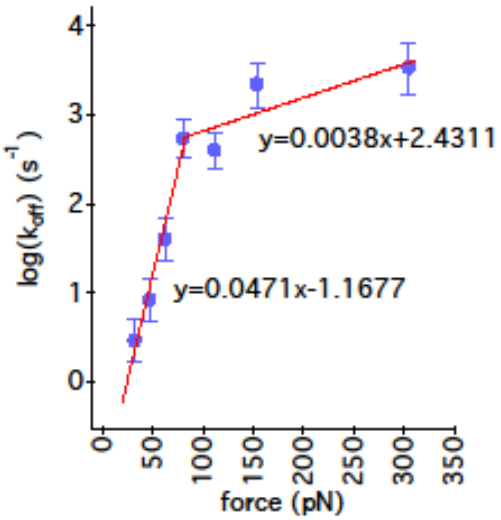

Figure 5.13. The variation of off-rate as a function of clamping force when the feedback controller is turned off [49] .

The zero force off-rate K^0 and barrier width x_β were derived with Bell-Evans' model in the same way as feedback ON case. The numerical values with one standard deviation are shown in Table 5.3.

Table 5.3. Zero force off-rates K^0 and barrier widths x_β derived from feedback OFF method [49] .

	Force range （pN）	K^0 (1/s)	x_β (nm)
Region 1	0-100	0.311±0.093	0.19±0.02
Region 2	100-350	11.373±3.590	0.02±0.01

5.2.3 Discussion

The PID parameters of the feedback controller were optimised empirically before experiments. However, the system dynamics depends more on the characteristics of the hardware of the setup and the alignment of the laser, cantilever and magnetic actuator even if the controller parameters were optimized.

When the feedback is OFF, the moving structure in the system is miniaturised beads while the relatively large cantilever is kept stationary, the system dynamics mainly depend on the characteristics of the electromagnet actuator, Thus, the drift in the system is significantly minimised [49] .

Figure 5.14 compares the data collected from feedback ON and feedback OFF methods. More scattered data for the feedback ON case is shown in Figure 5.14 (a), especially near the $100\ pN$ clamping force region. This may due to the difference of the rise times when using feedback ON method. The rise times are different in feedback ON and feedback OFF cases, the selection of starting time does not significantly affect the estimation of off-rate, but the variations of rise times, thus the pulling speed may induce errors [125] . The different slopes in the feedback ON and OFF curves may due to the discard of subsequent data on the multiple event curves.

Figure 5.14 (b) shows the scatter plot of the off-rate versus clamping force for feedback ON and feedback OFF methods. The scatter distribution of lifetimes in these two methods are very similar, which demonstrates that it is possible to perform force-clamp experiments without using feedback system in the customised AFM system [49] .

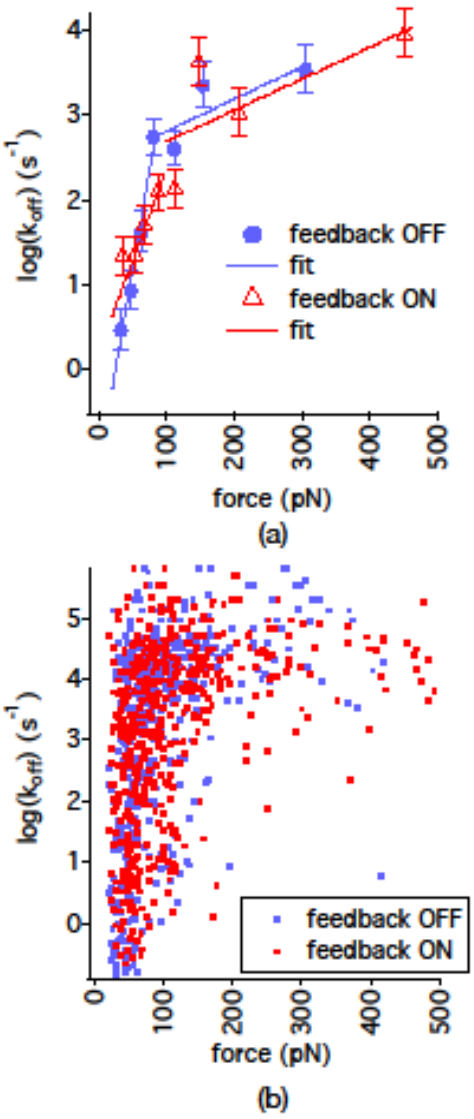

Figure 5.14. The comparison of off-rates using feedback ON and feedback OFF methods. (a) The statistical results and fittings, (b) the scatter plot [49] .

5.3 Heparin-FGF2 Pulling Experiments

Heparin is a type of linear polysaccharides with complex structure, a member of the glycosaminoglycan (GAG) family. It's expressed only in mast cells [126] . It has been used clinically for over 70 years, especially as anticoagulant [127] . Hundreds of proteins have been shown to bind to heparin [128] , despite the long history, the interest in

characterisation of heparin-protein binding continues because of its great potentials in medical applications [129] .

Fibroblast Growth Factors 2 (FGF2), also called basic FGF, is one of the peptides first to be identified, purified from different tissues, it's also one of the most widely studied fibroblast growth factor [130] [131] . FGF2 plays an important role in many physiological and pathological processes, including wound healing process [132] , stem cell differentiation [133] , cell proliferation [134] [135] and angiogenesis [136] . It has great potential in drug development [137] [138] and clinical application such as implantation [139] and recombinant protein therapy [140] [141] .

Study has shown that in culture media, FGF2 is stable at 4℃ but degrades easily at 37℃ [142] , heparin is used to bind FGF2 to stabilise and prolong half-life of FGF2 [143] [144] and regulate the released of FGF2 [145] .

Several regions on FGF2 participating in cell attachment and heparin binding are identified by crystallographic studies combining with site-directed mutagenesis experiments [146] . FGF2 binding structural requirements to heparin are also studied by nuclear magnetic resonance (NMR) spectroscopy [147] . The stable ratios of FGF2 and heparin saccharides of different lengths reveal the mechanisms of heparin promoting FGF2 [148] . The dissociation rate of FGF2 binding to heparan sulfate proteoglycans (HSPG) under flow induced shear stress is also measured experimentally [149] .

However, bulk measurements only measure the average characteristics but not monitor individual molecule behaviours. Here single molecule experiments of heparin-FGF2 were performed using the customised AFM system.

5.3.1 Sample preparation

In conventional piezo pulling experiment, MLCT (Bruker) cantilever was functionalised in $10\,\mu L$ murine FGF2 with concentration of $112.5\,\mu g/mL$ [150] for 15 min, meanwhile the coverslip was incubated in $20\,\mu L$ of low molecular weight heparin (Sanofi-Aventis) with concentration of $20\,\mu g/mL$. The excess heparin was removed by pipette, then both the functionalised cantilever and coverslip were treated with $50\,\mu L$ of BSA (Sigma-Aldrich) with concentration of $40\,\mu g/mL$ for 15 min to reduce nonspecific adhesion. After removing the BSA, $100\,\mu L$ droplet of PBS was placed onto the coverslip and then the cantilever was brought down towards the surface to form a meniscus for the experiment.

In magnetic actuation experiments, the magnetic beads (micromod Partikeltechnologie GmbH) with $5\,\mu m$ diameter were decorated with low molecular weight heparin through surface functionalised PEG-NH2 [151] . The cantilever (MLCT, Bruker) was functionalised with FGF2 with concentration of $112.5\,\mu g/mL$ for 15 min. Then the cantilever and a new coverslip were incubated in BSA with concentration of $40\,\mu g/mL$ for 15 min to reduce nonspecific adhesion. $100\,\mu L$ droplet of PBS was placed onto the centre of the coverslip, then the heparin decorated magnetic beads were injected into the PBS on top of the core tip of the magnetic actuator with a micropipette. Cantilever was aligned with the core tip and brought towards the surface to form a meniscus.

5.3.2 Results

Control experiments were performed to test the validity of the experiment protocol of using heparin decorated beads and FGF2 coated cantilever by examining the binding probabilities. The probability of ruptures from experiment groups and control groups is shown in Figure 5.15. The first control experiment was performed in the in the PBS with

10-times excess of NaCl which impaired electrostatic interactions between the heparin-FGF2 pair, the probability of binding was reduced significantly to 7.04 ± 4.2%. The second control experiment was performed by saturating the FGF2 coated cantilever with heparin, the FGF2 coated cantilever was kept inside heparin solution overnight prior to the experiment, the probability of binding reduced to 1.96 ± 0.31%. The third control experiment was performed using FGF2 coated cantilever and unmodified blank magnetic beads, the probability of nonspecific interaction was 1.53 ± 0.63%. While using heparin decorated beads and FGF2 functionalised cantilever, the probability of binding was measured to be 29.09 ± 3.11%, therefore the bindings were specific. This binding probability also ensured that majority of the recorded events were from single-molecular interactions [152] .

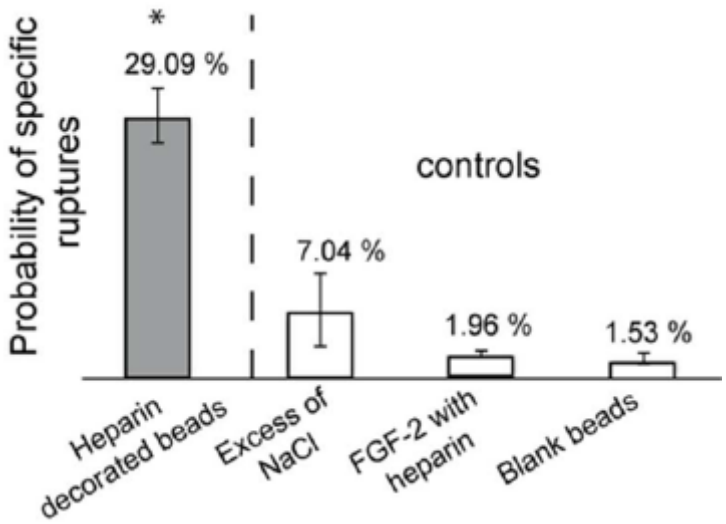

Figure 5.15. Probability of ruptures in experiment group and control groups [152] .

During piezo actuation experiments, the piezo actuators were actuated by triangular waves with different frequencies to induce different loading rates. The loading rates were varied from 1×10^3 to $1 \times 10^7\, pN/s$.

Magnetic actuation was used to perform pulling experiments at the low loading regime from 1×10^1 to $1 \times 10^4\, pN/s$, which is slower than those using conventional piezo actuators. A typical force curve is shown in Figure 5.16, the loading rate is $670\, pN/s$,

the rupture force is 60 pN [152] .

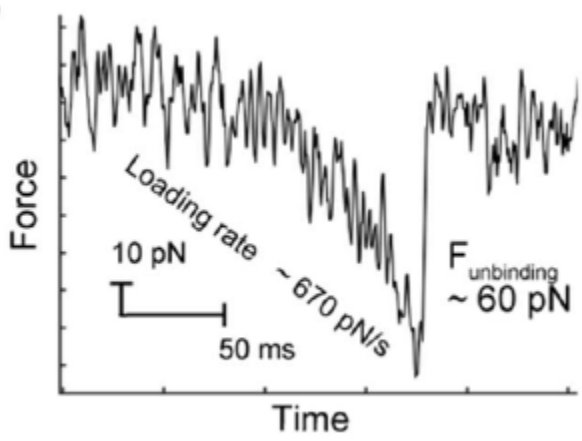

Figure 5.16. Sample force curve from heparin-FGF2 experiments using magnetic actuation [152] .

Conventional pulling experiments were also performed using a commercial AFM. The most probable rupture force in respect to loading rate from the three experiment methods is shown in Figure 5.17. The most probable rupture force measured with magnetic actuation method, which is labelled in black circle, together with the most probable rupture force measured from piezo actuation method using the customised AFM, which is labelled in red star, show good agreement with those measured by the commercial AFM (blue triangle). This indicates that the electromagnetic actuator of the customised AFM is able to perform pulling experiments with low loading rates, which is similar to the physiological conditions and at cellular force levels [152] .

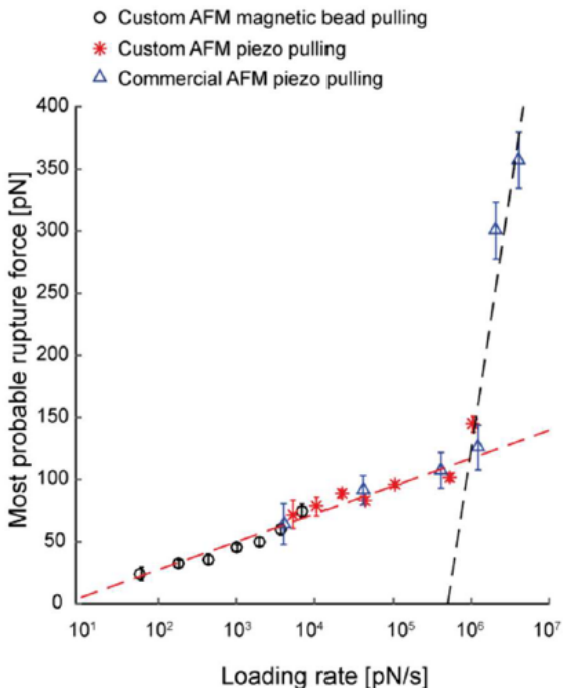

Figure 5.17. Most probable rupture force as a function of loading rate [152] .

The corresponding Bell's parameters K^0 and x_β of the heparin-FGF2 molecule pair were fitted with the same method mentioned earlier in this chapter. The numerical results are summarised in Table 5.4.

Table 5.4. Bell's parameters of heparin-FGF2 interaction at different loading rate regimes [152] .

	Loading rate (pN/s)	K^0 (s^{-1})	x_β (nm)
Region 1	1×10^1 to 1×10^6	0.62	0.42
Region 2	1×10^6 to 1×10^7	2774	0.02

The presence of two distinct linear regions shows that two energy barriers exist along the potential energy coordinate of the heparin-FGF2 bond. The calculated zero force off-rate K^0 from the high loading rate region is about 4500 times higher than the zero force off-rate $K^0 = 0.62\ s^{-1}$ from the low loading region. The K^0 in low loading rate region shows good agreement with a study of heparin-FGF2 interactions using surface plasmon

resonance SPR analysis, which is $K^0 = 0.43 \pm 1.92 \times 10^{-2}\ \mathrm{s}^{-1}$ [153] The unit cell of FGF2 measured by X-ray diffraction is approximately $3.20\ nm \times 4.18\ nm \times 8.59\ nm$ (pdb file: 1BFB [154]). The calculated $x_\beta = 0.42\ nm$ in low loading rate region is consistent to the binding site with heparin [152] .

5.4 Heparin-FGF2 Force Clamp Experiments

5.4.1 Sample preparation

The experimental setup and sample preparation procedure in force clamp experiments was the same as that in pulling experiment using magnetic actuation except that the cantilever was aligned $5\ \mu m$ above the core tip of the magnetic actuator.

5.4.2 Results

Figure 5.18 is a sample force curve using heparin and FGF2 when the feedback controller is on. The setpoint force acting on the cantilever for all the beads is about $1500\ pN$, a rupture event happens at $978\ ms$ with unbinding force measured to be $263\ pN$, due to the sudden change in the total force, the actuation current increases by $0.33\ A$ to bring the total force back to the setpoint. The time of the force applied in the experiment was $1.5\ s$, which was long enough to observe most of the events for this molecular pair.

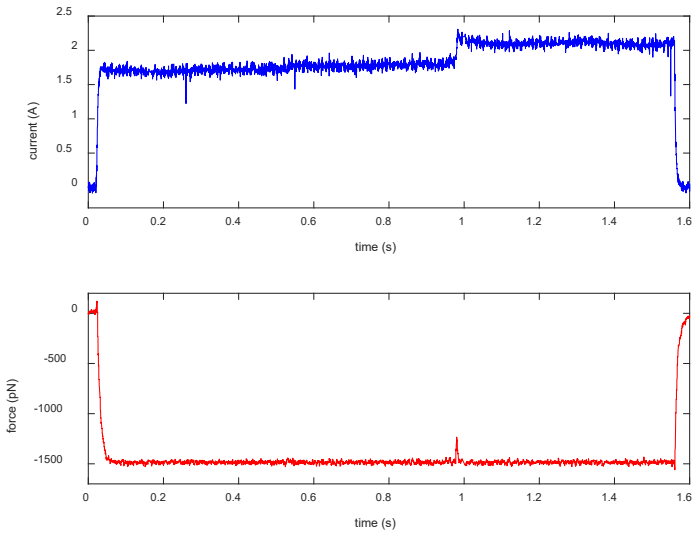

Figure 5.18. A typical force curve from heparin-FGF2 force clamp experiment using feedback ON method.

Same as in biotin-streptavidin force clamp case, only the first rupture events were included in statistical analysis. In total 469 first rupture events were observed, all the subsequence events were discarded. Similarly, the data were grouped by the vicinity of force and then histograms of lifetime were plotted and fitted with exponential distribution. Figure 5.19 is the histogram of lifetime with force from $40\ pN$ to $55\ pN$, the mean force is $47\ pN$ and the expected lifetime is estimated to be $0.26\ s$ with 95% confidential interval $(0.21\ s,\ 0.34\ s)$.

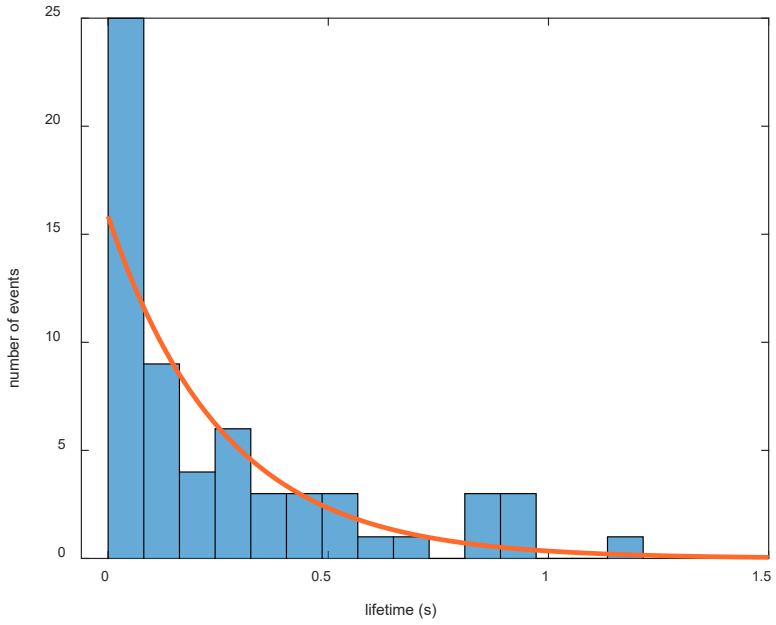

Figure 5.19. Histogram of lifetime with clamping force from 40 pN to 55 pN using feedback ON method from heparin-FGF2 force clamp experiment.

In force clamp without feedback experiment, only DC current was applied on the electromagnetic coil to actuate the force applied on the magnetic beads. Figure 5.20 shows a typical force curve using feedback OFF method. The current is kept constant at 1.1 A for 1.5 s. A rupture happens at 524 ms with unbinding force of 73 pN.

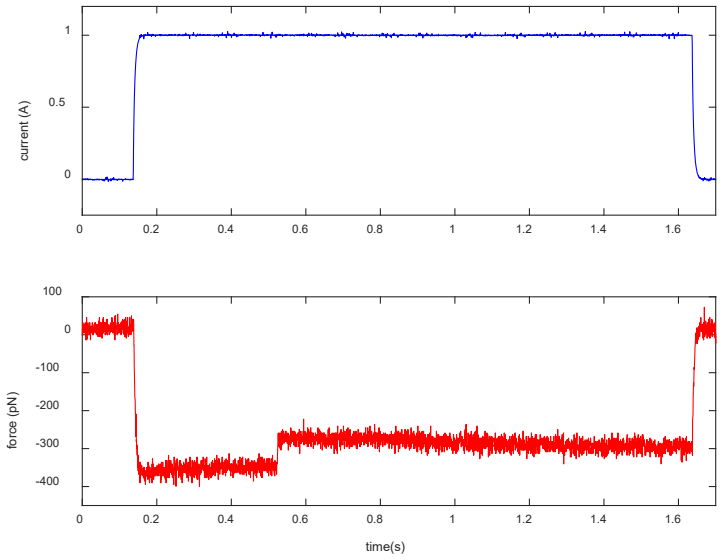

Figure 5.20. Sample force trace captured using feedback OFF method in heparin-FGF2 force clamp experiment.

The data were also processed in the same way as described in feedback ON method. In total 787 first rupture events were collected for statistical analysis, all the subsequence events were discarded. The data then were grouped by force ranges and the lifetimes in each force range were fitted with exponential distribution. Figure 5.21 is the histogram of lifetimes at force ranges from $55\,pN$ to $65\,pN$, the mean force is $60\,pN$ and the expected lifetime is estimated to be $0.27\,s$ with 95% confidential interval ($0.22\,s$, $0.34\,s$).

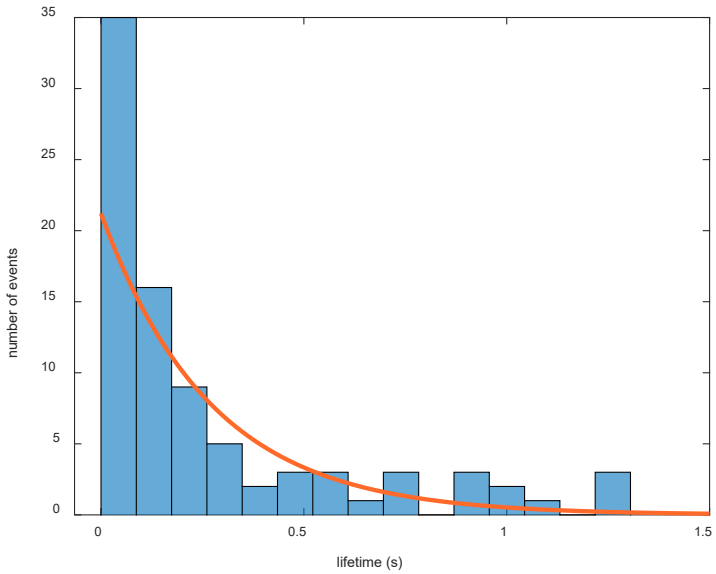

Figure 5.21. Histogram of lifetimes under clamping force ranging from 55 pN to 65 pN using feedback OFF method in heparin-FGF2 force clamp experiment.

The off-rates k_{off} were plot as a function of force to derive K^0 and x_β by fitting Bell-Evan's model, the numerical fitted results are summarised in Table 5.5. Figure 5.22 is the fitted off-rates from both feedback ON and feedback OFF methods as a function of force. Two distinct force regions exhibit in both methods and agree with each other, the two intersections of the slopes at about $110\ pN$, are also consistent with the intersection of two loading rate regions from pulling experiments. which proves that force clamp experiments using both feedback ON and feedback OFF methods are valid.

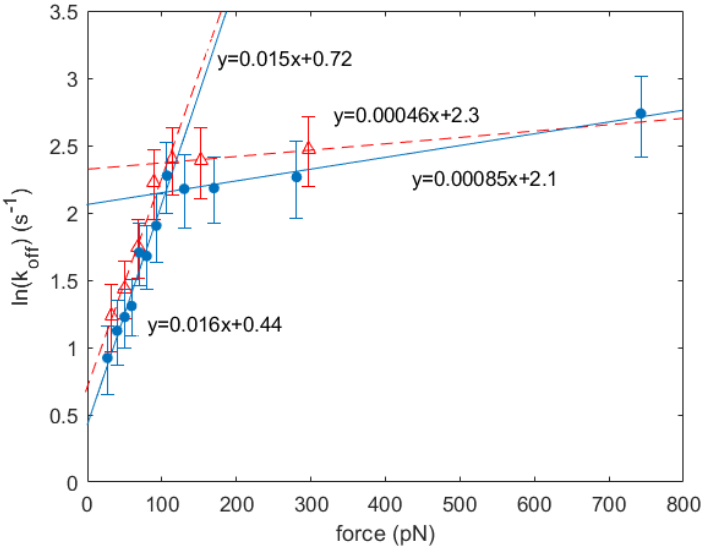

Figure 5.22. Estimated off-rates as a function of clamping force from heparin-FGF2 experiments.

Table 5.5. Bell's parameters estimated from Heparin-FGF2 experiments using force clamp method.

	Feedback ON		Feedback OFF	
	$x_\beta\ (nm)$	$K^0\ (1/s)$	$x_\beta\ (nm)$	$K^0\ (1/s)$
Region 1	0.062	2.05	0.066	1.55
Region 2	0.002	9.97	0.004	8.17

Figure 5.23 is the scatter plot of all the first ruptures using feedback ON and feedback OFF methods. Similar to the biotin-streptavidin experiment case, the off-rates seems to be more scattered and higher at $110\ pN$ region using feedback ON method. However, the distribution of them is close to the feedback OFF case, further verified that it is possible to perform force clamp experiments without feedback controller using the customised AFM.

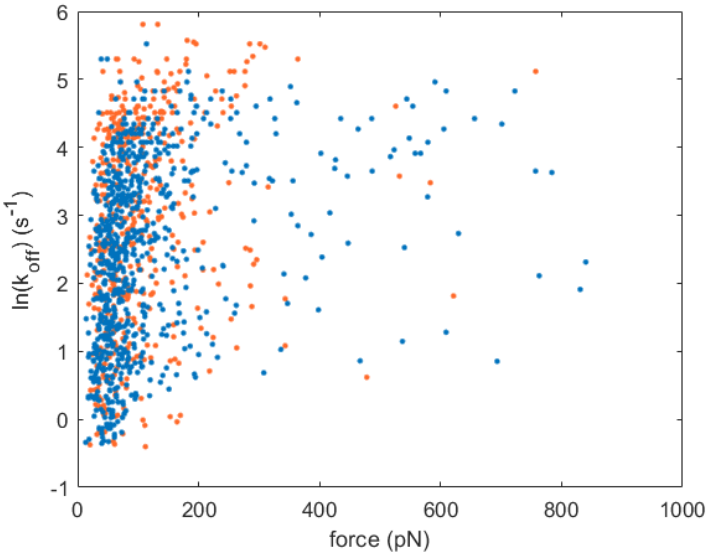

Figure 5.23. Nature logarithmic of off-rate versus clamping force from heparin-FGF2 experiments, data from feedback ON method is in red, from feedback OFF is in blue.

6. CONCLUSIONS

The main achievements in this research are listed in this chapter, the limitations and some possible further developments are also mentioned.

6.1 The Main Achievements in This Study

1) The hardware

The main aim in this research is to develop a customised AFM that is capable of both piezo actuation and magnetic actuation for single molecule experiments. The requirements for the hardware were analysed. The AFM head was first designed in SolidWorks, then was 3D printed with rigid resin and assembled, the electronic components were properly connected, the noise level and force resolution measured from the initial experiments met the requirements for single molecule experiments. The electromagnetic actuator was designed to meet the requirements of working distance and force range, the coil and core were manufactured accordingly with suitable materials and suitable coil drive amplifiers were chosen. The customised AFM was tested experimentally, the outcome electromagnetic actuator integrated sample stage met the requirements of both the force range within the working distance and actuation bandwidth, the heating effect of the coil didn't show significant impact on biomolecular experiments. The positioning of both the AFM head and sample stage were realised by manual micrometre with 3 degree of freedom.

2) The software

The simulation analysis was performed on MATLAB Simulink, the basic characteristics of the system is understood through the simulation. Then a software controller was

designed on LabView (National instrument) for the AFM system. Accordingly, the software was programmed for cantilever deflection signal tracking, cantilever sensitivity calibration, pulling experiments using both piezo and magnetic actuation and force clamp experiment using magnetic actuation. The software was programmed modulated with user-friendly interfaces.

3) Biomolecular pulling experiments

Conventional biomolecular pulling experiments by varying loading rates were performed using the well-studied biotin-streptavidin pair on both the customised AFM and a commercial AFM. The functionalisation protocols for both the piezo and magnetic actuation experiments on the customised AFM were developed. In loading rate region from $10^2\ pN/s$ to $10^5\ pN/s$, the measured zero force dissociation rate K^0 and barrier widths x_β are $6.41 \times 10^{-4}\ s^{-1}$ and $0.85\ nm$ respectively using piezo actuation and $1.08\ s^{-1}$ and $0.28\ nm$ respectively using magnetic actuation, which are comparable to the measurement in commercial AFM, $K^0 = 6.04 \times 10^{-4}\ s^{-1}$ and $x_\beta = 0.48\ nm$. In loading rate region from $10^5\ pN/s$ to $10^6\ pN/s$, the measure K^0 and x_β are $7.14 \times 10^2\ s^{-1}$ and $0.07\ nm$ respectively using piezo actuation in the customised AFM system, they are also comparable to the measurement results $5.25 \times 10^2\ s^{-1}$ and $0.05\ nm$ using commercial AFM and comparable to other literatures [117] . Then pulling experiments using heparin-FGF2 were also performed, the slip bond properties and the presence of two distinct energy barriers of this pair were revealed. In loading rate region until 1×10^6 pN/s, the calculated dissociation rate $K^0 = 0.62\ s^{-1}$ shows good agreement with the result $K^0 = 0.43 \pm 1.92 \times 10^{-2}\ \mathrm{s}^{-1}$ using surface plasmon resonance SPR analysis [153] , barrier widths $x_\beta = 0.42\ nm$ is consistent to the X-ray diffraction measurement of unit cell of FGF2, which is $3.20\ nm \times 4.18\ nm \times 8.59\ nm$ (pdb file: 1BFB [154]).

4) Biomolecular force clamp experiments

Following the protocols to functionalise biomolecular on magnetic beads and AFM cantilevers, force clamp experiments were also performed using two different pairs of molecules and the off-rates and barrier widths which indicate the affinities and dynamics of these two pairs were measured, two distinct energy barriers were revealed from both pairs, the boundary of the barriers are consistent with the measurements with the customised AFM and the commercial AFM using varying loading rate methods.

5) Specifications

Some important specifications of the customised AFM are listed in Table 6.1. The AFM meets the requirements for biomolecular force measurement.

Table 6.1 Specifications of the customised AFM

Specification	Definition and Dependence	Value
Working Distance	Traveling range of the piezo actuator	15 μm
Resolution	Vertical displacement resolution of the piezo actuator	0.15 nm
Resonance Frequency (Piezo)	resonance frequency of the piezo actuator.	18 kHz
Response Time (Piezo)	Step response time when using piezo actuation,	~1 μs
Response Time (Magnetic)	Step response time when using magnetic actuation,	~10 ms
Force Resolution (Air)	Force resolution obtained by noise spectrum analysis in air using SNL-10 cantilever	2 pN
Force Resolution (DI Water)	Force resolution obtained by noise spectrum analysis in DI water using SNL-10 cantilever	3 pN
Measurement Bandwidth	Maximum measurement bandwidth limited by photodetector	250 kHz
Actuation Bandwidth	Open loop actuation bandwidth when using magnetic actuator	1 kHz
Maximum Force	Force on Dynabeads M-280 bead at 5 μm away from core tip	1000 pN

6.2 Main Features of the Developed System

1) The structural parts of the customised AFM are 3D printed, so that with the designed, they can be readily re-printed, the electronic components are also commercially available and comparatively inexpensive, which means the customised AFM can be built readily at low cost following the design.

2) The AFM take advantages of the high spatial resolution of optical lever measurement and the almost infinite actuation bandwidth of magnetic actuation. Since magnetic beads are used in magnetic actuation mode, the actuator size is shrunk down to a few micrometres and the experiment using beads as actuators is performed in a non-contact mode, therefore the system is robust against noise. The maximum actuation force about $1000\,pN$ using magnetic actuation can be achieved when the magnetic bead (Dynabead M-280) is about $5\,\mu m$ away from the core tip of the actuator. Statistical results from bio-experiments using two different molecule pairs also show that it's capable of fore clamp experiment without the need for an active feedback controller.

3) The AFM is in a compact design, the piezo actuation integrated head and magnetic actuation integrated sample stage are detachable, the whole system is lightweight and portable desktop size. It's both flexible and multifunctional.

4) The LabView based software controller is designed in a modulated way with friendly user interface, it can perform experiments and collect data automatically, which increases the efficiency and data throughput.

5) It provides a novel way to perform single molecular force clamp experiments. The experiment results allow the extraction of the affinities and dynamics of the molecular pair, which is important to understand the nature of molecule bonds.

6.3 Limitations and Possible Further Developments

1) Since camera is not integrated in the system, the working range of the piezo is $15\ \mu m$, the laser alignments rely on the observation of optical path and the manual adjustment of the linear stages, therefore the AFM system highly relies on the experience of the user. Further possible improvement can be integrating a suitable camera into the 3D printed AFM head, there's enough spare space on the AFM head and a new AFM head can be printed readily. The system can also be upgraded with motorised stage, thereby extra functionalities for stage control can be added into the software controller in further developments. However, the cost will also increase.

2) The 3D printed components will deform after about 2 years of usage based on our experience, a new AFM need to be re-printed and assembled, due to manufacturing precision limitation, the new AFM head is not identical with the previous one, consequently the optical path will change. It's possible that the optical lever magnification of the new printed AFM differs from the previous one. The possible solution can be using magnetic compactable aluminium alloy to manufacture AFM head material with higher precision computer numerical control (CNC) machining.

3) The system is operated in open environment, so it can pick up all the environmental noise, such as wind motion, ground vibration and sounds. It's necessary to build an enclosure and prepare a vibration platform for it for noise isolation. In further development, the enclosure can be standardised to facilitate compatibility and repeatability.

4) The actual sampling rate of the system is lower than the DAQ card maximum capability, although the timer utilised in the software is the build-in timer on the DAQ card, the open loop actuation rate can reach about $4\ kHz$, however because the software controller is built on a PC which is not a real time system, some sampling

points may be missing due to the competing of CPU time, this is much lower than the capability of the DAQ card. To increase the sampling rate of the system while using close loop actuation, the possible solutions can be upgrading the PC or using a real time system in the sacrifice of the user friendliness but achieve more significant speed improvement.

5) Only the first rupture events in force clamp experiments were included during statistical analysis, which means the lifetimes of the bonds in the analysis tend to be shorter due to selection bias. The statistical analysis method can be improved by developing a new mathematical model to use the subsequence rupture events.

REFERENCE

[1] Thomas Jr G J. Raman spectroscopy of protein and nucleic acid assemblies[J]. Annual review of biophysics and biomolecular structure, 1999, 28(1): 1-27.

[2] Bonham A J, Braun G, Pavel I, et al. Detection of sequence-specific protein-DNA interactions via surface enhanced resonance Raman scattering[J]. Journal of the American Chemical Society, 2007, 129(47): 14572-14573.

[3] Banerjee A, Perez-Castillejos R, Hahn D, et al. Micro-fluidic channels on nanopatterned substrates: Monitoring protein binding to lipid bilayers with surface-enhanced Raman spectroscopy[J]. Chemical physics letters, 2010, 489(1-3): 121-126.

[4] Oladepo S A, Xiong K, Hong Z, et al. Elucidating peptide and protein structure and dynamics: UV resonance Raman spectroscopy[J]. The journal of physical chemistry letters, 2011, 2(4): 334-344.

[5] Dykeman E C, Sankey O F. Atomistic modeling of the low-frequency mechanical modes and Raman spectra of icosahedral virus capsids[J]. Physical Review E, 2010, 81(2): 021918.

[6] Shanmukh S, Jones L, Zhao Y P, et al. Identification and classification of respiratory syncytial virus (RSV) strains by surface-enhanced Raman spectroscopy and multivariate statistical techniques[J]. Analytical and bioanalytical chemistry, 2008, 390(6): 1551-1555.

[7] Short K W, Carpenter S, Freyer J P, et al. Raman spectroscopy detects biochemical changes due to proliferation in mammalian cell cultures[J]. Biophysical journal, 2005, 88(6): 4274-4288.

[8] Chapman H N, Fromme P, Barty A, et al. Femtosecond X-ray protein nanocrystallography[J]. Nature, 2011, 470(7332): 73-77.

[9] Van den Berg B, Clemons W M, Collinson I, et al. X-ray structure of a protein-

conducting channel[J]. Nature, 2004, 427(6969): 36-44.

[10] Schotte F, Lim M, Jackson T A, et al. Watching a protein as it functions with 150-ps time-resolved x-ray crystallography[J]. Science, 2003, 300(5627): 1944-1947.

[11] Domon B, Aebersold R. Mass spectrometry and protein analysis[J]. science, 2006, 312(5771): 212-217.

[12] Hunt D F, Yates J R, Shabanowitz J, et al. Protein sequencing by tandem mass spectrometry[J]. Proceedings of the National Academy of Sciences, 1986, 83(17): 6233-6237.

[13] Sampath R, Russell K L, Massire C, et al. Global surveillance of emerging Influenza virus genotypes by mass spectrometry[J]. PLoS One, 2007, 2(5).

[14] Snijder J, Rose R J, Veesler D, et al. Studying 18 MDa virus assemblies with native mass spectrometry[J]. Angewandte Chemie International Edition, 2013, 52(14): 4020-4023.

[15] Chait B T, Kent S B. Weighing naked proteins: practical, high-accuracy mass measurement of peptides and proteins[J]. Science, 1992, 257(5078): 1885-1894.

[16] Katta V, Chait B T, Carr S. Conformational changes in proteins probed by hydrogen‐exchange electrospray‐ionization mass spectrometry[J]. Rapid Communications in Mass Spectrometry, 1991, 5(4): 214-217.

[17] Pierce M M, Raman C S, Nall B T. Isothermal titration calorimetry of protein–protein interactions[J]. Methods, 1999, 19(2): 213-221.

[18] Bou-Abdallah F, Arosio P, Levi S, et al. Defining metal ion inhibitor interactions with recombinant human H-and L-chain ferritins and site-directed variants: an isothermal titration calorimetry study[J]. JBIC Journal of Biological Inorganic Chemistry, 2003, 8(4): 489-497.

[19] Swamy M J, Sankhala R S, Singh B P. Thermodynamic Analysis of Protein–

Lipid Interactions by Isothermal Titration Calorimetry[M]//Lipid-Protein Interactions. Humana, New York, NY, 2019: 71-89.

[20] Velazquez-Campoy A, Freire E. Isothermal titration calorimetry to determine association constants for high-affinity ligands[J]. Nature protocols, 2006, 1(1): 186-191.

[21] Luo Q, Chen D, Boom R M, et al. Revisiting the enzymatic kinetics of pepsin using isothermal titration calorimetry[J]. Food chemistry, 2018, 268: 94-100.

[22] Rodler A, Beyer B, Ueberbacher R, et al. Hydrophobic interaction chromatography of proteins: Studies of unfolding upon adsorption by isothermal titration calorimetry[J]. Journal of separation science, 2018, 41(15): 3069-3080.

[23] Zlatanova J, Van Holde K. Single-molecule biology: what is it and how does it work?[J]. *Molecular cell*, 2006, 24(3): 317-329.

[24] Neher E, Sakmann B. Single-channel currents recorded from membrane of denervated frog muscle fibres[J]. *Nature*, 1976, 260(5554): 799.

[25] Stuart G J, Dodt H U, Sakmann B. Patch-clamp recordings from the soma and dendrites of neurons in brain slices using infrared video microscopy[J]. *Pflügers Archiv*, 1993, 423(5-6): 511-518.

[26] Scheel O, Frech S, Amuzescu B, et al. Action potential characterization of human induced pluripotent stem cell–derived cardiomyocytes using automated patch-clamp technology[J]. *Assay and drug development technologies*, 2014, 12(8): 457-469.

[27] Singer J J, Walsh V. Characterization of calcium-activated potassium channels in single smooth muscle cells using the patch-clamp technique[J]. *Pflügers Archiv*, 1987, 408(2): 98-111.

[28] Göpel S O, Kanno T, Barg S, et al. Patch-clamp characterisation of somatostatin-secreting δ-cells in intact mouse pancreatic islets[J]. *The Journal*

of physiology, 2000, 528(3): 497-507.

[29] Delcour A H, Martinac B, Adler J, et al. Modified reconstitution method used in patch-clamp studies of Escherichia coli ion channels[J]. *Biophysical journal*, 1989, 56(3): 631-636.

[30] Spring KR, Davidson MW. "Introduction to Fluorescence Microscopy". *Nikon MicroscopyU*. Retrieved 28 September 2008.

[31] Möckl L, Lamb D C, Bräuchle C. Super-resolved Fluorescence Microscopy: Nobel Prize in Chemistry 2014 for Eric Betzig, Stefan Hell, and William E. Moerner[J]. *Angewandte Chemie International Edition*, 2014, 53(51): 13972-13977.

[32] Sahl S J, Moerner W E. Super-resolution fluorescence imaging with single molecules[J]. *Current opinion in structural biology*, 2013, 23(5): 778-787.

[33] Kronick M N, Little W A. Fluorescent immunoassay employing total reflection for activation: U.S. Patent 3,939,350[P]. 1976-2-17.

[34] Axelrod D. Cell-substrate contacts illuminated by total internal reflection fluorescence[J]. *The Journal of cell biology*, 1981, 89(1): 141-145.

[35] Funatsu T, Harada Y, Tokunaga M, et al. Imaging of single fluorescent molecules and individual ATP turnovers by single myosin molecules in aqueous solution[J]. *Nature*, 1995, 374(6522): 555.

[36] Boehm E M, Subramanyam S, Ghoneim M, et al. Quantifying the assembly of multicomponent molecular machines by single-molecule total internal reflection fluorescence microscopy[M]//*Methods in enzymology. Academic Press*, 2016, 581: 105-145.

[37] Shimomura O, Johnson F H, Saiga Y. Extraction, purification and properties of aequorin, a bioluminescent protein from the luminous hydromedusan, Aequorea[J]. *Journal of cellular and comparative physiology*, 1962, 59(3): 223-239.

[38] Chalfie M, Tu Y, Euskirchen G, et al. Green fluorescent protein as a marker for gene expression[J]. Science, 1994, 263(5148): 802-805.

[39] Tsien R Y. *The green fluorescent protein*[J]. 1998.

[40] Zacharias D A, Tsien R Y. Molecular biology and mutation of green fluorescent protein[J]. *Methods of biochemical analysis*, 2006, 47: 83-120.

[41] Liang F, Guo Y, Hou S, et al. Photonic-plasmonic hybrid single-molecule nanosensor measures the effect of fluorescent labels on DNA-protein dynamics[J]. *Science advances*, 2017, 3(5): e1602991.

[42] Tinoco Jr I, Bustamante C. The effect of force on thermodynamics and kinetics of single molecule reactions[J]. *Biophysical chemistry*, 2002, 101: 513-533.

[43] Laidler K J. The development of the Arrhenius equation[J]. *Journal of Chemical Education*, 1984, 61(6): 494.

[44] Evans M G, Polanyi M. Some applications of the transition state method to the calculation of reaction velocities, especially in solution[J]. *Transactions of the Faraday Society*, 1935, 31: 875-894.

[45] Evans E. Probing the relation between force—lifetime—and chemistry in single molecular bonds[J]. *Annual review of biophysics and biomolecular structure*, 2001, 30(1): 105-128.

[46] Friedsam C, Wehle A K, Kühner F, et al. Dynamic single-molecule force spectroscopy: bond rupture analysis with variable spacer length[J]. *Journal of Physics: Condensed Matter*, 2003, 15(18): S1709.

[47] Popa I, Kosuri P, Alegre-Cebollada J, et al. Force dependency of biochemical reactions measured by single-molecule force-clamp spectroscopy[J]. *Nature protocols*, 2013, 8(7): 1261.

[48] Neumann J. Physical applications of the ergodic hypothesis[J]. *Proceedings of the National Academy of Sciences of the United States of America*, 1932, 18(3):

263.

[49] Feng L, Torun H. Miniaturized magnetic bead-actuators for force-clamp spectroscopy-based single-molecule measurements[J]. *Ultramicroscopy*, 2020, 209: 112888.

[50] Ashkin A, Dziedzic J M, Bjorkholm J E, et al. Observation of a single-beam gradient force optical trap for dielectric particles[J]. *Optics letters*, 1986, 11(5): 288-290.

[51] Grier D G. A revolution in optical manipulation[J]. *Nature*, 2003, 424(6950): 810.

[52] Neuman K C, Block S M. Optical trapping[J]. *Review of scientific instruments*, 2004, 75(9): 2787-2809.

[53] Gordon R. Biosensing with nanoaperture optical tweezers[J]. *Optics & Laser Technology*, 2019, 109: 328-335.

[54] Bolognesi G, Friddin M S, Salehi-Reyhani A, et al. Sculpting and fusing biomimetic vesicle networks using optical tweezers[J]. *Nature communications*, 2018, 9(1): 1882.

[55] Hou X, DeSantis M C, Tian C, et al. Optical manipulation of a single human virus for study of viral-cell interactions[C]//Optical Trapping and Optical Micromanipulation XIII. International Society for Optics and Photonics, 2016, 9922: 992212.

[56] Keloth A, Anderson O, Risbridger D, et al. Single Cell Isolation Using Optical Tweezers[J]. *Micromachines*, 2018, 9(9): 434.

[57] Kotnala A, Gordon R. Double nanohole optical tweezers visualize protein p53 suppressing unzipping of single DNA-hairpins[J]. *Biomedical optics express*, 2014, 5(6): 1886-1894.

[58] Miller J, Hester B. Determination of Elastic Modulus of White Blood Cells with

Varying Temperatures using Optical Tweezers[J]. *Biophysical Journal*, 2019, 116(3): 431a.

[59] Curtis J E, Koss B A, Grier D G. Dynamic holographic optical tweezers[J]. *Optics communications*, 2002, 207(1-6): 169-175.

[60] Crick F H C, Hughes A F W. The physical properties of cytoplasm[J]. *Experimental Cell Research*, 1950, 1(1): 37-80.

[61] Neuman K C, Nagy A. Single-molecule force spectroscopy: optical tweezers, magnetic tweezers and atomic force microscopy[J]. *Nature methods*, 2008, 5(6): 491.

[62] Strick T R, Allemand J F, Bensimon D, et al. The elasticity of a single supercoiled DNA molecule[J]. *Science*, 1996, 271(5257): 1835-1837.

[63] Lipfert J, Kerssemakers J W J, Jager T, et al. Magnetic torque tweezers: measuring torsional stiffness in DNA and RecA-DNA filaments[J]. *Nature methods*, 2010, 7(12): 977..

[64] Crut A, Koster D A, Seidel R, et al. Fast dynamics of supercoiled DNA revealed by single-molecule experiments[J]. *Proceedings of the National Academy of Sciences*, 2007, 104(29): 11957-11962.

[65] Shang H, Lee G U. Magnetic Tweezers Measurement of the Bond Lifetime− Force Behavior of the IgG− Protein A Specific Molecular Interaction[J]. *Journal of the American Chemical Society*, 2007, 129(20): 6640-6646.

[66] Lansdorp B M, Tabrizi S J, Dittmore A, et al. A high-speed magnetic tweezer beyond 10,000 frames per second[J]. *Review of Scientific Instruments*, 2013, 84(4): 044301.

[67] Binnig G, Quate C F, Gerber C. Atomic force microscope[J]. *Physical review letters*, 1986, 56(9): 930.

[68] Binnig G, Rohrer H. Scanning tunneling microscopy[J]. *Surface science*, 1983,

126(1-3): 236-244.

[69] Herrmann A, Sieben C. Single-virus force spectroscopy unravels molecular details of virus infection[J]. *Integrative Biology*, 2015, 7(6): 620-632.

[70] Jin S, Shi Q, Li Q, et al. Effect of calcium ionic concentrations on the adsorption of carboxymethyl cellulose onto talc surface: Flotation, adsorption and AFM imaging study[J]. *Powder Technology*, 2018, 331: 155-161.

[71] Seifert J, Rheinlaender J, Novak P, et al. Comparison of atomic force microscopy and scanning ion conductance microscopy for live cell imaging[J]. *Langmuir*, 2015, 31(24): 6807-6813.

[72] Essmann C L, Elmi M, Shaw M, et al. In-vivo high resolution AFM topographic imaging of Caenorhabditis elegans reveals previously unreported surface structures of cuticle mutants[J]. *Nanomedicine: Nanotechnology, Biology and Medicine*, 2017, 13(1): 183-189.

[73] Kodera N, Yamamoto D, Ishikawa R, et al. Video imaging of walking myosin V by high-speed atomic force microscopy[J]. *Nature*, 2010, 468(7320): 72.

[74] Ando T, Uchihashi T, Fukuma T. High-speed atomic force microscopy for nano-visualization of dynamic biomolecular processes[J]. *Progress in Surface Science*, 2008, 83(7-9): 337-437.

[75] Hayashi K, Iwata M. Stiffness of cancer cells measured with an AFM indentation method[J]. *Journal of the mechanical behavior of biomedical materials*, 2015, 49: 105-111.

[76] Khan S H, Kramkowski E L, Ochs P J, et al. Viscosity of a nanoconfined liquid during compression[J]. *Applied Physics Letters*, 2014, 104(2): 023110.

[77] Li H, Zhang W, Zhang X, et al. Single molecule force spectroscopy on poly (vinyl alcohol) by atomic force microscopy[J]. *Macromolecular rapid communications*, 1998, 19(12): 609-611.

[78] Zhu X, Siamantouras E, Liu K K, et al. Determination of work of adhesion of biological cell under AFM bead indentation[J]. *Journal of the mechanical behavior of biomedical materials*, 2016, 56: 77-86.

[79] Frybort S, Obersriebnig M, Müller U, et al. Variability in surface polarity of wood by means of AFM adhesion force mapping[J]. *Colloids and Surfaces A: Physicochemical and Engineering Aspects*, 2014, 457: 82-87.

[80] Pyrgiotakis G, Blattmann C O, Demokritou P. Real-time nanoparticle–cell interactions in physiological media by atomic force microscopy[J]. *ACS sustainable chemistry & engineering*, 2014, 2(7): 1681-1690.

[81] Manibog K, Li H, Rakshit S, et al. Resolving the molecular mechanism of cadherin catch bond formation[J]. *Nature communications*, 2014, 5: 3941.

[82] Fernandez J M, Li H. Force-clamp spectroscopy monitors the folding trajectory of a single protein[J]. *Science*, 2004, 303(5664): 1674-1678.

[83] Pacific Silicon Sensor, http://www.mouser.com/catalog/specsheets/qp50-6-18u-sd2-501102[1].pdf

[84] Fukuma T. Wideband low-noise optical beam deflection sensor with photothermal excitation for liquid-environment atomic force microscopy[J]. *Review of Scientific Instruments*, 2009, 80(2): 023707.

[85] Belikov S, Alexander J, Wall C, et al. Thermal tune method for AFM oscillatory resonant imaging in air and liquid[C]//2014 American Control Conference. IEEE, 2014: 1009-1014.

[86] Levy R, Maaloum M. Measuring the spring constant of atomic force microscope cantilevers: thermal fluctuations and other methods[J]. *Nanotechnology*, 2001, 13(1): 33.

[87] Gates R S, Reitsma M G. Precise atomic force microscope cantilever spring constant calibration using a reference cantilever array[J]. *Review of Scientific Instruments*, 2007, 78(8): 086101.

[88] Katzir S. The discovery of the piezoelectric effect[M]//THE BEGINNINGS OF PIEZOELECTRICITY. *Springer, Dordrecht*, 2006: 15-64.

[89] Goldfarb M, Celanovic N. Modeling piezoelectric stack actuators for control of micromanipulation[J]. *IEEE Control Systems Magazine*, 1997, 17(3): 69-79.

[90] Mokaberi B, Requicha A A G. Compensation of scanner creep and hysteresis for AFM nanomanipulation[J]. *IEEE Transactions on Automation Science and Engineering*, 2008, 5(2): 197-206.

[91] Bruker. https://www.brukerafmprobes.com/a-3811-decafmch-pft.aspx

[92] Newport. https://www.newport.com/p/SN100C-F3K

[93] ThorLab. https://www.thorlabs.com/thorproduct.cfm?partnumber=T12XY/M

[94] Florin E L, Pralle A, Stelzer E H K, et al. Photonic force microscope calibration by thermal noise analysis[J]. *Applied Physics A*, 1998, 66(1): S75-S78.

[95] Belikov S, Alexander J, Wall C, et al. Thermal tune method for AFM oscillatory resonant imaging in air and liquid[C]//2014 American Control Conference. IEEE, 2014: 1009-1014.

[96] Sevim S, Shamsudhin N, Ozer S, et al. An Atomic Force Microscope with Dual Actuation Capability for Biomolecular Experiments[J]. *Scientific reports*, 2016, 6: 27567.

[97] De Vlaminck I, Dekker C. Recent advances in magnetic tweezers[J]. *Annual review of biophysics*, 2012, 41: 453-472.

[98] Barbic M, Mock J J, Gray A P, et al. Scanning probe electromagnetic tweezers[J]. *Applied Physics Letters*, 2001, 79(12): 1897-1899.

[99] Lipfert J, Hao X, Dekker N H. Quantitative modeling and optimization of magnetic tweezers[J]. *Biophysical journal*, 2009, 96(12): 5040-5049.

[100] Neuman K C, Nagy A. Single-molecule force spectroscopy: optical tweezers, magnetic tweezers and atomic force microscopy[J]. *Nature methods*, 2008, 5(6):

491.

[101] Lipfert J, Hao X, Dekker N H. Quantitative modeling and optimization of magnetic tweezers[J]. *Biophysical journal*, 2009, 96(12): 5040-5049.

[102] Boyer T H. The force on a magnetic dipole[J]. *American Journal of Physics*, 1988, 56(8): 688-692.

[103] Ostrofet E, Papini F S, Dulin D. Correction-free force calibration for magnetic tweezers experiments[J]. *Scientific reports*, 2018, 8(1): 1-10.

[104] Wong W P, Halvorsen K. The effect of integration time on fluctuation measurements: calibrating an optical trap in the presence of motion blur[J]. *Optics express*, 2006, 14(25): 12517-12531.

[105] Gosse C, Croquette V. Magnetic tweezers: micromanipulation and force measurement at the molecular level[J]. *Biophysical journal*, 2002, 82(6): 3314-3329.

[106] Fonnum G, Johansson C, Molteberg A, et al. Characterisation of Dynabeads® by magnetization measurements and Mössbauer spectroscopy[J]. *Journal of magnetism and magnetic materials*, 2005, 293(1): 41-47.

[107] Tran Q H, Dong-Young K, Parvatheeswara R B, et al. Novel Planar Hall Sensor for Biomedical Diagnosing [J] *Lab-on-a-chip*. 2013. 10.5772/52820.

[108] Bijamov A, Shubitidze F, Oliver P M, et al. Quantitative modeling of forces in electromagnetic tweezers[J]. *Journal of applied physics*, 2010, 108(10): 104701.

[109] Sevim S, Ozer S, Feng L, et al. Dually actuated atomic force microscope with miniaturized magnetic bead-actuators for single-molecule force measurements[J]. *Nanoscale Horizons*, 2016, 1(6): 488-495.

[110] Bahrami M R, Abeygunawardana A W B. Modeling and Simulation of Tapping Mode Atomic Force Microscope Through a Bond-Graph[M]//*Advances in*

Mechanical Engineering. Springer, Cham, 2018: 9-15.

[111] Crut A, Koster D A, Seidel R, et al. Fast dynamics of supercoiled DNA revealed by single-molecule experiments[J]. *Proceedings of the National Academy of Sciences*, 2007, 104(29): 11957-11962.

[112] Bevan M A, Prieve D C. Hindered diffusion of colloidal particles very near to a wall: Revisited[J]. *The Journal of Chemical Physics*, 2000, 113(3): 1228-1236.

[113] Fu H, Jiang Y, Yang D, et al. Flow-induced elongation of von Willebrand factor precedes tension-dependent activation[J]. *Nature communications*, 2017, 8(1): 1-12.

[114] Elangovan M, Wallrabe H, Chen Y, et al. Characterization of one-and two-photon excitation fluorescence resonance energy transfer microscopy[J]. *Methods*, 2003, 29(1): 58-73.

[115] Bennett, S., A history of control engineering, 1930–1955, Peter Peregrinus Ltd., London, UK, 1993.

[116] Åström, K. J., and T. Hägglund, Advanced PID Control, ISA - The Instrumentation, Systems, and Automation Society; Research Triangle Park, NC, USA, 2006.

[117] Teulon J M, Delcuze Y, Odorico M, et al. Single and multiple bonds in (strept) avidin–biotin interactions[J]. *Journal of Molecular Recognition*, 2011, 24(3): 490-502.

[118] Chivers C E, Koner A L, Lowe E D, et al. How the biotin–streptavidin interaction was made even stronger: investigation via crystallography and a chimaeric tetramer[J]. *Biochemical Journal*, 2011, 435(1): 55-63.

[119] Micic M, Chen A, Leblanc R M, et al. Scanning electron microscopy studies of protein-functionalized atomic force microscopy cantilever tips[J]. *Scanning*, 1999, 21(6): 394-397.

[120] Evans E, Ritchie K. Dynamic strength of molecular adhesion bonds[J]. *Biophysical journal*, 1997, 72(4): 1541-1555.

[121] de Odrowąż Piramowicz M, Czuba P, Targosz M, et al. Dynamic force measurements of avidin–biotin and streptavdin–biotin interactions using AFM[J]. *Acta Biochimica Polonica*, 2006, 53(1): 93-100.

[122] Popa I, Kosuri P, Alegre-Cebollada J, et al. Force dependency of biochemical reactions measured by single-molecule force-clamp spectroscopy[J]. *Nature protocols*, 2013, 8(7): 1261. https://doi.org/10.1038/nprot.2013.05

[123] Bell G I. Models for the specific adhesion of cells to cells[J]. *Science*, 1978, 200(4342): 618-627.

[124] Merkel R, Nassoy P, Leung A, et al. Energy landscapes of receptor–ligand bonds explored with dynamic force spectroscopy[J]. *Nature*, 1999, 397(6714): 50-53.

[125] Cao Y, Li H. Single-molecule force-clamp spectroscopy: dwell time analysis and practical considerations[J]. *Langmuir*, 2010, 27(4): 1440-1447. https://doi.org/10.1021/la104130n

[126] Rabenstein D L. Heparin and heparan sulfate: structure and function[J]. *Natural product reports*, 2002, 19(3): 312-331.

[127] Lane D A, Ulf L. Heparin: chemical and biological properties, clinical applications[M]. 1989.

[128] Conrad H E. Heparin-binding proteins[M]. Elsevier, 1997.

[129] Ishihara J, Ishihara A, Fukunaga K, et al. Laminin heparin-binding peptides bind to several growth factors and enhance diabetic wound healing[J]. *Nature communications*, 2018, 9(1): 2163.

[130] Manetti F, Corelli F, Botta M. Fibroblast growth factors and their inhibitors[J]. *Current pharmaceutical design*, 2000, 6(18): 1897-1924.

[131] Gospodarowicz D, Lindstrom J, Rudland P, et al. Fibroblast Growth Factor: Its Localisation, Purification, Mode of Action, and Physiological Significance[M]//*Advances in metabolic disorders*. Elsevier, 1975, 8: 301-335.

[132] Werner S, Grose R. Regulation of wound healing by growth factors and cytokines[J]. *Physiological reviews*, 2003, 83(3): 835-870.

[133] Yu P, Pan G, Yu J, et al. FGF2 sustains NANOG and switches the outcome of BMP4-induced human embryonic stem cell differentiation[J]. *Cell stem cell*, 2011, 8(3): 326-334.

[134] Raballo R, Rhee J, Lyn-Cook R, et al. Basic fibroblast growth factor (Fgf2) is necessary for cell proliferation and neurogenesis in the developing cerebral cortex[J]. *Journal of Neuroscience*, 2000, 20(13): 5012-5023.

[135] Sahni M, Raz R, Coffin J D, et al. STAT1 mediates the increased apoptosis and reduced chondrocyte proliferation in mice overexpressing FGF2[J]. *Development*, 2001, 128(11): 2119-2129.

[136] Nissen L J, Cao R, Hedlund E M, et al. Angiogenic factors FGF2 and PDGF-BB synergistically promote murine tumor neovascularization and metastasis[J]. *The Journal of clinical investigation*, 2007, 117(10): 2766-2777.

[137] Hafenbreidel M, Twining R C, Todd C R, et al. Blocking infralimbic basic fibroblast growth factor (bFGF or FGF2) facilitates extinction of drug seeking after cocaine self-administration[J]. *Neuropsychopharmacology*, 2015, 40(13): 2907.

[138] Xia L, Zhai M, Wang L, et al. FGF2 blocks PTSD symptoms via an astrocyte-based mechanism[J]. *Behavioural brain research*, 2013, 256: 472-480.

[139] KOBAYASHI N, MIYAJI H, SUGAYA T, et al. Bone augmentation by implantation of an FGF2-loaded collagen gel-sponge composite scaffold[J]. *Journal of Oral Tissue Engineering*, 2010, 8(2): 91-101.

[140] Akl M R, Nagpal P, Ayoub N M, et al. Molecular and clinical significance of

fibroblast growth factor 2 (FGF2/bFGF) in malignancies of solid and hematological cancers for personalized therapies[J]. *Oncotarget*, 2016, 7(28): 44735.

[141] Kastrup J. Therapeutic angiogenesis in ischemic heart disease: gene or recombinant vascular growth factor protein therapy[J]. *Current gene therapy*, 2003, 3(3): 197-206.

[142] Caldwell M A, Garcion E, He X, et al. Heparin stabilizes FGF-2 and modulates striatal precursor cell behavior in response to EGF[J]. *Experimental neurology*, 2004, 188(2): 408-420.

[143] Damon D H, Lobb R R, D'Amore P A, et al. Heparin potentiates the action of acidic fibroblast growth factor by prolonging its biological half-life[J]. *Journal of cellular physiology*, 1989, 138(2): 221-226.

[144] Volpato F Z, Almodóvar J, Erickson K, et al. Preservation of FGF-2 bioactivity using heparin-based nanoparticles, and their delivery from electrospun chitosan fibers[J]. *Acta biomaterialia*, 2012, 8(4): 1551-1559.

[145] Wu J, Ye J, Zhu J, et al. Heparin-based coacervate of FGF2 improves dermal regeneration by asserting a synergistic role with cell proliferation and endogenous facilitated VEGF for cutaneous wound healing[J]. *Biomacromolecules*, 2016, 17(6): 2168-2177.

[146] Thompson L D, Pantoliano M W, Springer B A. Energetic characterization of the basic fibroblast growth factor-heparin interaction: identification of the heparin binding domain[J]. *Biochemistry*, 1994, 33(13): 3831-3840.

[147] Guglieri S, Hricovíni M, Raman R, et al. Minimum FGF2 binding structural requirements of heparin and heparan sulfate oligosaccharides as determined by NMR spectroscopy[J]. *Biochemistry*, 2008, 47(52): 13862-13869.

[148] Goodger S J, Robinson C J, Murphy K J, et al. Evidence that heparin saccharides promote FGF2 mitogenesis through two distinct mechanisms[J].

Journal of Biological Chemistry, 2008, 283(19): 13001-13008.

[149] Garcia J, Patel N, Basehore S, et al. Fibroblast Growth Factor-2 Binding to Heparan Sulfate Proteoglycans Varies with Shear Stress in Flow-Adapted Cells[J]. *Annals of biomedical engineering*, 2019, 47(4): 1078-1093.

[150] Lühmann T, Jones G, Gutmann M, et al. Bio-orthogonal immobilization of fibroblast growth factor 2 for spatial controlled cell proliferation[J]. *ACS Biomaterials Science & Engineering*, 2015, 1(9): 740-746.

[151] Zhao H, Heusler E, Jones G, et al. Decoration of silk fibroin by click chemistry for biomedical application[J]. *Journal of structural biology*, 2014, 186(3): 420-430.

[152] Sevim S, Ozer S, Jones G, et al. Nanomechanics on FGF-2 and heparin reveal slip bond characteristics with pH dependency[J]. *ACS Biomaterials Science & Engineering*, 2017, 3(6): 1000-1007.

[153] Ibrahimi O A, Zhang F, Lang Hrstka S C, et al. Kinetic model for FGF, FGFR, and proteoglycan signal transduction complex assembly[J]. *Biochemistry*, 2004, 43(16): 4724-4730.

[154] pdb file: 1BFB. http://files.rcsb.org/pub/pdb/validation_reports/bf/1bfb/1bfb_full_validation.pdf